PHYSICAL REVIEW D **78,** 115016 (2008)

Measuring the Higgs-vector boson couplings at linear e^+e^- collider

Sukanta Dutta,[1,2,*] Kaoru Hagiwara,[2,3] and Yu Matsumoto[2,3,†]

[1]*SGTB Khalsa College, University of Delhi, Delhi-110007, India*

[2]*KEK Theory Division, 1-1 Oho Tsukuba, 305-0801, Japan*

[3]*Graduate University for Advanced Studies (Soken-dai), 1-1 Oho Tsukuba, 305-0801, Japan*

(Received 24 August 2008; published 30 December 2008)

We estimate the accuracy with which the coefficient of the *CP* even dimension-six operators involving Higgs and two vector bosons (*HVV*) can be measured at linear e^+e^- colliders. Using the optimal observables method for the kinematic distributions, our analysis is based on the five different processes. First is the *WW* fusion process in the *t*-channel ($e^+e^- \to \bar{\nu}_e \nu_e H$), where we use the rapidity y and the transverse momentum p_T of the Higgs boson as observables. Second is the *ZH* pair production process in the *s* channel, where we use the scattering angle of the *Z* and the *Z* decay angular distributions, reproducing the results of the previous studies. Third is the *t*-channel *ZZ*, fusion processes ($e^+e^- \to e^+e^-H$), where we use the energy and angular distributions of the tagged e^+ and e^-. In the fourth, we consider the rapidity distribution of the untagged e^+e^-H events, which can be approximated well as the $\gamma\gamma$ fusion of the bremsstrahlung photons from e^+ and e^- beams. As the last process, we consider the single-tagged e^+e^-H events, which probe the $\gamma e^\pm \to He^\pm$ process. All the results are presented in such a way that statistical errors of the constraints on the effective couplings and their correlations are read off when all of them are allowed to vary simultaneously, for each of the above processes, for $m_H = 120$ GeV, at $\sqrt{s} = 250$ GeV, 350 GeV, 500 GeV, and 1 TeV, with and without e^- beam polarization of 80%. We find, for instance, that the *HZZ* and *HWW* couplings can be measured with 0.6% and 0.9% accuracy, respectively, for the integrated luminosity of $L = 100$ fb^{-1} at $\sqrt{s} = 250$ GeV, 350 GeV, and $L = 500$ fb^{-1} at $\sqrt{s} = 500$ GeV, 1 TeV, for the luminosity uncertainty of 1% at each energy. We find that the luminosity uncertainty affects only one combination of the nonstandard couplings, which are proportional to the standard *HWW* and *HZZ* couplings, while it does not affect the errors of the other independent combinations of the couplings. As a consequence, we observe that a few combinations of the eight dimension-six operators can be constrained as accurately as the two operators, which have been constrained by the precision measurements of the *Z* and *W* boson properties.

DOI: 10.1103/PhysRevD.78.115016 PACS numbers: 14.80.Cp, 14.70.Fm, 14.70.Hp

I. INTRODUCTION

The standard model (SM) of the elementary particles based on the SU(3) × SU(2) × U(1) gauge symmetry has proved to be a successful theory to interpret all the precision data available to date. SM predicts a light Higgs boson whose discovery is one of the prime tasks of the upcoming future colliders.

In fact, the present electroweak precision measurements indicate the existence of a light Higgs boson [1,2]. Experiments at the CERN Large Electron Positron collider (LEP) set the lower bound on its mass of 114.1 GeV at the 95% confidence level (CL) [1]. The Fermilab Tevatron, which collides proton and antiproton at $\sqrt{s} = 2$ TeV, is currently the only collider that can produce low mass Higgs bosons. Analysis with Run IIb data samples by the CDF and D0 detectors indicates that the Tevatron experiments can observe the Higgs boson with about 10 fb^{-1} total integrated luminosity for the mass of around 120 GeV [3]. The LHC at CERN will start colliding two protons at $\sqrt{s} = 14$ TeV in the year 2008, and is geared to detect the Higgs boson in gluon-gluon and vector-boson fusion processes. It will measure ratios of various Higgs-boson couplings through variety of decay channels at accuracies of order 10 to 15% with 100 fb^{-1} luminosity [4].

Despite the success, SM presents the naturalness problem due to the quadratic sensitivity of the Higgs-boson mass to the new physics scale at high energies, which implies that there is a need of subtle fine-tuning to keep the electroweak symmetry breaking theory below the TeV scale. To put it in another way, this may suggest an existence of a new physics scale Λ not far above the TeV scale. The key to probe the new physics beyond the SM theory is to clarify the origin of the electroweak symmetry breaking, the Higgs mechanism. Therefore, it is necessary to measure the Higgs-boson properties as precisely as possible, especially the *HVV* couplings, because they are expected to be sensitive to the symmetry breaking physics that gives rise to the weak-boson masses.

With this motivation, we re-examine the potential of the future e^+e^- linear collider, the International Linear Collider (ILC) in the precise measurement of the *HVV* couplings. Clean experimental environment, well-defined

*Sukanta.Dutta@kek.jp
†ymatsu@post.kek.jp

initial state, tunable energy, and beam polarization render ILC to be the best machine to study the Higgs-boson properties with high precision. In this paper, we study the sensitivity of the ILC measurements on all the HVV (HWW, HZZ, $HZ\gamma$, and $H\gamma\gamma$) couplings comprehensively and semiquantitatively by using all the available processes with a light Higgs-boson ($m_H \lesssim 120$ GeV); $e^+e^- \to \nu_e\bar{\nu}_e H$ with t-channel W exchange, $e^+e^- \to ZH$ with s-channel Z exchange, $e^+e^- \to e^+e^- H$ with t-channel Z exchange, no-tag $e^+e^- \to (e^+e^-)H$ process from $\gamma\gamma$ fusion, and single-tagged $e^+e^- \to (e^\pm)e^\mp H$ process that probes $\gamma e^\mp \to He^\mp$ via t-channel γ and Z exchange.

In order to quantify the ILC sensitivity to measure various HVV couplings simultaneously, we adopt the powerful technique of the optimal observables method [5–8]. It allows us to measure several couplings simultaneously as long as the nonstandard couplings give rise to different observable kinematic distributions. The results can be summarized in terms of the covariance matrix of the measurement errors, from each process at each energy, that scales inversely as the integrated luminosity.

In order to combine results from different processes and at different energies, we adopt the effective Lagrangian of the SM particles with operators of mass dimension six to parametrize all the HVV couplings [9–11]. This allows us not only to compare the significance of the measurements of various HVV couplings at different energies and at different colliders, but also to study what ILC can add to the precision measurements of the Z and W boson properties in the search for new physics via quantum effects. We therefore parametrize the HVV couplings as linear combination of all the dimension-six operators that are allowed by the electroweak gauge symmetry and CP invariance.

Some of the previous studies based on the optimal observables method are found for CP-violating effects in $e^+e^- \to ZH$ via HZZ and $HZ\gamma$ couplings [8,12], and also in $e^+e^- \to t\bar{t}H$ [8]. CP conserving and CP violating effects in the $e^+e^- \to ZH$ process have been studied in Refs. [13,14]. In Refs. [8,13,14] all the relevant couplings are varied simultaneously, and their correlations are studied. More recently, the ILC sensitivity to the HZZ and HWW couplings has been studied in Refs. [15–17]. Bounds on the coefficients of the Higgs-vector-boson dimension-six operators have been found in Refs. [18,19] based on nonobservation of the Higgs-boson signal at the Tevatron. Whenever relevant, we compare our results with the previous observations.

This paper is organized as follows: In Sec. II, we describe the low-energy effective interactions among the Higgs boson and the electroweak gauge bosons arising from new physics that is parametrized in terms of the effective Lagrangian of the SM particles with operators up to mass dimension six. In Sec. III, we introduce the optimal observables method and explain how we perform the phase-space integration when some of the kinematic distributions are unobservable, such as neutrino momenta and a distinction between quark and antiquark jets. Although we present numerical results for unpolarized beams and for 80% polarized e^- beam only, all the formulas are presented for an arbitrary polarization of e^- and e^+ beams. After introducing final state cuts, such as those for the $e^\pm$ tagging and those for selecting or excluding $Z \to f\bar{f}$ events, we present the total cross sections for all the five processes at $\sqrt{s} = 200$ GeV–1 TeV for $m_H = 120$ GeV, and at $\sqrt{s} = 250$ GeV, 500 GeV, 1 TeV for $m_H =$ 100–200 GeV. Then in Sec. IV we compute the statistical errors of the nonstandard HWW couplings extracted from measurements of the WW-fusion process, $e^+e^- \to \nu_e\bar{\nu}_e H$. In Sec. V, we study the constraints on the HZZ and $HZ\gamma$ couplings extracted from ZH production. In Sec. VI, not only the HZZ and $HZ\gamma$ couplings but also the $H\gamma\gamma$ coupling are studied in the double-tag $e^+e^- \to e^+e^- H$ process via t-channel Z and γ exchange. In Sec. VII, we obtain the constraints on the $H\gamma\gamma$ coupling from the $\gamma\gamma$ fusion, in no-tag $e^+e^- \to (e^+e^-)H$ events, using the equivalent real photon approximation. In Sec. VIII, we consider the single-tag $e^+e^- \to (e^\pm)e^\mp H$ process to constrain the $H\gamma\gamma$ and $H\gamma Z$ couplings. In Sec. IX, we address the implication of luminosity uncertainty on the measurement of these couplings. In Sec. X, we summarize all our results, compare them with previous studies, and present our estimates for the ILC constraints on the dimension-six operators, which are then compared with the constraints from the precision electroweak measurements of the W and Z boson properties. In the appendices, we present our parameterizations of the 3-body phase space (Appendix A), and the explicit forms the t-channel and s-channel currents and their contractions that appear in the helicity amplitudes (Appendix B).

II. GENERALIZED HVV VERTEX WITH DIMENSION-SIX OPERATORS

In our study, we adopt the effective Lagrangian of the Higgs and the gauge bosons with operators up to mass dimension six

$$L_{\rm eff} = L_{\rm SM} + \sum_i \frac{f_i^{(6)}}{\Lambda^2}\mathcal{O}_i^{(6)}, \tag{1}$$

where $L_{\rm SM}$ denotes the renormalizable SM Lagrangian and $\mathcal{O}_i^{(6)}$'s are the gauge-invariant operators of mass dimension six. The index i runs over all operators of the given mass dimension. The mass scale is set by Λ, and the coefficients $f_i^{(6)}$ are dimensionless parameters, which are determined once the full theory is known. Excluding the dimension-five operators for the neutrino Majorana masses, and the dimension-six operators with quark and lepton fields, we are left with the following eight CP-even operators that affect the HVV couplings. Notation of the operators are

taken from the Ref. [20].

$$\mathcal{O}_{WW} = \Phi^\dagger \bar{W}^{\mu\nu}\bar{W}_{\mu\nu}\Phi, \tag{2a}$$
$$\mathcal{O}_{BB} = \Phi^\dagger \bar{B}^{\mu\nu}\bar{B}_{\mu\nu}\Phi, \tag{2b}$$
$$\mathcal{O}_{BW} = \Phi^\dagger \bar{B}^{\mu\nu}\bar{W}_{\mu\nu}\Phi, \tag{2c}$$
$$\mathcal{O}_{W} = (D^\mu\Phi)^\dagger \bar{W}_{\mu\nu}(D^\nu\Phi), \tag{2d}$$
$$\mathcal{O}_{B} = (D^\mu\Phi)^\dagger \bar{B}_{\mu\nu}(D^\nu\Phi), \tag{2e}$$
$$\mathcal{O}_{\phi 1} = [(D_\mu\Phi)^\dagger\Phi][\Phi^\dagger(D^\mu\Phi)], \tag{2f}$$
$$\mathcal{O}_{\phi 4} = (\Phi^\dagger\Phi)(D_\mu\Phi)^\dagger(D^\mu\Phi), \tag{2g}$$
$$\mathcal{O}_{\phi 2} = \frac{1}{2}\partial_\mu(\Phi^\dagger\Phi)\partial^\mu(\Phi^\dagger\Phi). \tag{2h}$$

Here, Φ denotes the Higgs doublet field with the hypercharge $Y = 1/2$, and the covariant derivative is $D_\mu = \partial_\mu + i\hat{g}_W T^a \hat{W}^a_\mu + i\hat{g}_Y Y \hat{B}_\mu$, where the gauge couplings and the gauge fields with a caret represent those of the SM, in the absence of higher-dimensional operators. The gauge-covariant and invariant tensors $\bar{W}_{\mu\nu}$ and $\bar{B}_{\mu\nu}$, respectively, are $\bar{W}_{\mu\nu} = i\hat{g}_W T^a \hat{W}^a_{\mu\nu}$, and $\bar{B}_{\mu\nu} = \frac{i}{2}\hat{g}_Y \hat{B}_{\mu\nu}$. The coefficients of the operators (2a)–(2h), which are denoted as $f_i^{(6)}/\Lambda^2$ in the effective Lagrangian of Eq. (1), should give us information about physics beyond the SM. So far, the precision measurements of the weak-boson properties [2] constrained the operators $\mathcal{O}_{BW}$ and $\mathcal{O}_{\phi 1}$, which have been useful in testing some models of the electroweak symmetry breakdown [10,21]. In this report, we explore the accuracy with which the ILC experiments can measure the coefficients of all these eight operators when a light Higgs boson exists.

When the Higgs field acquires the vacuum expectation value $\langle\Phi\rangle = \frac{1}{\sqrt{2}}(0, v)^T$, the bilinear part of the effective Lagrangian of Eq. (1) is expressed as

$$\begin{aligned} L_{\text{eff}} = & -\frac{1}{4}\left(1 + \frac{\hat{g}_W^2 v^2}{2\Lambda^2} f_{WW}\right)\hat{W}^a_{\mu\nu}\hat{W}^{a\mu\nu} - \frac{1}{4}\left(1 + \frac{\hat{g}_Y^2 v^2}{2\Lambda^2} f_{BB}\right)\hat{B}_{\mu\nu}\hat{B}^{\mu\nu} + \frac{\hat{g}_W\hat{g}_Y v^2}{8\Lambda^2} f_{BW}\hat{B}_{\mu\nu}\hat{W}^{3\mu\nu} \\ & + \frac{\hat{g}_W^2 v^2}{8}\left(1 + \frac{v^2}{2\Lambda^2} f_{\phi 4}\right)(\hat{W}^1_\mu\hat{W}^{1\mu} + \hat{W}^2_\mu\hat{W}^{2\mu}) + \frac{v^2}{8}\left(1 + \frac{v^2}{2\Lambda^2}(f_{\phi 1} + f_{\phi 4})\right)(\hat{g}_W\hat{W}^3{}_\mu - \hat{g}_Y\hat{B}_\mu)(\hat{g}_W\hat{W}^{3\mu} - \hat{g}_Y\hat{B}^\mu) \\ & + \frac{1}{2}\left(1 + \frac{v^2}{2\Lambda^2}(f_{\phi 1} + f_{\phi 4} + 2f_{\phi 2})\right)(\partial_\mu\hat{H}_0)(\partial^\mu\hat{H}_0) - \frac{1}{2}\hat{m}_H^2\hat{H}_0^2 + \cdots. \end{aligned} \tag{3}$$

After renormalization of gauge fields and their couplings,

$$W^a_\mu = \left(1 + \frac{\hat{g}_W^2 v^2}{4\Lambda^2} f_{WW}\right)\hat{W}^a_\mu; \qquad g_W W^a_\mu = \hat{g}_W \hat{W}^a_\mu; \tag{4a}$$
$$B_\mu = \left(1 + \frac{\hat{g}_Y^2 v^2}{4\Lambda^2} f_{BB}\right)\hat{B}_\mu; \qquad g_Y B_\mu = \hat{g}_Y \hat{B}_\mu; \tag{4b}$$

and after diagonalization of the mass squared matrices, the effective Lagrangian reads

$$\begin{aligned} L_{\text{eff}} = & -\frac{1}{2}W^+_{\mu\nu}W^{-\mu\nu} - \frac{1}{4}Z_{\mu\nu}Z^{\mu\nu} - \frac{1}{4}A_{\mu\nu}A^{\mu\nu} \\ & + \frac{g_W g_Y v^2}{8\Lambda^2} f_{BW} B_{\mu\nu}W^{3\mu\nu} + m_W^2 W^+_\mu W^{-\mu} \\ & + \frac{m_Z^2}{2}Z_\mu Z^\mu - \frac{1}{2}(\partial_\mu H)(\partial^\mu H) - \frac{1}{2}m_H^2 H^2 + \cdots, \end{aligned} \tag{5}$$

where

$$m_W^2 = \frac{g_W^2 v^2}{4}\left[1 + \frac{v^2}{2\Lambda^2} f_{\phi 4}\right], \tag{6a}$$
$$m_Z^2 = \frac{g_Z^2 v^2}{4}\left[1 + \frac{v^2}{2\Lambda^2}(f_{\phi 1} + f_{\phi 2})\right], \tag{6b}$$
$$m_H^2 = \hat{m}_H^2\left[1 - \frac{v^2}{2\Lambda^2}(f_{\phi 1} + f_{\phi 4} + 2f_{\phi 2})\right], \tag{6c}$$
$$H = \left[1 + \frac{v^2}{4\Lambda^2}(f_{\phi 1} + f_{\phi 4} + 2f_{\phi 2})\right]^{1/2}\hat{H}_0. \tag{6d}$$

All the remaining terms in the effective Lagrangian, denoted by dots in Eq. (5), are expressed in terms of the renormalized fields, couplings and masses, as defined in Eqs. (4) and (6). The standard gauge interactions are dictated by the covariant derivative

$$\begin{aligned} D_\mu = & \partial_\mu + i\frac{g_W}{\sqrt{2}}(T^+W^+_\mu + T^-W^-_\mu) + ig_Z(T^3 - s_W^2 Q)Z_\mu \\ & + ieQA_\mu, \end{aligned} \tag{7}$$

where $T^\pm = (T^1 \pm iT^2)/2$, $Q = T^3 + Y$, and $e = g_W s_W = g_Y c_W = g_Z c_W s_W$.

Before expressing the HVV interactions of L_{eff}, let us briefly review the observable consequence of new physics in the gauge boson two point functions in Eq. (5). First, the ratio of the neutral current and the charged current interactions at low energies deviate [21,22] from unity,

$$\rho\left(= \frac{1}{1 - \alpha T}\right) = \frac{G_{\text{N.C.}}}{G_{\text{C.C.}}} = \frac{g_Z^2/m_Z^2}{g_W^2/m_W^2} = 1 - \frac{f_{\phi 1}}{2\Lambda^2}. \tag{8}$$

Second, the extra kinetic mixing between $B_{\mu\nu}$ and $W^3_{\mu\nu}$ modifies the γ and Z boson propagators

$$\Delta\Pi_T^{QQ}(q^2) = 2\Delta\Pi_T^{3Q}(q^2) = \left(-\frac{v^2}{2\Lambda^2} f_{BW}\right)q^2 \tag{9}$$

in the notation of Ref. [23], which contributes to the S parameter [21]

$$S = 16\pi\left[\frac{\bar{s}^2(m_Z^2)\bar{c}^2(m_Z^2)}{\bar{e}^2(m_Z^2)} - \frac{1}{\bar{g}_Z^2(0)}\right] = -\frac{4\pi v^2}{\Lambda^2} f_{BW}. \quad (10)$$

Here, the over-lined couplings $\bar{e}^2(q^2)$, $\bar{s}^2(q^2) = 1 - \bar{c}^2(q^2)$, and $\bar{g}_Z^2(q^2)$ are the effective couplings that contain the gauge-boson propagator corrections at the momentum transfer q^2 [23]. We will examine the constraints on $f_{\phi 1}$ and f_{BW} from the precision measurements of the weak-boson properties in the last section of this report.

The terms describing the HVV couplings in the effective Lagrangian are now expressed as

$$\begin{aligned} L_{\rm eff}^{HVV} &= (1 + c_{1WW}) g m_W H W_\mu^+ W^{-\mu} + (1 + c_{1ZZ}) \frac{g_Z m_Z}{2} H Z_\mu Z^\mu \\ &+ \frac{g_Z}{m_Z}\left[c_{2WW} H W^+_{\mu\nu} W^{-\mu\nu} + \frac{c_{3WW}}{2}\{((\partial_\mu H) W_\nu^- - (\partial_\nu H) W_\mu^-) W^{+\mu\nu} + \text{H.c.}\}\right] \\ &+ \frac{g_Z}{m_Z}\left[\frac{c_{2ZZ}}{2} H Z_{\mu\nu} Z^{\mu\nu} + \frac{c_{3ZZ}}{2}((\partial_\mu H) Z_\nu - (\partial_\nu H) Z_\mu) Z^{\mu\nu}\right] + \frac{g_Z}{m_Z}\left[\frac{c_{2\gamma\gamma}}{2} H A_{\mu\nu} A^{\mu\nu}\right] \\ &+ \frac{g_Z}{m_Z}\left[c_{2Z\gamma} H Z_{\mu\nu} A^{\mu\nu} + c_{3Z\gamma}((\partial_\mu H) Z_\nu - (\partial_\nu H) Z_\mu) A^{\mu\nu}\right] \ldots, \end{aligned} \quad (11)$$

where the 9 dimensionless couplings, c_i, parametrize all the nonstandard HVV interactions:

$$c_{1ZZ} = \frac{v^2}{4\Lambda^2}(3 f_{\phi 1} + 3 f_{\phi 4} - 2 f_{\phi 2}), \quad (12a)$$

$$c_{1WW} = \frac{v^2}{4\Lambda^2}(-f_{\phi 1} + 3 f_{\phi 4} - 2 f_{\phi 2}), \quad (12b)$$

$$c_{2ZZ} = \frac{m_Z^2}{\Lambda^2}(-s_W^4 f_{BB} - s_W^2 c_W^2 f_{BW} - c_W^4 f_{WW}), \quad (12c)$$

$$c_{2Z\gamma} = \frac{m_Z^2}{\Lambda^2}\left(s_W^2 f_{BB} + \frac{1}{2}(c_W^2 - s_W^2) f_{BW} - c_W^2 f_{WW}\right) s_W c_W, \quad (12d)$$

$$c_{2\gamma\gamma} = \frac{m_Z^2}{\Lambda^2}(-f_{BB} + f_{BW} - f_{WW}) c_W^2 s_W^2, \quad (12e)$$

$$c_{2WW} = \frac{m_Z^2 c_W^2}{\Lambda^2}(-f_{WW}), \quad (12f)$$

$$c_{3ZZ} = \frac{m_Z^2}{2\Lambda^2}(-s_W^2 f_B - c_W^2 f_W), \quad (12g)$$

$$c_{3Z\gamma} = \frac{m_Z^2}{4\Lambda^2}(f_B - f_W) s_W c_W, \quad (12h)$$

$$c_{3WW} = \frac{m_Z^2 c_W^2}{2\Lambda^2}(-f_W). \quad (12i)$$

From the effective Lagrangian of Eq. (11), we obtain the Feynman rule for $V_1^\mu(p_1) - V_2^\nu(p_2) - H(p_H)$ vertex as

$$\Gamma_{\mu\nu}^{HV_1V_2}(p_H, p_1, p_2) = g_Z m_Z\left[h_1^{V_1V_2} g_{\mu\nu} + \frac{h_2^{V_1V_2}}{m_Z^2} p_{2\mu} p_{1\nu}\right], \quad (13)$$

where all three momenta are incoming, $p_1 + p_2 + p_H = 0$, as shown in Fig. 1. V_1 and V_2 can be $(V_1V_2) = (ZZ)$, $(Z\gamma)$, (γZ), $(\gamma\gamma)$, (W^+W^-), or (W^-W^+). The coefficients $h_i^{V_1V_2}(p_1, p_2)$ are

$$h_1^{ZZ}(p_1, p_2) = 1 + c_{1ZZ} + \frac{p_1^2 + p_2^2 - m_H^2}{m_Z^2} c_{2ZZ} + \frac{m_H^2}{m_Z^2} c_{3ZZ}, \quad (14a)$$

$$h_2^{ZZ}(p_1, p_2) = 2(c_{2ZZ} - c_{3ZZ}), \quad (14b)$$

for the HZZ couplings,

$$h_1^{\gamma\gamma}(p_1, p_2) = \frac{p_1^2 + p_2^2 - m_H^2}{m_Z^2} c_{2\gamma\gamma}, \quad (15a)$$

$$h_2^{\gamma\gamma}(p_1, p_2) = 2 c_{2\gamma\gamma}, \quad (15b)$$

for the $H\gamma\gamma$ couplings,

$$h_1^{Z\gamma}(p_1, p_2) = \frac{p_1^2 + p_2^2 - m_H^2}{m_Z^2} c_{2Z\gamma} - \frac{p_1^2 - p_2^2 - m_H^2}{m_Z^2} c_{3Z\gamma}, \quad (16a)$$

$$h_1^{\gamma Z}(p_1, p_2) = \frac{p_1^2 + p_2^2 - m_H^2}{m_Z^2} c_{2Z\gamma} - \frac{-p_1^2 + p_2^2 - m_H^2}{m_Z^2} c_{3Z\gamma}, \quad (16b)$$

$$h_2^{Z\gamma}(p_1, p_2) = h_2^{\gamma Z}(p_1, p_2) = 2(c_{2Z\gamma} - c_{3Z\gamma}), \quad (16c)$$

for the $HZ\gamma$ couplings. It is to be noted that the $HZ\gamma$ coupling $c_{3Z\gamma}$ has the Feynman rule, which is not symmetric under an interchange of p_1 and p_2. For the HWW

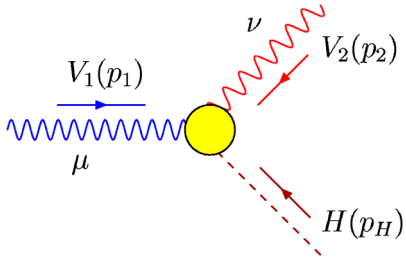

FIG. 1 (color online). The HVV Vertex.

couplings,

$$h_i^{W^+W^-}(p_1,p_2) = h_i^{W^-W^+}(p_1,p_2) = h_i^{WW}(p_1,p_2) \quad (i=1,2), \tag{17a}$$

$$h_1^{WW}(p_1,p_2) = (1+c_{1WW})\cos^2\theta_W + \frac{p_1^2+p_2^2-m_H^2}{m_Z^2}c_{2WW} + \frac{m_H^2}{m_Z^2}c_{3WW}, \tag{17b}$$

$$h_2^{WW}(p_1,p_2) = 2(c_{2WW}-c_{3WW}). \tag{17c}$$

Although we do not consider off-shell Higgs-boson contributions in this report, m_H^2 should be replaced by $(p_1+p_2)^2$ in the above Feynman rules when the Higgs boson is off shell.

III. OPTIMAL OBSERVABLES AND PHASE SPACE

A. Optimal observables method

The optimal observables method [8] makes use of all the kinematic distributions that are observable in experiments. We therefore summarize our phase-space parameterizations for all the Higgs-boson production processes in e^+e^- collisions considered in this study, which can be generically written as

$$e^-\left(k_1,\frac{\sigma_1}{2}\right)+e^+\left(k_2,\frac{\sigma_2}{2}\right)\to f\left(p_1,\frac{\lambda_1}{2}\right)+\bar{f}\left(p_2,\frac{\lambda_2}{2}\right)+H(p_H). \tag{18}$$

Here, k_i and $\sigma_i/2$ are the $e^\pm$ four momenta and helicities, respectively, and p_i^μ and $\lambda_i/2$ are the four momenta and helicities, respectively, of the produced fermion ($i=1$) and antifermion ($i=2$). For $f\neq e$, ν_e, the processes (18) occur only through the ZH production diagram as shown in Fig. 2(a), whereas for $f=e$ or ν_e, both the diagrams Figs. 2(a) and 2(b) contribute. The effective HVV vertex is depicted by the solid circle in the Feynman diagrams. The ZH production process (a) is sensitive to the HZZ and $HZ\gamma$ couplings, while the vector-boson fusion processes (b) are sensitive to the HWW coupling for $f=\nu_e$, and the HZZ, $HZ\gamma$, $H\gamma\gamma$ couplings for $f=e$.

The matrix elements for the processes Eq. (18) can in general be expressed as

$$M_{\sigma_1\sigma_2}^{\lambda_1\lambda_2} = (M_{\rm SM})_{\sigma_1\sigma_2}^{\lambda_1\lambda_2} + \sum_{i=1}^{n} c_i (M_i)_{\sigma_1\sigma_2}^{\lambda_1\lambda_2}, \tag{19}$$

where $(M_{\rm SM})_{\sigma_1\sigma_2}^{\lambda_1\lambda_2}$ denotes the SM helicity amplitude, and c_i denotes the nonstandard couplings of Eq. (12) that contribute to the process. The matrix elements $(M_i)_{\sigma_1\sigma_2}^{\lambda_1\lambda_2}$ give the helicity amplitudes, which are proportional to the coupling c_i. If the e^- and e^+ beam polarizations are P and $\bar{P}$ ($|P|, |\bar{P}| \le 1$), respectively, the differential cross section can be expressed as

$$d\sigma(P,\bar{P}) = \left[\Sigma_{\rm SM}(P,\bar{P};\Phi_3) + \sum_{i=1}^{n} c_i \Sigma_i(P,\bar{P};\Phi_3)\right] d\Phi_3, \tag{20}$$

where the nonstandard couplings c_i are assumed to be real and small, and hence the terms quadratic in couplings are dropped. Here, $d\Phi_3$ is the 3-body phase-space volume of the $f\bar{f}H$ system, and

$$\Sigma_{\rm SM}(P,\bar{P};\Phi_3) = \frac{1}{2s}\sum_{\sigma_1,\sigma_2,\lambda_1,\lambda_2}\left(\frac{1+\sigma_1 P}{2}\right)\times\left(\frac{1+\sigma_2\bar{P}}{2}\right)|(M_{\rm SM})_{\sigma_1\sigma_2}^{\lambda_1\lambda_2}|^2 \tag{21}$$

gives the differential cross section of the SM. The term proportional to c_i,

$$\Sigma_i(P,\bar{P};\Phi_3) = \frac{1}{2s}\sum_{\sigma_1,\sigma_2,\lambda_1,\lambda_2}\left(\frac{1+\sigma_1 P}{2}\right)\times\left(\frac{1+\sigma_2\bar{P}}{2}\right)2\,{\rm Re}[(M_i)_{\sigma_1\sigma_2}^{\lambda_1\lambda_2}(M_{\rm SM}^*)_{\sigma_1\sigma_2}^{\lambda_1\lambda_2}] \tag{22}$$

gives the differential distribution, which is proportional to c_i.

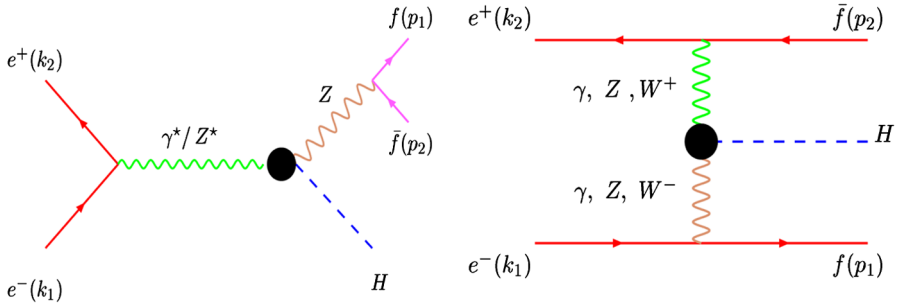

(a) ZH production (b) vector-boson fusion

FIG. 2 (color online). Feynman diagrams for $e^-e^+\to f\bar{f}H$.

In the optimal observables method, we make full use of the distribution $\Sigma_i(P,\bar{P};\Phi_3)$ in order to constrain c_i. For instance, if all $\Sigma_i(P,\bar{P};\Phi_3)$ have different shapes from each other, then in principle, we can constrain all the coefficients c_i simultaneously. For a given integrated luminosity L, the statistical errors of the c_i measurement can be obtained from a χ^2 function

$$\chi^2(c_i) = \sum_{k=1}^{N}\left(\frac{N^k_{\rm exp}(P,\bar{P}) - N^k_{\rm th}(P,\bar{P};c_i)}{\sqrt{N^k_{\rm exp}(P,\bar{P})}}\right)^2, \tag{23a}$$

$$= \sum_{k=1}^{N}\left(\frac{L\Sigma_{\rm exp}(P,\bar{P};\Phi_3^k)\Delta - L[\Sigma_{\rm SM}(P,\bar{P};\Phi_3^k) + \sum_{i=1}^{n} c_i\Sigma_i(P,\bar{P};\Phi_3^k)]\Delta}{\sqrt{L\Sigma_{\rm exp}(P,\bar{P};\Phi_3^k)\Delta}}\right)^2, \tag{23b}$$

where $N^k_{\rm exp}(P,\bar{P})$ is the number of events in the k'th bin, and $N^k_{\rm th}(P,\bar{P};c_i)$ is the corresponding prediction of the theory, which depends on the parameters of the SM and c_i. In the second line (23b), Φ_3^k for $k=1$ to N gives the representative phase-space point of a bin number k with the bin size Δ. Now, if all the coefficients c_i are tiny, the experimental result in the k'th bin should be approximated by the SM prediction as

$$\Sigma_{\rm exp}(P,\bar{P};\Phi_3^k) \approx \Sigma_{\rm SM}(P,\bar{P};\Phi_3^k). \tag{24}$$

The χ^2 function can then be expressed as

$$\chi^2(c_i) = \chi^2_{\rm min} + \sum_{i,j}(c_i - \bar{c}_i)[V^{-1}_{(P,\bar{P})}]_{ij}(c_j - \bar{c}_j), \tag{25}$$

where

$$[V^{-1}_{(P,\bar{P})}]_{ij} = L_0\sum_{k=1}^{N}\frac{\Sigma_i(P,\bar{P};\Phi_3^k)\Sigma_j(P,\bar{P};\Phi_3^k)}{\Sigma_{\rm SM}(P,\bar{P};\Phi_3^k)}\Delta, \tag{26a}$$

$$\overset{N\to\infty}{\to} L_0\int\frac{\Sigma_i(P,\bar{P};\Phi_3)\Sigma_j(P,\bar{P};\Phi_3)}{\Sigma_{\rm SM}(P,\bar{P};\Phi_3)}d\Phi_3, \tag{26b}$$

where we take $L_0 = 100\ {\rm fb}^{-1}$ as a nominal integrated luminosity throughout this report. If the total number of events is sufficiently large, the integral representation in Eq. (26b) gives a good approximation for the V^{-1} matrix. The value of $\chi^2_{\rm min}$ and the mean value $\bar{c}_i$ depend on the actual experimental results, or the small deviation from the equality in Eq. (24). If the SM prediction gives a reasonably good description of the data in most of the phase-space region, then the statistical errors of c_i and their correlations are determined solely in terms of the covariance matrices V, which is the inverse of the matrix given in Eq. (26);

$$c_i - \bar{c}_i = \pm\Delta c_i = \pm\sqrt{V_{ii}}, \qquad \rho_{ij} = V_{ij}/\sqrt{V_{ii}V_{jj}}. \tag{27}$$

In practice, however, we should address the following subtleties:

(i) If the statistical error becomes small, systematic errors need to be considered.

(ii) The results depend on how we split the total luminosity to different beam polarizations.

(iii) Not all the 3-body phase-space points are observable in experiments.

As for the first issue, we assume that the energy and angular resolutions of ILC detectors are good enough to justify our integral approximation of Eq. (26), and consider only the impacts of the luminosity uncertainty as a source of the systematic error, which is discussed in Sec. IX. We leave the difficult problem of background contaminations and the spectrum distribution due to bremsstrahlung and beamstrahlung photon emissions to future studies. In short, our results should be regarded as an ultimate accuracy of the HVV couplings measurement for a perfect detector in a background-free environment, when the SM predictions are accurately known.

On the second point, we provide numerical results for the two very simple cases only:

(1) Unpolarized $e^\pm$ beam: The total integrated luminosity L is given for collisions with $(P,\bar{P}) = (0,0)$ at each collider energy $\sqrt{s}$. However, in order to save the length of this article, we provide the unpolarized results specifically only for s-channel ZH production at $\sqrt{s} = 250$ GeV. They are calculated for all the processes at all energy choices and are used to evaluate the significance of the beam polarization after all the channels and energies are combined in Sec. X.

(2) 80% polarized e^- beam: Exactly half of the total luminosity L is given for collisions with $(P,\bar{P}) = (0.8,0)$, and the remaining half with $(P,\bar{P}) = (-0.8,0)$.

In general, the covariance matrix depends on the partition of the total luminosity into experiments with different sets of e^- and e^+ beam polarizations. If the e^- and e^+ beams with polarizations $P = \pm|P|$ and $\bar{P} = \pm|\bar{P}|$, respectively, are available and if the integrated luminosity of $L_{(P,\bar{P})}$ is distributed for each case, then by using the definition of the inverse of the covariance matrix for the beam polarization $(P,\bar{P})$ in Eq. (26), the inverse of the total covariance matrix

is obtained as

$$V^{-1} = \frac{L_{(|P|,|\bar{P}|)}}{L_0} V^{-1}_{(|P|,|\bar{P}|)} + \frac{L_{(-|P|,|\bar{P}|)}}{L_0} V^{-1}_{(-|P|,|\bar{P}|)} + \frac{L_{(|P|,-|\bar{P}|)}}{L_0} V^{-1}_{(|P|,-|\bar{P}|)} + \frac{L_{(-|P|,-|\bar{P}|)}}{L_0} V^{-1}_{(-|P|,-|\bar{P}|)}. \tag{28}$$

Our first case is simply $L(0, 0) = L_{\text{total}}$ and the second case stands for

$$L_{(P=0.8,\bar{P}=0)} = L_{(P=-0.8,\bar{P}=0)} = \frac{L_{\text{total}}}{2}. \tag{29}$$

It should be noted that an equal partition of the total luminosity as above is advantageous for the asymmetry measurements, and hence for discriminating among different couplings, while $L_{(P=-|P|,\bar{P}=|\bar{P}|)} = L_{\text{total}}$ maximizes the WW-fusion cross section.

We address the third point of limited observable kinematic distributions in the following subsection.

B. Observable phase space for each process

The observability of the three-body phase-space point depends on species of $f\bar{f}$ pair, and also on their energy and the scattering angle in the laboratory frame. Let us discuss the following 4 cases one by one:

(1) $f = \mu, \tau$
(2) $f = e$
(3) $f = \nu_e, \nu_\mu, \nu_\tau$
(4) $f = u, d, s, c, b$

First, for $f = \mu$ and τ, all the four momenta p_1, p_2, p_H are measured and used in evaluating V^{-1} to estimate the experimental sensitivity. Since only one diagram Fig. 2(a) contributes to the cross section, a very tiny fraction of $\mu^\pm$ and $\tau^\pm$ escape detection along the beam pipe. We therefore use the whole phase-space region to evaluate the inverse of the covariance matrix Eq. (26). We also assume that the majority of $\tau^+\tau^- H$ events can be made background free by selecting the events, in which the $\tau^+\tau^-$ invariant mass is reconstructed and required to match the Z-boson mass. Although this reconstruction is not possible when the Higgs-boson decay has significant missing momentum, such as $H \to \tau^+\tau^-$ and $H \to W^+W^-$, we do not take account of resulting reduction of the number of events, since it can be considered as part of detection efficiency.

We do not consider the τ polarization in our analysis, because it was found in Ref. [13] that its impact is not significant once the e^- beam polarization is available.

Second, for $f = e$, we can also measure both p_1 and p_2 uniquely. For this process both the diagrams Figs. 2(a) and 2(b) contribute to the cross section because of the possible escape of e^+ or e^- (or both) along the beam pipe, the events can be divided into the following four classes:

(1) ZH events are selected by requiring

$$|\cos\theta_{e^\pm}| < 0.995, \qquad |m_{e^+e^-} - m_Z| < 5\Gamma_Z. \tag{30}$$

(2) Both outgoing $e^\pm$ are detected (double-tag events) when

$$p_T(e^\pm) > 1 \text{ GeV}, \qquad |\cos\theta_{e^\pm}| < 0.995, \qquad |m_{e^+e^-} - m_Z| > 5\Gamma_Z. \tag{31}$$

(3) When a photon is exchanged either from electron or positron in the t channel, the corresponding outgoing $e^\pm$ tends to escape detection (single-tag events). Those events are selected by requiring

$$p_T(e^-) > 1 \text{ GeV}, \quad |\cos\theta_{e^-}| < 0.995 < |\cos\theta_{e^+}|, \tag{32a}$$

or

$$p_T(e^+) > 1 \text{ GeV}, \quad |\cos\theta_{e^+}| < 0.995 < |\cos\theta_{e^-}|. \tag{32b}$$

(4) When a photon is exchanged from both the $e^\pm$ legs in the t channel, both of the outgoing $e^\pm$ tend to escape detection (no-tag event). The selection conditions are

$$|\cos\theta_{e^\pm}| > 0.995. \tag{33}$$

Although the above classification misses a part of the phase space where $|\cos\theta_{e^\pm}| < 0.995$ and $p_T(e^\pm) < 1$ GeV, we find that less than 0.001% (0.02%) of the total e^+e^-H events escape from this region of phase space at $\sqrt{s} =$ 500 GeV(250 GeV).

For the ZH production case (30) and for the double-tagged eeH events (31), we assume that the whole 3-body phase space is observable, and the inverse of the covariance matrix V^{-1} is calculated by integrating over the phase space with the selection cuts. In the case of no-tagged events (33), most of the events are due to $\gamma\gamma$ fusion, and it is sensitive to the $H\gamma\gamma$ coupling. We estimate the cross section by using the equivalent real photon approximation in Sec. VII. Since typical transverse momentum of the Higgs boson is smaller than the experimental resolution, the only observable kinematic variable is the Higgs-boson rapidity

$$y_H = \frac{1}{2} \ln \frac{E_H + p_{HZ}}{E_H - p_{HZ}}, \tag{34}$$

where p_{HZ} is the momentum component along the e^- beam direction. The cross section for the no-tag $(ee)H$ events can then be expressed as

$$\frac{d\sigma}{dy_H} = \Sigma_{\rm SM}(y_H) + \sum_i c_i \Sigma_i(y_H) \tag{35}$$

and accordingly, the inverse covariance matrix elements are calculated in terms of $\Sigma_{\rm SM}(y_H)$ and $\Sigma_i(y_H)$. In our study, we find in Sec. VII that $\Sigma_i(y_H) = \text{constant} \times \Sigma_{\rm SM}(y_H)$, and hence only the total production cross section constrains the $H\gamma\gamma$ coupling.

The single-tag $(e)eH$ events, where either e^- or e^+ escapes detection, are sensitive to both $H\gamma\gamma$ and $HZ\gamma$ couplings. We can again use the equivalent real photon approximation for the emission from untagged $e^\pm$, and the differential cross section is expressed as

$$d\sigma = d\hat{\sigma}(\hat{s} = sz) D_{\gamma/e}(z) dz, \tag{36}$$

where $D_{\gamma/e}(z)$ is the number density of an equivalent real photon of momentum fraction z, and the subprocess cross section for $\gamma e \to He$ can be expressed as

$$\frac{d\hat{\sigma}}{d\cos\hat{\theta}} = \hat{\Sigma}_{\rm SM}(\cos\hat{\theta}) + \sum_i c_i \hat{\Sigma}_i(\cos\hat{\theta}), \tag{37}$$

where $\hat{\theta}$ is the scattering angle in the observed eH rest frame. By inserting Eq. (37) into Eq. (36), we find

$$d\sigma = \left[D_{\gamma/e}(z) \hat{\Sigma}_{\rm SM}(\cos\hat{\theta}) + \sum_i c_i D_{\gamma/e}(z) \hat{\Sigma}_i(\cos\hat{\theta}) \right] dz\, d\cos\hat{\theta}, \tag{38a}$$

$$\equiv \left[\Sigma_{\rm SM}(z, \cos\hat{\theta}) + \sum_i c_i \Sigma_i(z, \cos\hat{\theta}) \right] dz\, d\cos\hat{\theta}. \tag{38b}$$

The inverse covariance matrix is then obtained by replacing $\Sigma_{\{{\rm SM},i\}}(\Phi_3)$ by $\Sigma_{\{{\rm SM},i\}}(z, \cos\hat{\theta})$ in Eq. (26), and $d\Phi_3$ by $dz\, d\cos\hat{\theta}$.

When $f = \nu_e$, ν_μ or ν_τ, we can measure neither p_1 nor p_2, but only the sum $p_1 + p_2$ from the four-momentum conservation. In this case, only the Higgs-boson energy and momentum are observable when Higgs boson decays to $b\bar{b}$ pair, and the observable cross section in the laboratory frame is

$$d\sigma = B(H \to b\bar{b}) \left[\Sigma_{\rm SM}(E_H, \cos\theta_H) + \sum_i c_i \Sigma_i(E_H, \cos\theta_H) \right] dE_H\, d\cos\theta_H. \tag{39}$$

The covariance matrix is obtained by using the above distributions. In practice, the Higgs-boson energy E_H from ZH production is peaked in the region

$$|m_{\nu\bar{\nu}} - m_Z| = |(s + m_H^2 - 2\sqrt{s}E_H)^{1/2} - m_Z| < 5\Gamma_Z, \tag{40}$$

and only the $\cos\theta_H$ dependence of the distributions is effective.

In the case of $f = \nu_e$, in addition, the W boson fusion diagram in Fig. 2(b) contributes. Since this amplitude is rather large at high energies, $\sqrt{s} \gtrsim 500$ GeV, we make a careful study of the W-fusion contribution by using the Higgs-boson rapidity y_H and the transverse momentum p_{TH};

$$d\sigma = B(H \to b\bar{b}) \left[\Sigma_{\rm SM}(y_H, p_{TH}) + \sum_i c_i \Sigma_i(y_H, p_{TH}) \right] dy_H\, dp_{TH}. \tag{41}$$

The W-fusion events are selected by requiring

$$|m_{\nu\bar{\nu}} - m_Z| = |(s + m_H^2 - 2\sqrt{s}E_H)^{1/2} - m_Z| > 5\Gamma_Z, \tag{42}$$

and in order to avoid contamination with the $\gamma\gamma$ fusion events, we impose an additional constraint

$$p_{TH} > 10 \text{ GeV}. \tag{43}$$

When $f = q = u, d, s, c, b$ we cannot distinguish f from $\bar{f}$ efficiently. In Ref. [13], impacts of partial identification of b from $\bar{b}$ have been studied, and they are found to be negligibly small. In this study, therefore, we do not distinguish q from $\bar{q}$ at all, and we do not distinguish quark flavors. In this limit, the hadronic decays of the Z boson gives two jets with momenta p_1 and p_2 for q and $\bar{q}$, respectively, but we cannot distinguish the events from those where q jet has the momentum p_2 and $\bar{q}$ jet has p_1. The appropriate optimal observables are then obtained as follows:

$$d\sigma = \frac{1}{2} \left\{ \Sigma_{\rm SM}(\Phi_3) + \Sigma_{\rm SM}(\tilde{\Phi}_3) + \sum_i c_i [\Sigma_i(\Phi_3) + \Sigma_i(\tilde{\Phi}_3)] \right\} d\Phi_3, \tag{44}$$

where $\tilde{\Phi}_3$ is obtained from the phase-space point Φ_3 by interchanging p_1 and p_2. The three-body phase-space volume $d\Phi_3$ is divided by 2 in order to account for the double counting. The inverse covariance matrix is calculated as in Eq. (26), while Σ's are replaced by $\Sigma(\Phi) + \Sigma(\tilde{\Phi})$, and the phase-space measure is divided by 2.

C. Cross section for each process

Before we start examining the above processes one by one, we present here the total cross section of all the five processes for $m_H = 120$ GeV in Fig. 3 as a function of the c.m. energy $\sqrt{s}$. All the curves show the SM prediction, which are obtained by setting all c_i to zero. As for $e^+e^- \to ZH$, we plot the cross section for the sum of all the Z boson decay modes when $|m_{f\bar{f}} - m_Z| < 5\Gamma_Z$. The $\Gamma_Z = 0$ limit

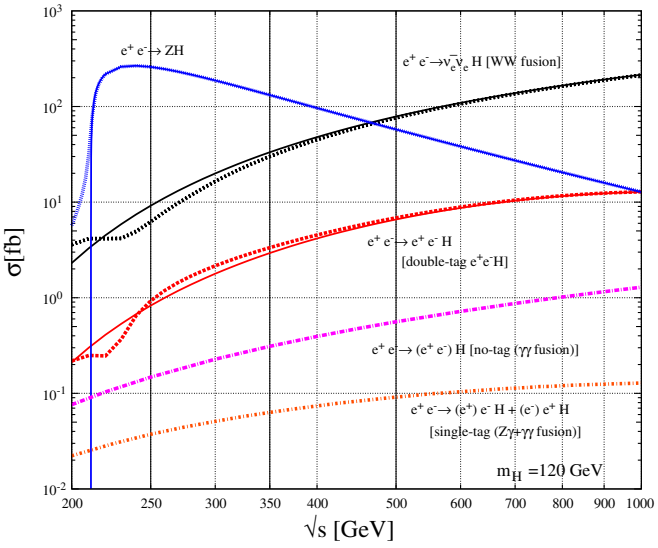

FIG. 3 (color online). Total cross sections versus e^+e^- collision energy $\sqrt{s}$ for the five processes that are sensitive to the HVV couplings at ILC. All the curves are for $m_H = 120$ GeV. The ZH production cross section is the sum over all $Z \to f\bar{f}$ decay modes with $|m_{\nu\bar{\nu}} - m_Z| < 5\Gamma_Z$, while the solid thin curves show the $\Gamma_Z = 0$ limit. The $\nu\bar{\nu}H$ and the double-tag e^+e^-H events satisfy $|m_{f\bar{f}} - m_Z| > 5\Gamma_Z$, and the tagged $e^\pm$ has $|\cos\theta_{e^\pm}| < 0.995$ and $p_{Te^\pm} > 1$ GeV, while $p_{TH} > 10$ GeV is imposed on $\nu\bar{\nu}H$ process. The solid thin curves for $e^+e^- \to \nu_e\bar{\nu}_eH$ and $e^+e^- \to e^+e^-H$ give the cross sections calculated from the t-channel W and Z-boson exchange amplitudes only without imposing the invariant mass cut.

result is given by the thin curve. The cross section for $e^+e^- \to \nu_e\bar{\nu}_eH$ is obtained by requiring $|m_{\nu\bar{\nu}} - m_Z| > 5\Gamma_Z$, Eq. (42), and $p_{TH} > 10$ GeV, Eq. (43), in order to suppress the contribution from $Z \to \nu\bar{\nu}$ and $\gamma\gamma \to H$, respectively. The contribution from the WW fusion (t-channel W exchange) process only without the $m_{\nu\bar{\nu}}$ cut is given by the thin curve, in order to show the relevance of the interference effects and the $m_{\nu\bar{\nu}}$ cut at low energies. The cross section for the process $e^+e^- \to e^+e^-H$ is separated into four cases; $Z \to e^+e^-$ ($|m_{ee} - m_Z| < 5\Gamma_Z$), double-tag ($|m_{ee} - m_Z| > 5\Gamma_Z$), single-tag and no-tag events, where the final e^+ and e^- are tagged when $|\cos\theta_{e^\pm}| < 0.995$ and $p_{Te^\pm} > 1$ GeV. The thin curve for the double-tag e^+e^-H cross section gives the contribution from the ZZ fusion only without the m_{ee} cut. The sign of the interference effect is opposite between the $\nu_e\bar{\nu}_eH$ and e^+e^-H process, because of the opposite relative sign of the coupling factors between the t-channel and s-channel amplitudes. In addition, when $\sqrt{s} \lesssim m_H + m_Z + 5\Gamma_Z$, only the $m_{f\bar{f}} - m_Z < 0$ region contribute with positive (negative) interference in $\nu_e\bar{\nu}_eH$ (e^+e^-H) events, while at high $\sqrt{s}$ the negative (positive) interference from the $m_{f\bar{f}} - m_Z > 0$ region dominates because the magnitude of the t-channel amplitudes grow with $m_{f\bar{f}}$.

For the SM cross sections, we use the physical masses, $m_W = 80.423$ GeV, and $m_Z = 91.1876$ GeV [2], and the $\overline{\rm MS}$ couplings at the m_Z scale, $\hat{\alpha}(m_Z) = 1/128.0$ and $\sin^2\hat{\theta}_W(m_Z) = 0.2312$ for the gauge couplings, except when we use the equivalent real photon distribution, which is evaluated with $\alpha = 1/137$. All the calculations are done in the leading order of the perturbation theory, since none of our results (errors and correlations) are sensitive to small differences in the cross sections. We leave the important task of evaluating the impacts of initial state radiation, both from bremsstrahlung and beamstrahlung, for future studies.

We study the significance of each process in constraining the HVV couplings quantitatively at four representative energies, $\sqrt{s} = 250$, 350, 500 GeV, and 1 TeV. The statistical errors are estimated for a nominal integrated luminosity of $L_0 = 100$ fb^{-1} at each energy. For $\sqrt{s} = 250$ and 350 GeV, we consider only the ZH, $\nu_e\bar{\nu}_eH$ and double-tag e^+e^-H processes, because the single-tag and no-tag e^+e^-H cross sections do not give sufficient number of events in the SM. It should be noted that the WW fusion overtakes the ZH production contribution at $\sqrt{s} = 500$ GeV, and even the cross section of the double-tag eeH events from ZZ fusion becomes comparable to that of the ZH production at $\sqrt{s} = 1$ TeV. The single and no-tag e^+e^-H events, which are sensitive to the $HZ\gamma$ and $H\gamma\gamma$ couplings, respectively, give sufficiently large cross sections only at $\sqrt{s} = 500$ GeV and 1 TeV. When we combine results from all the processes and from all the energies, we examine the impacts of higher luminosity, by giving $L = 500$ fb^{-1} at $\sqrt{s} = 500$ GeV and at $\sqrt{s} = 1$ TeV.

The total cross sections are shown in Fig. 4 as functions of the Higgs-boson mass between 100 GeV and 200 GeV for (a) $\sqrt{s} = 250$ GeV, (b) 500 GeV and (c) 1 TeV. The cross sections do not depend strongly on m_H for $m_H < 200$ GeV, except for the dominant ZH production cross section at $\sqrt{s} = 250$ GeV, which drops sharply from 100 fb at $m_H \sim 150$ GeV down to 1 fb at $m_H = 165$ GeV, and vanishes at $m_H = \sqrt{s} - m_Z + 5\Gamma_Z \sim 170$ GeV because of the final state cut $|m_{f\bar{f}} - m_Z| < 5\Gamma_Z$; see Eq. (30). The thin curve shows the zero-width limit. The ZH production process is dominant up to $m_H \sim 165$ GeV, above which the WW-fusion process becomes a main process, and its cross section is above $\sim$1 fb up to $m_H \sim 180$ GeV.

In Fig. 4(a), we show two curves for the $\nu_e\bar{\nu}_eH$ and double-tag eeH processes. The thick curves gives the cross sections when the $Z \to f\bar{f}$ exclusion cut Eq. (42) is applied, and hence they may be regarded as those of WW and ZZ fusion events. On the other hand, the thin curves give the total cross sections without the $Z \to f\bar{f}$ exclusion cut, and hence they receive contribution from the ZH production amplitudes with $Z \to \nu_e\bar{\nu}_e$ or e^+e^- transitions. Along the thick curves for the WW and ZZ fusion events, the

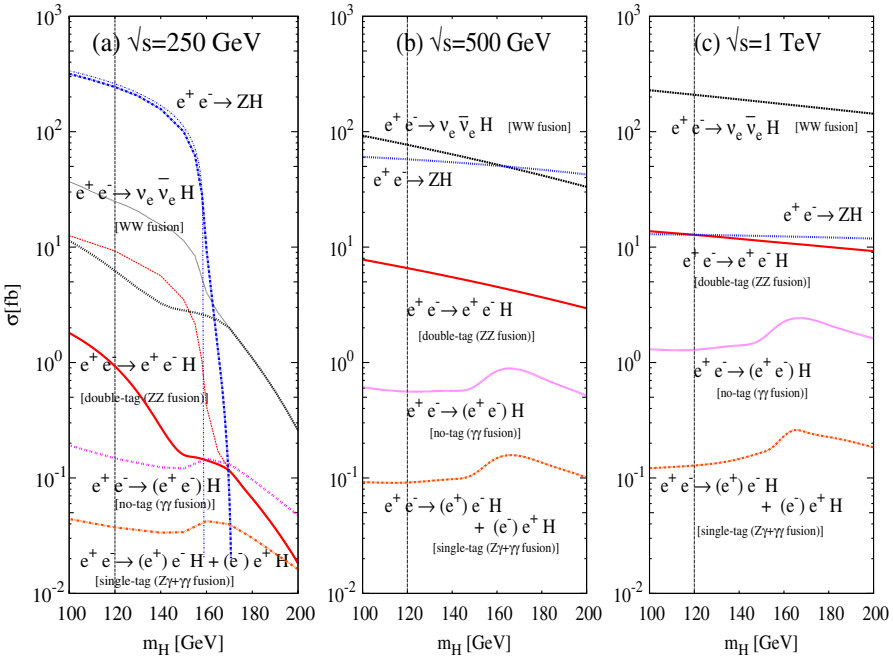

FIG. 4 (color online). Total cross sections versus m_H for the five processes, which are sensitive to the HVV couplings at ILC, at (a) $\sqrt{s} = 250$ GeV, (b) 500 GeV, and (c) 1 TeV. The tagged $e^{\pm}$ has $|\cos\theta_{e^{\pm}}| < 0.995$ and $p_{Te^{\pm}} > 1$ GeV in the laboratory frame. $|m_{f\bar{f}} - m_Z| < 5\Gamma_Z$ for ZH production and $|m_{f\bar{f}} - m_Z| > 5\Gamma_Z$ for $\nu_e\bar{\nu}_e H$ and double-tag e^+e^-H. The thin curves in (a) for $\nu\bar{\nu}H$ and e^+e^-H show the cross sections when the $Z \to f\bar{f}$ exclusion cut is removed, and that for ZH shows the $\Gamma_Z = 0$ limit. $p_{TH} > 10$ GeV is imposed on $\nu\bar{\nu}H$ process.

exclusion cut affects the fusion cross sections below $m_H = 170$ GeV $\sim \sqrt{s} - m_Z + 5\Gamma_Z$, which remain almost constant down to $m_H = 150$ GeV $\sim \sqrt{s} - m_Z - 5\Gamma_Z$, where the increase of the overall phase space is compensated by the increase in the cutout phase-space region.

At $\sqrt{s} = 500$ GeV in Fig. 4(b), all the cross sections of the t-channel processes increase, and that of the s-channel ZH production process decreases. The ZH production and the WW-fusion processes have almost the same cross section, over 30 fb up to $m_H = 200$ GeV, and the cross section of the double-tag eeH event is about 1 order of magnitude smaller than that of $\nu_e\bar{\nu}_e H$. The cross sections of the no-tag and the single-tag eeH events are still small, whose maximum is 1 fb and 0.2 fb, respectively, for $m_H \sim 2m_W$, where the one-loop $H\gamma\gamma$ and $HZ\gamma$ vertices receive the W pair threshold enhancement.

At $\sqrt{s} = 1$ TeV in Fig. 4(c), the cross section of the WW-fusion process is above 100 fb, while those of the ZH production and the double-tag eeH processes are $\sim$10 fb, almost independent of m_H up to $m_H = 200$ GeV. As in Fig. 4(b) for $\sqrt{s} = 500$ GeV, the cross section of the no-tag and single-tag eeH processes take the maximum values of 2 fb and 0.2 fb, respectively, around $m_H \sim 2m_W$.

IV. $e^+e^- \to \nu_e\bar{\nu}_e H$ WW-FUSION PROCESS

The HWW coupling is best measured in WW-fusion production of the Higgs boson, see Fig. 2(b), in the process

$$e^-\left(k_1, \frac{\sigma_1}{2}\right) + e^+\left(k_2, \frac{\sigma_2}{2}\right) \to \nu_e\left(p_1, \frac{\lambda_1}{2}\right) + \bar{\nu}_e\left(p_2, \frac{\lambda_2}{2}\right) + H(p_H), \tag{45}$$

where k_i and p_i denote four momenta of each particles, $\sigma_i/2$ demote $e^{\pm}$ helicities, and $\lambda_i/2$ demote ν_e or $\bar{\nu}_e$ helicities. The WW-fusion process contribute only to one helicity amplitude, $\sigma_1 = -\sigma_2 = \lambda_1 = -\lambda_2 = -$. Contamination of the HZZ couplings via s-channel ZH production followed by $Z \to \nu\bar{\nu}$ decays, see Fig. 2(a), can be avoided by choosing suitable cuts on the observed Higgs-boson energy Eq. (40). Therefore, the process with "a Higgs + missing energy" in e^+e^- annihilation can probe HWW couplings independently of the other vector-boson couplings. Once the branching fraction of $H \to WW^*$ decay is known, the measurement of the HWW coupling determines the total decay width of the Higgs boson in a model-independent manner. It then allows us to translate all the Higgs-boson branching ratio measurements into the measurements of the partial widths, from which we can determine the magnitude of various Higgs-boson couplings. It is also worth repeating here, that the sensitivity of the HWW coupling measurement is expected to be better at high energies, because the cross section grows as $\log(s/m_H^2)$ with energy, in contrast to the ZH production cross section, which decreases as $1/s$; see Fig. 3.

A. Helicity amplitudes and backgrounds

The helicity amplitudes for the process given in Eq. (45) can be written as

$$M^{\lambda_1\lambda_2}_{\sigma_1\sigma_2} = \frac{g_W^2}{2}\delta_{\sigma_1-}\delta_{\sigma_2+}\delta_{\lambda_1-}\delta_{\lambda_2+} j^{\mu}_{e^-(\sigma_1,\lambda_1)}\Gamma^{HWW}_{\mu\nu} j^{\nu}_{e^+(\sigma_2,\lambda_2)} \times D_W(t_1)D_W(t_2), \quad (46)$$

where $D_W(t_i) = 1/(t_i - m_W^2)$ are the propagator factors with $t_i = (k_i - p_i)^2$, $(i = 1, 2)$ and

$$j^{\mu}_{e^-(-,-)} = \bar{u}\left(p_1, -\frac{1}{2}\right)\gamma^{\mu}P_L u\left(k_1, -\frac{1}{2}\right), \quad (47a)$$

$$j^{\nu}_{e^+(+,+)} = \bar{v}\left(p_2, +\frac{1}{2}\right)\gamma^{\nu}P_L v\left(k_2, +\frac{1}{2}\right), \quad (47b)$$

are the leptonic charged currents. The explicit form of the nonzero components of the massless currents in the laboratory frame are given in Eqs. (B1) in Appendix B. The HWW coupling can be read from Eqs. (13) and (17) and expressed as

$$\Gamma^{HWW}_{\mu\nu} = g_Z m_Z\Big[\Big\{1 + c_{1WW} - \frac{2}{m_Z^2}\Big(\frac{1}{2}(m_H^2 - t_1 - t_2)c_{2WW} - m_H^2 c_{3WW}\Big)\Big\}g^{\mu\nu} + \frac{2}{m_Z^2}(c_{2WW} - c_{3WW})q_{2\mu}q_{1\nu}\Big], \quad (48)$$

where $q_i^{\mu} = k_i^{\mu} - p_i^{\mu}$ $(i = 1, 2)$. By contracting the t-channel currents with the generalized HWW vertex using Eqs. (B2) in Appendix B, we can write the helicity amplitude (46) as

$$M^{-+}_{-+} = M_{\rm SM}\Big[1 + c_{1WW} + \frac{1}{m_Z^2}\Big\{c_{2WW}\Big(t_1 + t_2 - m_H^2 + \frac{s\mathcal{G}}{4}\Big) + c_{3WW}\Big(2m_H^2 - \frac{s\mathcal{G}}{4}\Big)\Big\}\Big], \quad (49)$$

where

$$M_{\rm SM} = \frac{g_W^3 m_W}{2}D_W(t_1)D_W(t_2)\mathcal{F}(\theta_1,\theta_2), \quad (50a)$$

$$\mathcal{F}(\theta_1,\theta_2) = 2s\sqrt{x_1x_2}\cos\frac{\theta_1}{2}\sin\frac{\theta_2}{2}, \quad (50b)$$

$$\mathcal{G}(\theta_1,\theta_2,\phi) = \Big[2 - x_1(1+\cos\theta_1) + x_1\sin\theta_1\cot\frac{\theta_2}{2}e^{-i\phi}\Big] \times\Big[2 - x_2(1-\cos\theta_2) + x_2\sin\theta_2\tan\frac{\theta_1}{2}e^{i\phi}\Big]. \quad (50c)$$

Here, $\phi = \phi_1 - \phi_2$, and x_i, θ_i, ϕ_i are the energy fraction, polar, and azimuthal angles, respectively, of ν_e $(i = 1)$ and $\bar{\nu}_e$ $(i = 2)$ in the laboratory frame; see Eq. (A1) in Appendix A.

The SM contribution to the squared matrix element is

$$F_{\rm SM} = |M^{-+}_{\rm SM-+}|^2 = |M_{\rm SM}|^2 = \frac{g^6 m_W^2}{4}|D_W(t_1)D_W(t_2)\mathcal{F}(\theta_1,\theta_2)|^2, \quad (51)$$

and the distributions F_i for each nonstandard effective couplings are

$$F_{c_{1WW}} = 2\,\mathrm{Re}[M_{c_{1WW}-+}{}^{-+}(M_{\rm SM-+}{}^{-+})^{\star}] = 2F_{\rm SM}, \quad (52a)$$

$$F_{c_{2WW}} = 2\,\mathrm{Re}[M_{c_{2WW}-+}{}^{-+}(M_{\rm SM-+}{}^{-+})^{\star}] = \frac{2}{m_Z^2}\Big[t_1 + t_2 - m_H^2 + \frac{s}{4}\,\mathrm{Re}\mathcal{G}\Big]F_{\rm SM}, \quad (52b)$$

$$F_{c_{3WW}} = 2\,\mathrm{Re}[M_{c_{3WW}-+}{}^{-+}(M_{\rm SM-+}{}^{-+})^{\star}] = \frac{2}{m_Z^2}\Big[2m_H^2 - \frac{s}{4}\,\mathrm{Re}\mathcal{G}\Big]F_{\rm SM}. \quad (52c)$$

As explained in Sec. III, since we cannot observe ν_e and $\bar{\nu}_e$ momenta, we cannot make use of all the distributions F_i in Eq. (52) to constrain the couplings c_{iWW}. In fact, we can measure only the Higgs-boson momenta, E_H and $\cos\theta_H$, or p_{TH} and y_H. In order to obtain the observable weight functions, we perform the integration over the ν_e and $\bar{\nu}_e$ momenta by using the 3-body phase-space parametrization in Eq. (A8c) as

$$d\Phi_3 = \frac{\sqrt{s}}{512\pi^4}\bar{\beta}\Big(\frac{m^2_{\nu\bar{\nu}}}{s}, \frac{m_H^2}{s}\Big)d(\cos\theta^*)d\phi^* dp_{TH}dy_H, \quad (53)$$

where $m^2_{\nu\bar{\nu}} = s + m_H^2 - 2\sqrt{s}E_H$, and $E_H = \sqrt{p_{TH}^2 + m_H^2}$. The observable differential cross section with initial e^- and e^+ beam polarizations P and $\bar{P}$, respectively, is

$$\frac{d^2\sigma(P,\bar{P})}{dy_H dp_{TH}} = B(H\to b\bar{b})\Big[\Sigma_{\rm SM}(P,\bar{P};y_H,p_{TH}) + \sum_i c_i\Sigma_{c_i}(P,\bar{P};y_H,p_{TH})\Big]. \quad (54)$$

Since only the left-handed e^- and right-handed e^+ contribute to the cross section, the weight functions are

$$\Sigma_i(P,\bar{P};y_H,p_{TH}) = \frac{1}{2s}\Big(\frac{1-P}{2}\Big)\Big(\frac{1+\bar{P}}{2}\Big) \times \frac{1}{512\pi^4}\bar{\beta}\Big(\frac{m_{ff}^2}{s}, \frac{m_H^2}{s}\Big) \times \int F_i(x_1,x_2,\theta_1,\theta_2,\phi)d\cos\theta^* d\phi^*, \quad (55)$$

where $i = \mathrm{SM}$, c_{1WW}, c_{2WW}, and c_{3WW}. The covariance matrix for the measurements of $c_i = c_{1WW}$, c_{2WW}, c_{3WW} with an integrated luminosity of $L_{(P,\bar{P})}$ is now expressed as

$$[V^{-1}_{(P,\bar{P})}]_{ij} = B(H \to b\bar{b}) L_{(P,\bar{P})} \int \frac{\Sigma_i(P,\bar{P};y_H,p_{TH})\Sigma_j(P,\bar{P};y_H,p_{TH})}{\Sigma_{SM}(P,\bar{P};y_H,p_{TH})} dy_H dp_{TH}. \quad (56)$$

In the following numerical studies, we set $B(H \to b\bar{b}) = 0.9$ for the branching fraction at $m_H = 120$ GeV.

Before proceeding to the sensitivity analysis of the anomalous couplings, we briefly remind ourselves of the potential backgrounds to this measurement.

(1) No tag events in the process $e^+e^- \to e^+e^-H$ via the t-channel $\gamma\gamma$, γZ or ZZ fusion contribute, but the Higgs boson cannot have large p_{TH} in order for the $e^\pm$ to escape detection. We impose a selection cut $p_{TH} > 10$ GeV, Eq. (43), which is sufficient to suppress the no-tag $(ee)H$ contribution even at $\sqrt{s} \sim 1$ TeV. Contribution from $\gamma\gamma$ fusion is negligibly small at $p_T \gtrsim$ a few GeV, as we will show in Sec. VII, and that from ZZ fusion is estimated to about 5.4%, 4.8%, and 3.9% of the signal, respectively, in the three smallest p_{TH} bins, 10–20, 20–30, and 30–40 GeV at $\sqrt{s} = 1$ TeV.

(2) The s-channel ZH production process, where the Z boson decays into a $\nu\bar{\nu}$ pair, can also be a background to this measurement at low energies. Since the background events have missing mass peaked at m_Z, we impose the E_H cut, Eq. (42), which removes those events whose missing mass lies within $5\,\Gamma_Z$ of the Z boson mass.

Although a small number of background events will survive the above cuts, especially in the presence of initial state radiation and finite detector resolution, we expect that their effect can be controlled and that they will not affect the main conclusions of the following analysis.

B. Sensitivity analysis of the HWW couplings

1. Sensitivity at ILC-I for $\sqrt{s} = 500$ GeV

We first perform the binned analysis for single and double distribution at $\sqrt{s} = 500$ GeV. Since the weight functions of Eq. (54) depend only on y_H and p_{TH}, we calculate the expected number of events in a (y_H, p_{TH}) bin with the bin width of $\Delta y_H = 0.05$ and $\Delta p_{TH} = 10$ GeV.

We show in Fig. 5 the weight functions Σ's integrated over the rapidity, y_H. This plot shows that the contribution from the operators corresponding to the couplings, c_{1WW}, c_{2WW}, and c_{3WW} can in principle be differentiated by using the p_{TH} distribution, because they have different shapes. $\Sigma_{c_{1WW}}$ and $\Sigma_{c_{3WW}}$ has a peak at different p_{TH}, while $\Sigma_{c_{2WW}}$ changes sign. It is not clear, however, how well they can be distinguished.

The covariance matrix method gives a quantitative answer to this question. Using the p_{TH} distribution, we obtain the matrix elements of the inverse covariance matrix as

$$(V^{-1})_{ij} = B(H \to b\bar{b}) L_0 \sum_k \frac{\Sigma_i(p_{TH}{}^{(k)})\Sigma_j(p_{TH}{}^{(k)})}{\Sigma_{SM}(p^k_{TH})} \Delta p_{TH}, \quad (57)$$

where $p_{TH}{}^{(k)}$ denotes the center of each p_{TH} bin. Since the covariance matrix is the same for the unpolarized case $P = \bar{P} = 0$, and for the polarized e^- beam case with equipartition of the total luminosity into $P = |P|$ and $P = -|P|$, as in Eq. (29), we show our results without specifying the beam polarization. It should be noted, that, because of the simple polarization dependence of the WW fusion cross section, as shown in Eq. (55), the covariance matrix for the general case of asymmetric partition of the total luminosity is simply obtained by adjusting an overall normalization factor, which is proportional to the total number of events.

We find for $\sqrt{s} = 500$ GeV and $L_0 = 100$ fb^{-1},

$$\begin{matrix} \Delta c_{1WW} = \pm.15 \\ \Delta c_{2WW} = \pm.16 \\ \Delta c_{3WW} = \pm.045 \end{matrix} \begin{pmatrix} 1 & & \\ .9986 & 1 & \\ .9989 & .9982 & 1 \end{pmatrix}. \quad (58)$$

We observe that the magnitudes of the correlation matrix elements are quite large, implying that there is at least one combination of the three couplings that cannot be measured accurately as compared with the others. In order to identify which combination of the couplings are measured accurately and inaccurately, we obtain the eigenvalues λ_i and the associated eigenvector $\vec{a}_i$ of the covariance matrix, in terms of which V^{-1} and V are expressed as

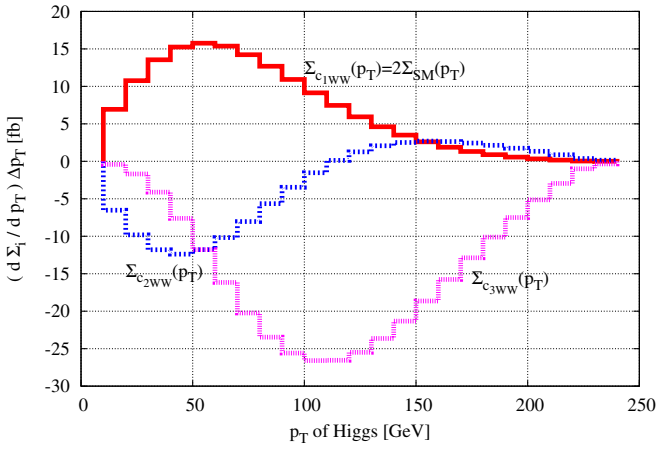

FIG. 5 (color online). Histogram showing the p_T distributions of the Higgs boson, where the differential cross section is integrated over y_H in each p_{TH} bin of 10 GeV width at $\sqrt{s} = 500$ GeV for $m_H = 120$ GeV. Σ_{SM} gives the SM distribution, and Σ_{c_i} shows the coefficients of the nonstandard HWW couplings $c_i = (c_{1WW}, c_{2WW}, c_{3WW})$.

$$V^{-1} = \sum_i \lambda_i^{-1} \vec{a}_i \vec{a}_i^T, \quad \text{or} \quad V = \sum_i \lambda_i \vec{a}_i \vec{a}_i^T. \tag{59}$$

The resolving power of the measurements can be studied best by showing the eigenvectors and their errors $\pm\sqrt{\lambda_i}$,

$$.22c_{1WW} + .061c_{2WW} - .97c_{3WW} = \pm.0020, \tag{60a}$$
$$.69c_{1WW} - .71c_{2WW} + .12c_{3WW} = \pm.0058, \tag{60b}$$
$$.68c_{1WW} + .70c_{2WW} + .20c_{3WW} = \pm.22. \tag{60c}$$

As anticipated, we find that the error of the combination (60c) is 2 orders of magnitude larger than those of the other two. In fact, if we sum over the weight functions given in Eq. (55), for the combination of Eq. (60c), we find that the sum almost cancels out and hence this combination is poorly measured.

As above, whenever the correlation matrix elements are large, the eigenvectors and their errors reveal much more information. Henceforth, we present our results in terms of the eigenvectors and their errors of the covariance matrix V, whenever they are more informative.

In order to obtain the maximum information from experiments, we further study the two-dimensional distributions of y_H and p_{TH} variables. We present the scatter plots of the weight functions of c_{1WW}, c_{2WW}, and c_{3WW} in Figs. 6(a)–6(c), respectively, on the y_H, p_{TH} plane. We find that adding the rapidity distribution does not help much in resolving the degeneracy, because the y_H dependence of the weight functions for c_{1WW}, c_{2WW}, and c_{3WW} are all similar. Only Fig. 6(b) gives some hint of an additional independent measurement as it has nonfactorizable dependencies in terms of y_H and p_{TH}, unlike the other two cases.

By using the double differential distributions, we obtain the optimal covariance matrix from

$$(V^{-1})_{ij} = B(H \to b\bar{b}) L_0 \times \sum_{l,m} \left[\frac{\Sigma_i(y_H^{(l)}, p_{TH}{}^{(m)}) \Sigma_j(y_H^{(l)}, p_{TH}{}^{(m)})}{\Sigma_{SM}(y_H^{(l)}, p_{TH}{}^{(m)})} \Delta y_H \Delta p_{TH} \right], \tag{61}$$

where we set the bin size $\Delta y_H = 0.1$ and $\Delta p_{TH} = 20$ GeV. For the cross section of 77 fb (see Fig. 3) at $\sqrt{s} = 500$ GeV, we expect 7700 events with $L_0 = 100$ fb^{-1}, when e^- and e^+ beams are unpolarized, $P = \bar{P} = 0$. The eigenvectors and their errors are

$$.24c_{1WW} + .045c_{2WW} - .97c_{3WW} = \pm.0020, \tag{62a}$$
$$.69c_{1WW} - .71c_{2WW} + .13c_{3WW} = \pm.0059, \tag{62b}$$
$$.68c_{1WW} + .70c_{2WW} + .20c_{3WW} = \pm.15, \tag{62c}$$

or in the standard representation

$$\begin{matrix} c_{1WW} = \pm.099 \\ c_{2WW} = \pm.10 \\ c_{3WW} = \pm.029 \end{matrix} \begin{pmatrix} 1 & & \\ .997 & 1 & \\ .997 & .995 & 1 \end{pmatrix}. \tag{63}$$

When we compare the optimal result (63) with the previous one (58) that used only the p_{TH} distribution, we find more than 30% improvements in the errors of all the couplings and slight decrease in the correlations. While by comparing the eigenvectors and their errors of the optimal results (62) with (60), we find that the only effect of using the additional information is to reduce the error of the least constrained combination by about 30%. Neither the eigenvectors nor the errors of the two accurately constrained combinations are affected much by the optimization.

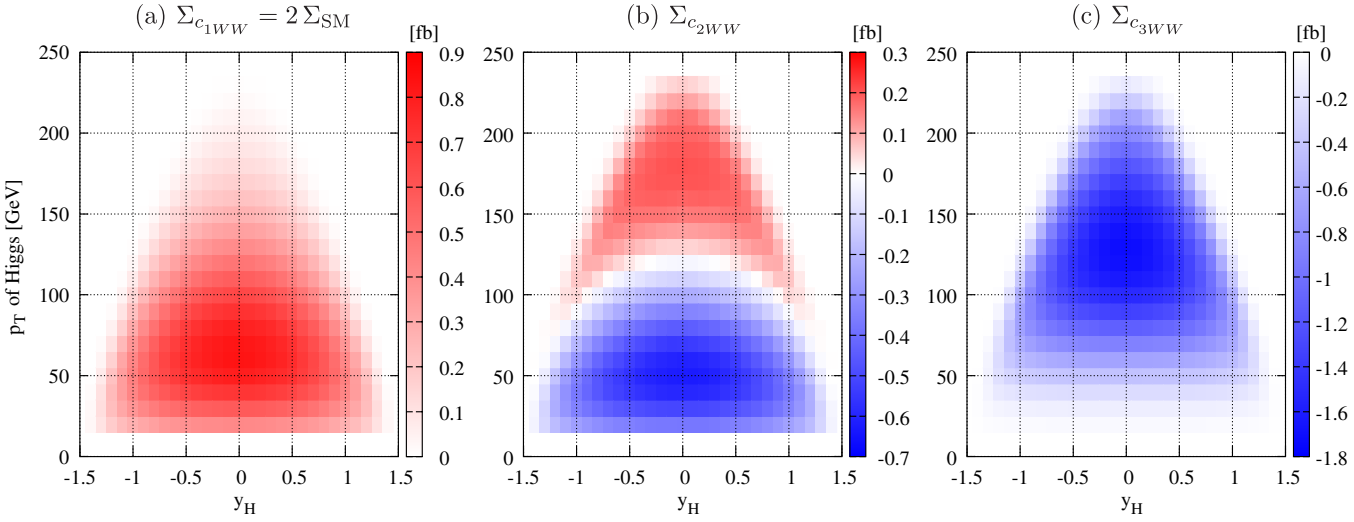

FIG. 6 (color online). Scatter plot in the y_H-p_{TH} plane for the coefficient of (a) c_{1WW}, (b) c_{2WW}, and (c) c_{3WW}. The measure gives $(d^2\sigma/dy_H dp_{TH})\Delta y_H \Delta p_{TH}$ in units of fb for the bin size of $p_{TH} = 10$ GeV and $y_H = 0.05$, at $\sqrt{s} = 500$ GeV for $m_H = 120$ GeV.

2. Sensitivity at $\sqrt{s} = 250$ GeV and 350 GeV with t channel only

The cross section for the WW fusion is small at lower energies; 9.2 fb at $\sqrt{s} = 250$ GeV and 33.2 fb at 350 GeV as can be seen from the solid thin curve in Fig. 3, which further reduces to 5.8 fb and 31.4 fb, respectively, after imposing the $Z \to \nu\bar{\nu}$ exclusion cut $|m_{\nu\bar{\nu}} - m_Z| > 5\Gamma_Z$. Not only the cross section is small but also contributions from the ZH production amplitudes and the interference terms, as well as the effects due to the $Z \to \nu\bar{\nu}$ exclusion cut, are significant at low energies, as can be seen from the dashed thick curve in Fig. 3. We first show the results of "theoretical" studies based on the WW fusion events only, which helps us understand the energy dependence of the WW fusion amplitudes when compared with the results at $\sqrt{s} = 500$ GeV and 1 TeV. A more realistic study will be given in the next subsection.

At $\sqrt{s} = 250$ GeV, we will have only 580 events from WW fusion with $L_0 = 100$ fb^{-1} and with 100% efficiency. Thus, our integral approximation for the covariance matrix, Eq. (56), may not be reliable. In order to examine the sensitivity of our results on the bin size, we enlarge the bin size to $\Delta y_H = 0.15$ and $\Delta p_{TH} = 30$ GeV and count only the contributions from these bins with more than 10 events for the nominal luminosity of $L_0 = 100$ fb^{-1}. We find the eigenvectors and their 1σ errors at $\sqrt{s} = 250$ GeV with $L_0 = 100$ fb^{-1} and $P = \bar{P} = 0$ to be

$$.61c_{1WW} - .045c_{2WW} - .79c_{3WW} = \pm.016, \quad (64a)$$

$$.58c_{1WW} - .65c_{2WW} + .49c_{3WW} = \pm.029, \quad (64b)$$

$$.54c_{1WW} + .76c_{2WW} + .38c_{3WW} = \pm1.1. \quad (64c)$$

We observe that the nature of the eigenvectors are similar to those at $\sqrt{s} = 500$ GeV in Eq. (62), and also the hierarchy between the largest error and the other two persist. The overall magnitude of the errors are larger than those of Eq. (62) at $\sqrt{s} = 500$ GeV by a factor of 8, half of which can be attributed to the reduction of the cross section by a factor of $13.5 \sim (3.7)^2$. We confirm that both the eigenvectors and the eigenvalues of Eq. (64) obtained with the large bin size do not differ much from those in the integral (infinitesimal bin size) limit. The errors of the two most accurately measured combinations are especially insensitive to the details of our binning procedure.

We also examine the case at $\sqrt{s} = 350$ GeV with $L_0 = 100$ fb^{-1}, since it is natural to study the top-quark property in detail near the $t\bar{t}$ threshold. We will have about 3140 events, and the eigenvectors and their 1σ errors for $P = \bar{P} = 0$ are

$$.44c_{1WW} - .068c_{2WW} - .89c_{3WW} = \pm.0050, \quad (65a)$$

$$.63c_{1WW} - .68c_{2WW} + .37c_{3WW} = \pm.011, \quad (65b)$$

$$.63c_{1WW} + .73c_{2WW} + .26c_{3WW} = \pm.44. \quad (65c)$$

Again, we observe the similar hierarchy pattern.

3. Sensitivity at $\sqrt{s} = 250$ GeV and 350 GeV with ZH interference

Since the cross sections of t-channel WW fusion process are small at $\sqrt{s} = 250$ and 350 GeV, contribution from the ZH production amplitudes is rather significant despite the $Z \to \nu\bar{\nu}$ exclusion cut $|m_{\nu\bar{\nu}} - m_Z| > 5\Gamma_Z$. At $\sqrt{s} = 250$ GeV, the cross section grows from 5.8 fb to 6.2 fb mainly because of the 0.7 fb contribution from the s-channel amplitude squared, which overcomes the -0.3 fb contribution from the destructive interference between the t-channel and s-channel amplitudes. On the other hand, the cross section at $\sqrt{s} = 350$ GeV decreases slightly from 31.4 fb to 30.1 fb because of the destructive interference. In addition, ZH production followed by $Z \to \nu_\mu\bar{\nu}_\mu$ and $Z \to \nu_\tau\bar{\nu}_\tau$ contributes with 1.4 fb at $\sqrt{s} = 250$ GeV, and 1.0 fb at $\sqrt{s} = 350$ GeV, after the $Z \to \nu\bar{\nu}$ exclusion cut. These events are experimentally indistinguishable from the WW fusion $\nu_e\bar{\nu}_e H$ process. Therefore, the total cross sections become 7.6 fb and 31.1 fb at $\sqrt{s} = 250$ GeV and 350 GeV, respectively.

We show in Fig. 7 the p_{TH} distribution of the SM, $\Sigma_{\rm SM}$, and the weight functions Σ_i at $\sqrt{s} = 250$ GeV. The thin lines show the WW fusion contribution only, which are the y_H integral of the two-dimensional weight functions used to obtain the results of Eqs. (64) and (65). The thick dashed lines are obtained after the interference between the t-channel WW fusion and the s-channel ZH production amplitudes are taken into account. Since we can safely neglect the nonstandard contributions in the subdominant

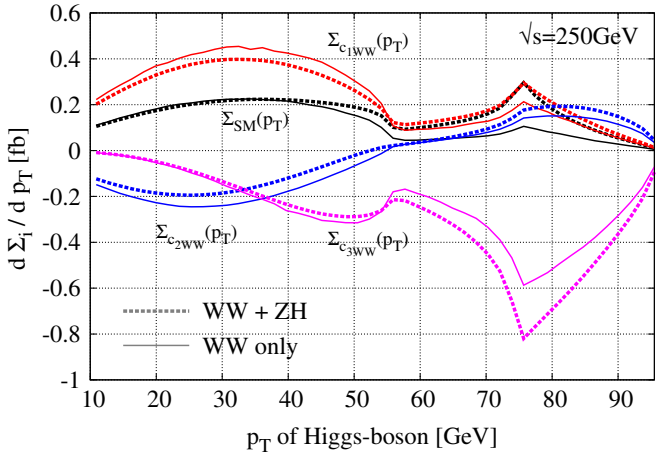

FIG. 7 (color online). p_T distribution of the weight function for the $\nu\bar{\nu}H$ process, where the differential distributions are integrated over y_H at $\sqrt{s} = 250$ GeV for $m_H = 120$ GeV. $\Sigma_{\rm SM}$ gives the SM distribution, and Σ_{c_i} shows the coefficients of the nonstandard HWW couplings $c_i \equiv c_{1WW}$, c_{2WW}, c_{3WW}. The thick dashed lines show the weight functions that include both the t- and s-channel contributions, while the thin lines are those with the t-channel contribution only. The thick dashed curve for the SM distribution, $\Sigma_{\rm SM}$, is the sum over all the neutrino species $(\nu_e, \nu_\mu, \nu_\tau)$.

ZH production amplitudes, we can constrain the HWW couplings by using the two-dimensional weight functions $\Sigma_i(y_H, p_{TH})$ of Eq. (55), including the interference contributions, where only the SM amplitudes in Eq. (52) are replaced by the sum of the WW fusion and the ZH production amplitudes. It should also be noted that the thick dashed SM curve in Fig. 7 includes the contributions from all the neutrino flavors, which cannot be distinguished from the signal. The limited phase space at low energies gives rise to the complex p_T dependence at 56 GeV and 75 GeV, which are the Higgs-boson momenta when $m_{\nu\bar{\nu}} = m_Z + 5\Gamma_Z$ and $m_{\nu\bar{\nu}} = m_Z - 5\Gamma_Z$, respectively. We find that there are large destructive interference effects for c_{1WW} and c_{2WW} at low p_{TH}. On the contrary the c_{2WW} and c_{3WW} curves show strong constructive interferences at high p_{TH}.

By using the two-dimensional weight functions, we find the eigenvectors and their 1σ errors at $\sqrt{s} = 250$ GeV with $L_0 = 100$ fb^{-1} and $P = \bar{P} = 0$ to be

$$.51c_{1WW} + .085c_{2WW} - .86c_{3WW} = \pm.017, \quad (66a)$$
$$.71c_{1WW} - .61c_{2WW} + .36c_{3WW} = \pm.030, \quad (66b)$$
$$.49c_{1WW} + .79c_{2WW} + .37c_{3WW} = \pm.51. \quad (66c)$$

Comparing the results of Eq. (66) with those of Eq. (64) from the t-channel contribution only, we find that the errors of the first two eigenvectors are almost the same despite the growth of the SM cross section. It is because the general growth of the magnitude of the SM distribution and the weight functions at $p_{TH} > 55$ GeV is compensated by the decrease in the weight functions at low p_{TH}. The third error decreases because it becomes more difficult to obtain a combination of the three weight functions that cancel out.

Similarly, we present the results for $\sqrt{s} = 350$ GeV with $L_0 = 100$ fb^{-1}, where we have included the s-channel ZH contribution.

$$.39c_{1WW} + .032c_{2WW} - .92c_{3WW} = \pm.0048, \quad (67a)$$
$$.66c_{1WW} - .71c_{2WW} + .25c_{3WW} = \pm.010, \quad (67b)$$
$$.64c_{1WW} + .71c_{2WW} + .29c_{3WW} = \pm.14. \quad (67c)$$

Comparing Eq. (67) with Eq. (65), the errors of the first two eigenvectors are reduced slightly, while the largest error is reduced by a factor 3. Again, it is a consequence of the complicated interference patterns for the three weight functions.

4. Sensitivity at $\sqrt{s} = 1$ TeV

Figure 3 shows that the WW fusion cross section grows with the c.m. energy, and reaches 210 fb at $\sqrt{s} = 1$ TeV. Precision studies of Higgs-boson properties, including the HWW couplings, will be one of the major motivations of the energy upgrade to ILC-II. We find the eigenvectors and their errors for $L_0 = 100$ fb^{-1} and $P = \bar{P} = 0$,

$$.14c_{1WW} + .038c_{2WW} - .990c_{3WW} = \pm.00\,079, \quad (68a)$$
$$.71c_{1WW} - .70c_{2WW} + .072c_{3WW} = \pm.0034, \quad (68b)$$
$$.69c_{1WW} + .71c_{2WW} + .12c_{3WW} = \pm.070. \quad (68c)$$

The errors are now a factor of 2 to 3 smaller than those at 500 GeV in Eq. (60). The reduction factor is bigger than the naive expectation from the cross section ratio $(77\text{ fb}/210\text{ fb})^{1/2} \sim 0.6$. This is because of the s dependence of the weight functions of c_{2WW} and c_{3WW}, in Eqs. (52b) and (52c), which grows linearly with s. On the other hand, the reduction is not so strong as we would expect from the linear growth of the weight functions. We find that the power of the weight functions that grow with s for c_{2WW} and c_{3WW} in Eqs. (52b) and (52c), respectively, is greatly reduced because of the nonobservability of the ν_e and $\bar{\nu}_e$ momenta, which results in the integration of the factor $\mathcal{G}(\theta_1, \theta_2, \phi)$ in Eq. (55) for the observable weight functions.

It is instructive to study, just as a reference, how well we could have measured the HWW couplings if ν_e and $\bar{\nu}_e$ momenta were measurable. We would then be able to use the dependence of the weight functions on the full 3-body phase-space, x_1 or x_2, $\cos\theta_1$, $\cos\theta_2$, $\phi_1 - \phi_2$ in the e^+e^- c.m. frame; see Appendix A for our phase-space parameterizations. By using the integral approximation of Eq. (56), we find at $\sqrt{s} = 1$ TeV,

$$.084c_{1WW} + .14c_{2WW} - .986c_{3WW} = \pm.00\,083, \quad (69a)$$
$$.099c_{1WW} - .986c_{2WW} - .013c_{3WW} = \pm.0017, \quad (69b)$$
$$.992c_{1WW} + .087c_{2WW} + .097c_{3WW} = \pm.0064. \quad (69c)$$

It is remarkable that no hierarchy among the three eigenvalues survives and that all the three couplings are measured accurately and rather independently, as is clear from the single coupling dominance of the three weight functions in Eq. (52). It is perhaps most remarkable here that the error of the most accurately measured combination of the three couplings in a realistic environment, 0.00 075 in Eq. (68a), is not much different from the corresponding one, 0.00 079 in Eq. (69a).

5. Beam polarization effects

All the above results are obtained for unpolarized e^+ and e^- beams, $P = \bar{P} = 0$. Since only left-handed e^- and right-handed $e^+(\sigma_1 = -\sigma_2 = -)$ contribute to the WW fusion process, the polarization dependence of our results for $e^+e^- \to \nu_e\bar{\nu}_e H$, can be obtained in a straightforward manner. If, for instance, an integrated luminosity of $L_{(P,\bar{P})}$ is devoted to experiments with e^- beam with polarization P and e^+ beam with polarization $\bar{P}$, then the total covariance matrix is simply

$$[V^{-1}_{(P,\bar{P})}]_{ij} = \frac{L_{(P,\bar{P})}}{L_0}(1 - P)(1 + \bar{P})[V^{-1}_{(0,0)}]_{ij}, \quad (70)$$

where $L_0 = 100$ fb^{-1} is the nominal integrated luminosity,

adopted throughout this report. It is clear from this expression that if we distribute the luminosity equally to all four combination of $e^{\pm}$ polarizations

$$L_{(|P|,|\bar{P}|)} = L_{(|P|,-|\bar{P}|)} = L_{(-|P|,|\bar{P}|)} = L_{(-|P|,-|\bar{P}|)} = \frac{L_{\rm total}}{4}, \tag{71}$$

then the total covariance matrix is identical to that of the unpolarized case. The same applies for our choice of Eq. (29). On the other hand, if we devote the entire luminosity with fixed polarization, such as

$$L_{(-|P|,|\bar{P}|)} = L_{\rm total}, \tag{72}$$

then the inverse of the covariance matrix will be larger by a factor of $(1+|P|)(1+|\bar{P}|)$, simply because of the large WW fusion cross section.

V. ZH PRODUCTION PROCESS

In ZH production via s-channel γ and Z exchange, we can study $HZ\gamma$ and HZZ vertices. Unlike the WW fusion process all the final states are observable when the Z boson decays into a pair of charged leptons or quark jets. The technique of optimal observables provides us with high discriminating power among the couplings.

A. Helicity amplitudes, backgrounds and event selection

The momentum and helicity assignment in ZH production followed by $Z \to f\bar{f}$ decay is

$$e^-\left(k_1, \frac{\sigma_1}{2}\right) + e^+\left(k_2, \frac{\sigma_2}{2}\right) \to Z(p_Z, \lambda) + H(p_H), \quad \to f\left(p_1, \frac{\lambda_1}{2}\right) + \bar{f}\left(p_2, \frac{\lambda_2}{2}\right). \tag{73}$$

We neglect the mass of $e^{\pm}$ and the outgoing fermions, and the fermionic chirality conservation tells $\sigma_1 = -\sigma_2 = \alpha$, and $\lambda_1 = -\lambda_2 = \beta$. Then the helicity amplitudes

$$M^{e^+e^-\to ZH\to f\bar{f}H}_{\alpha,\beta} = j^{\mu}_{1\alpha}[g^{\gamma ee}_{\alpha} D_{\gamma}(s)\Gamma^{HZ\gamma}_{\mu\nu} + g^{Zee}_{\alpha} D_Z(s)\Gamma^{HZZ}_{\mu\nu}] \times \frac{\sum_{\lambda} \epsilon^{\nu *}(p_Z,\lambda)\epsilon_{\rho}(p_Z,\lambda)}{p_Z^2 - m_Z^2 + i m_Z \Gamma_Z} g^{Zff}_{+\beta} j^{\rho}_{2\beta}, \tag{74}$$

where

$$j^{\mu}_{1\alpha} = \bar{v}(k_2, -\alpha/2)\gamma^{\mu} P_{\alpha} u(k_1, \alpha/2), \tag{75a}$$

$$j^{\nu}_{2\beta} = \bar{u}(p_1, \beta/2)\gamma^{\nu} P_{\beta} v(p_2, -\beta/2) \tag{75b}$$

are the e^+e^- annihilation current (75a) and the $Z \to f\bar{f}$ current (75b), respectively. Here, α and β denotes the sign of the e^- and f helicity, respectively, and P_{α} is the chirality projection operator $P_{\alpha} = (1+\alpha\gamma_5)/2$, sometimes referred to as $P_- = P_L$ and $P_+ = P_R$. The propagators and the couplings are denoted as

$$D_{\gamma}(s) = 1/s, \qquad D_Z(s) = 1/(s - m_Z^2 + i m_Z \Gamma_Z), \tag{76a}$$

$$g^{\gamma ff}_{\alpha} = eQ_f, \qquad g^{Zff}_{\alpha} = g_Z(T_3^{f\alpha} - Q_f s_W^2), \tag{76b}$$

where Q_f and $T_3^{f\alpha}$ are the electric charge and the weak isospin of the fermion f with chirality α.

In the vicinity of the Z boson resonance $m_{f\bar{f}} \sim m_Z$, we can factorize the amplitudes of Eq. (74) into the $e^+e^- \to ZH$ production part and the $Z \to f\bar{f}$ decay part, summed over the decaying Z boson helicities

$$M^{e^+e^-\to ZH\to f\bar{f}H}_{\alpha\beta} = \sum_{\lambda} T^{ZH}_{\alpha\lambda} D_Z(p_Z^2) T^{Z\to f\bar{f}}_{\lambda\beta}. \tag{77}$$

The production amplitudes $T^{ZH}_{\alpha\lambda}$ are obtained in the e^+e^- collision c.m. frame. Here, $\lambda \equiv (+, 0, -)$ is the helicity of the produced Z boson. By using the generic HZZ and $HZ\gamma$ vertices of Eqs. (14b) and (16a), respectively, and by using the e^+e^- annihilation currents of Eq. (B4) in Appendix B, we find for $p_Z^2 = m_Z^2$

$$T^{ZH}_{\alpha\lambda} = j^{\mu}_{1\alpha}[g^{\gamma ee}_{\alpha} D_{\gamma}(s)\Gamma^{HZ\gamma}_{\mu\nu} + g^{Zee}_{\alpha} D_Z(s)\Gamma^{HZZ}_{\mu\nu}]\epsilon^{\nu *}(p_Z, \lambda), \tag{78}$$

$$= \hat{M}^{\lambda}_{\alpha} d^1_{\alpha,\lambda}(\theta_Z), \tag{79}$$

where

$$\hat{M}^{\lambda=0}_{\alpha} = \sum_{V=\gamma,Z} g^{Vee}_{\alpha} g_Z \sqrt{2s} E_Z D_V(s)\left(h_1^{ZV} + h_2^{ZV}\frac{\sqrt{s}E_Z\beta_Z^2}{m_Z^2}\right), \tag{80a}$$

$$\hat{M}^{\lambda=\pm}_{\alpha} = \sum_{V=\gamma,Z} g^{Vee}_{\alpha} g_Z \sqrt{2s} m_Z D_V(s) h_1^{ZV}, \tag{80b}$$

with $\beta_Z = \sqrt{1 - m_Z^2/E_Z^2}$ and

$$h_1^{ZZ} = 1 + c_{1ZZ} + c_{3ZZ}\frac{s + m_Z^2}{m_Z^2} + (c_{2ZZ} - c_{3ZZ})\frac{s + m_Z^2 - m_H^2}{m_Z^2}, \tag{81a}$$

$$h_2^{ZZ} = -2(c_{2ZZ} - c_{3ZZ}), \tag{81b}$$

$$h_1^{Z\gamma} = 2c_{3Z\gamma}\frac{s}{m_Z^2} + (c_{2Z\gamma} - c_{3Z\gamma})\frac{s + m_Z^2 - m_H^2}{m_Z^2}, \tag{81c}$$

$$h_2^{Z\gamma} = -2(c_{2Z\gamma} - c_{3Z\gamma}). \tag{81d}$$

In Eq. (79), the d functions

$$d^1_{\alpha,\lambda=0}(\theta) = -\frac{\alpha\sin\theta}{\sqrt{2}}, \qquad d^1_{\alpha,\lambda=\pm}(\theta) = \frac{1 + \lambda\alpha\cos\theta}{2} \tag{82}$$

dictate the overlap of the initial (e^+e^-) and the final (ZH) state angular momentum states in the $J = 1$ channel, in

terms of the opening angle θ between the electron and the Z-boson momenta in the e^+e^- c.m. frame.

The Z boson decay amplitude is expressed in the $Z \to \bar{f}$ rest frame simply as

$$T^{Z\to f\bar{f}}_{\lambda\beta} = g^{Zff}_{\beta}\epsilon^{\rho}(p_Z, \lambda) j_{2\beta\rho} = g^{Zff}_{\beta} m_Z d^1_{\lambda,\beta}(\theta^*) e^{i\lambda\phi^*} \tag{83}$$

for $\lambda_1 = -\lambda_2 = \beta$ massless quarks and leptons, and again in the zero-width limit $p_Z^2 = m_Z^2$. Here, θ^* and ϕ^* are the polar and azimuthal angles of the fermion f in the decaying Z boson rest frame, where the polar axis is chosen along the Z boson momentum direction in the e^+e^- rest frame, and ϕ^* is measured from the $e^+e^- \to ZH$ scattering plane; see Appendix A.

From the above helicity amplitudes, we can calculate the weight functions Σ_{c_i}. The differential cross section, with the e^- polarization α, summed over the final state helicities β is

$$d\sigma^f_\alpha = \frac{1}{2s}\sum_\beta \left| \sum_\lambda T^{ZH}_{\alpha\lambda} D_Z(p_Z^2) T^{Z\to f\bar{f}}_{\lambda\beta} \right|^2 d\Phi_3, \tag{84a}$$

$$= \frac{1}{2s}\sum_\beta \left| \sum_\lambda T^{ZH}_{\alpha\lambda} T^{Z\to f\bar{f}}_{\lambda\beta} \right|^2 |D_Z(p_Z^2)|^2 d\Phi_3. \tag{84b}$$

We can simplify the phase-space $d\Phi_3$ in the small width limit as

$$|D_Z(p_Z^2)|^2 d\Phi_3 = |p_Z^2 - m_Z^2 + i m_Z\Gamma_Z|^{-2} \frac{dp_Z^2}{2\pi} \times d\Phi_2(Z \to f\bar{f}) d\Phi_2(ZH), \tag{85a}$$

$$\to \frac{\pi\delta(p_Z^2 - m_Z^2)}{m_Z\Gamma_Z}\frac{dp_Z^2}{2\pi} \times d\Phi_2(Z \to f\bar{f}) d\Phi_2(ZH), \tag{85b}$$

$$= \frac{1}{2m_Z\Gamma_Z} d\hat{\Phi}_3. \tag{85c}$$

Here, $d\hat{\Phi}_3$ is the reduced 3-body phase-space element

$$d\hat{\Phi}_3 \equiv d\Phi_2(Z \to f\bar{f})$$
$$d\Phi_2(ZH) = (8\pi)^{-3}\bar{\beta}\left(\frac{m_Z^2}{s}, \frac{m_H^2}{s}\right) d\cos\theta_Z d\cos\theta^* d\phi^*, \tag{86}$$

where $\bar{\beta}(a, b)$ is given by Eq. (A9a) in Appendix A.

The differential cross section is now expressed as

$$d\sigma^f_\alpha = \frac{1}{2s}\sum_{\lambda,\lambda'} T^{ZH}_{\alpha\lambda}(T^{ZH}_{\alpha\lambda'})^* \rho^f_{\lambda\lambda'} d\hat{\Phi}_3. \tag{87}$$

In this equation, we introduced the $Z \to f\bar{f}$ decay density matrix by summing over the helicities and colors of f and $\bar{f}$,

$$\rho^f_{\lambda\lambda'} = \frac{1}{2m_Z\Gamma_Z}\sum_{\text{color}}\sum_\beta T^{Z\to f\bar{f}}_{\lambda\beta}(T^{Z\to f\bar{f}}_{\lambda'\beta})^*, \tag{88}$$

which is normalized as

$$\int \rho^f_{\lambda\lambda'} d\Phi_2(Z \to f\bar{f}) = \frac{\Gamma(Z\to f\bar{f})}{8\pi\Gamma_Z}\delta_{\lambda\lambda'} = \frac{B_f}{8\pi}\delta_{\lambda\lambda'}. \tag{89}$$

By using Eqs. (B5)–(B7) in Appendix B for the $Z \to f\bar{f}$ currents and the Z boson polarization vectors, we obtain a compact expression for the Z boson decay density matrix

$$\rho^f_{\lambda\lambda'} = 12\pi B_f \left[\begin{pmatrix} \frac{1+\cos^2\theta^*}{2} & -\frac{\sin\theta^*\cos\theta^*}{\sqrt{2}} e^{i\phi^*} & \frac{\sin^2\theta^*}{2} e^{2i\phi^*} \\ -\frac{\sin\theta^*\cos\theta^*}{\sqrt{2}} e^{-i\phi^*} & \sin^2\theta^* & \frac{\sin\theta^*\cos\theta^*}{\sqrt{2}} e^{i\phi^*} \\ \frac{\sin^2\theta^*}{2} e^{-2i\phi^*} & \frac{\sin\theta^*\cos\theta^*}{\sqrt{2}} e^{-i\phi^*} & \frac{1+\cos^2\theta^*}{2} \end{pmatrix} + A_f \begin{pmatrix} -\cos\theta^* & \frac{\sin\theta^*}{\sqrt{2}} e^{i\phi^*} & 0 \\ \frac{\sin\theta^*}{\sqrt{2}} e^{-i\phi^*} & 0 & \frac{\sin\theta^*}{\sqrt{2}} e^{i\phi^*} \\ 0 & \frac{\sin\theta^*}{\sqrt{2}} e^{-i\phi^*} & \cos\theta^* \end{pmatrix} \right] \tag{90}$$

for $\lambda, \lambda' = -, 0, +$. Here, B_f is the $Z \to f\bar{f}$ decay branching fraction

$$B_f = \frac{\Gamma(Z\to f\bar{f})}{\Gamma_Z} = \frac{m_Z N_f}{16\pi\Gamma_Z}[(g_L^{Zff})^2 + (g_R^{Zff})^2], \tag{91}$$

with $N_f = 1$ for leptons and $N_f = 3$ for quarks, and

$$A_f = \frac{(g_L^{Zff})^2 - (g_R^{Zff})^2}{(g_L^{Zff})^2 + (g_R^{Zff})^2} \tag{92}$$

is the left-right asymmetry parameter of the Zff couplings. In the following analysis, we use the tree-level expression for the asymmetry parameter Eq. (92) for the charged lepton decays, whereas we replace the branching fraction Eq. (91) by the observed values [2] in simulating the number of events.

Let us now obtain the weight functions for polarized $e^\pm$ beams. The differential cross section for polarized e^+e^- beams is expressed as

$$d\sigma^f(P, \bar{P}) = \left[\Sigma^f_{\text{SM}}(P, \bar{P}; \hat{\Phi}_3) + \sum_{c_i} c_i \Sigma^f_{c_i}(P, \bar{P}; \hat{\Phi}_3)\right] d\hat{\Phi}_3, \tag{93}$$

where the weight functions are obtained by summing over the e^- helicity α,

$$\Sigma^f_{\rm SM}(P,\bar{P};\hat{\Phi}_3) = \frac{1}{2s}\sum_\alpha\left(\frac{1+\alpha P}{2}\right)\left(\frac{1-\alpha\bar{P}}{2}\right)\sum_{\lambda,\lambda'}(\hat{M}_{\rm SM})^\lambda_\alpha(\hat{M}_{\rm SM})^{\lambda'*}_\alpha d^1_{\alpha,\lambda}(\theta_Z)d^1_{\alpha,\lambda'}(\theta_Z)\rho^f_{\lambda\lambda'}, \tag{94a}$$

$$\Sigma^f_{c_i}(P,\bar{P};\hat{\Phi}_3) = \frac{1}{2s}\sum_\alpha\left(\frac{1+\alpha P}{2}\right)\left(\frac{1-\alpha\bar{P}}{2}\right)\sum_{\lambda,\lambda'}[\{(\hat{M}_{c_i})^\lambda_\alpha(\hat{M}^*_{\rm SM})^{\lambda'}_\alpha + (\hat{M}_{\rm SM})^\lambda_\alpha(\hat{M}^*_{c_i})^{\lambda'}_\alpha\}d^1_{\alpha,\lambda}(\theta_Z)d^1_{\alpha,\lambda'}(\theta_Z)\rho^f_{\lambda\lambda'}]. \tag{94b}$$

Here, the ZH production matrix elements, $(\hat{M}_{\rm SM})^\lambda_\alpha$ and $(\hat{M}_{c_i})^\lambda_\alpha \equiv (\hat{M}_{c_{iZV}})^\lambda_\alpha$, are obtained from Eqs. (80) and (81):

$$(\hat{M}_{\rm SM})^\lambda_\alpha = (\hat{M}_{c_{1ZZ}})^\lambda_\alpha = \frac{m_Z\sqrt{2s}}{s-m_Z^2}g_Z g^{Zee}_\alpha\gamma_\lambda, \tag{95a}$$

$$(\hat{M}_{c_{kZV}})^\lambda_\alpha = (\hat{M}_{\rm SM})^\lambda_\alpha R^\alpha_V(s)f^\lambda_{kV}(s) \qquad (k=2,3), \tag{95b}$$

with

$$\gamma_\pm = 1, \qquad \gamma_0 = \frac{E_Z}{m_Z}, \tag{96a}$$

$$R^\alpha_Z = 1, \qquad R^+_\gamma = -\cot\theta_W\left(\frac{s-m_Z^2}{s}\right), \qquad R^-_\gamma = \tan 2\theta_W\left(\frac{s-m_Z^2}{s}\right), \tag{96b}$$

$$f^\lambda_{2Z}(s) = \frac{s-m_H^2}{m_Z^2} + 1 - \delta_{\lambda 0}\frac{2\sqrt{s}}{m_Z}\frac{\gamma_0^2-1}{\gamma_0}, \qquad f^\lambda_{2\gamma}(s) = \frac{s-m_H^2}{m_Z^2} + 1 - \delta_{\lambda 0}\frac{2\sqrt{s}}{m_Z}\frac{\gamma_0^2-1}{\gamma_0}, \tag{96c}$$

$$f^\lambda_{3Z}(s) = \frac{m_H^2}{m_Z^2} + \delta_{\lambda 0}\frac{2\sqrt{s}}{m_Z}\frac{\gamma_0^2-1}{\gamma_0}, \qquad f^\lambda_{3\gamma}(s) = \frac{s+m_H^2}{m_Z^2} - 1 + \delta_{\lambda 0}\frac{2\sqrt{s}}{m_Z}\frac{\gamma_0^2-1}{\gamma_0}, \tag{96d}$$

where $\delta_{00} = \delta_{\gamma\gamma} = \delta_{ZZ} = 1$ and $\delta_{\pm 0} = \delta_{Z\gamma} = \delta_{\gamma Z} = 0$. The weight functions $\Sigma^f_{c_i}$ are now expressed as

$$\Sigma^f_{\rm SM}(P,\bar{P};\hat{\Phi}_3) = \sum_\alpha\left(\frac{1+\alpha P}{2}\right)\left(\frac{1-\alpha\bar{P}}{2}\right)\frac{g_Z^2(g^{Zee}_\alpha)^2m_Z^2}{(s-m_Z^2)^2}\sum_{\lambda,\lambda'}\gamma_\lambda\gamma_{\lambda'}d^1_{\alpha\lambda}(\theta_Z)d^1_{\alpha\lambda'}(\theta_Z)\rho^f_{\lambda\lambda'}, \tag{97a}$$

$$\Sigma^f_{c_{kZV}}(P,\bar{P};\hat{\Phi}_3) = \sum_\alpha\left(\frac{1+\alpha P}{2}\right)\left(\frac{1-\alpha\bar{P}}{2}\right)\frac{g_Z^2(g^{Zee}_\alpha)^2m_Z^2}{(s-m_Z^2)^2}\left[\sum_{\lambda,\lambda'}\gamma_\lambda\gamma_{\lambda'}R^\alpha_V\{f^\lambda_{kV}(s)+f^{\lambda'}_{kV}(s)\}d^1_{\alpha\lambda}(\theta_Z)d^1_{\alpha\lambda'}(\theta_Z)\,{\rm Re}(\rho^f_{\lambda\lambda'})\right] \tag{97b}$$

for $k=2,3$ and $V=Z,\gamma$. The weight function for c_{1ZZ} is simply twice the SM one, Eq. (97a). Since all our matrix elements are real, only the real parts of the density matrix elements $\rho^f_{\lambda\lambda'}$ in Eq. (90) contribute to the weight functions.

The weight functions depend both on the beam polarization and on the final fermion species. For brevity, we give expressions for covariance matrices for electron polarization P, with unpolarized positron ($\bar{P}=0$). For $f=e$, μ or τ, we can use the full phase-space information of $\hat{\theta}$, θ^* and ϕ^*, and accordingly the covariance matrix is obtained as

$$[(V^l_P)^{-1}]_{ij} = L_0\int\frac{\Sigma^l_{c_i}(P,0;\hat{\Phi}_3)\Sigma^l_{c_j}(P,0;\hat{\Phi}_3)}{\Sigma^l_{\rm SM}(P,0;\hat{\Phi}_3)}d\hat{\Phi}_3, \tag{98}$$

where $L_0 = 100\ {\rm fb}^{-1}$.

On the other hand, when the outgoing fermion is invisible, i.e., for $f=\nu_e$, ν_μ or ν_τ, we can observe only the $\cos\theta_H = -\cos\theta_Z$ distribution, and the covariance matrix is

$$[(V^\nu_P)^{-1}]_{ij} = B(H\to b\bar{b})L_0\int\frac{\int\Sigma^\nu_{c_i}(P,0;\hat{\Phi}_3)d\cos\theta^*d\phi^*\int\Sigma^\nu_{c_j}(P,0;\hat{\Phi}_3)d\cos\theta^*d\phi^*}{\int\Sigma^\nu_{\rm SM}(P,0;\hat{\Phi}_3)d\cos\theta^*d\phi^*}d\cos\theta_Z. \tag{99}$$

Here, again, we multiply the branching fraction $B(H\to b\bar{b}) = 0.9$ because the $H\to\tau\tau$ decay mode may not be useful in the analysis.

When the outgoing fermions are quarks, $f=u$, d c, s, b, we use only the half phase-space information for θ^* and ϕ^* because the q jet and $\bar{q}$ jet cannot be distinguished. We find

$$[(V_P^q)^{-1}]_{ij} = L_0 \int \frac{(\Sigma^q_{c_i}(P,0;\hat{\Phi}_3) + \Sigma^q_{c_i}(P,0;\tilde{\hat{\Phi}}_3))(\Sigma^q_{c_j}(P,0;\hat{\Phi}_3) + \Sigma^q_{c_j}(P,0;\tilde{\hat{\Phi}}_3))}{(\Sigma^q_{\rm SM}(P,0;\hat{\Phi}_3) + \Sigma^q_{\rm SM}(P,0;\tilde{\hat{\Phi}}_3))} \frac{1}{2} d\hat{\Phi}_3, \tag{100}$$

where $\tilde{\hat{\Phi}}_3$ is the phase space obtained by interchanging q jet and $\bar{q}$ jet; see Eq. (44). Finally, the electron beam polarization is taken into account as

$$V^{-1} = \sum_{P=\pm 0.8} \frac{L_P}{L_0} \sum_{f=l,\nu,q} (V_P^f)^{-1}, \tag{101}$$

where L_P is the integrated luminosity for each electron beam polarization.

We expect no significant background to this channel. But the WW fusion process $e^+e^- \to \nu_e\bar{\nu}_e H$ can mimic the HZ production when the Z decays into neutrinos. This background is avoided by demanding the missing mass to lie within 5 times the Z boson width, see Eq. (40). After the cut, we confirm numerically that our results are not affected by the interference effects in the $\nu_e\bar{\nu}_e H$ channel.

B. Sensitivity analysis of HZZ and $HZ\gamma$ coupling

We first note that the five CP conserving dimensionless effective couplings c_{1ZZ}, c_{2ZZ}, c_{3ZZ}, $c_{2Z\gamma}$, and $c_{3Z\gamma}$ coming from the dimension-six operators, contribute to the process only through the four form factors of Eq. (81). In particular, only two combinations of the three couplings c_{1ZZ}, c_{2ZZ}, and c_{3ZZ} appear in the form factors of the HZZ and $HZ\gamma$ vertices. Consequently, we cannot determine the couplings independently at a fixed collision energy.

In the following analysis, we show the eigenvectors for the four combinations of the effective couplings

$$c'_{2ZZ} = c_{2ZZ} + \frac{m_Z^2}{s+m_Z^2} c_{1ZZ},$$
$$c'_{3ZZ} = c_{3ZZ} + \frac{m_Z^2}{s+m_Z^2} c_{1ZZ}, \qquad c_{2Z\gamma}, \quad \text{and} \quad c_{3Z\gamma}, \tag{102}$$

which can be measured simultaneously at each energy. Note that the unmeasurable combination

$$c_{1ZZ} - (c_{2ZZ} + c_{3ZZ}) \frac{m_Z^2}{s+m_Z^2} \tag{103}$$

changes with the collision energy $\sqrt{s}$, and hence moderate constraint on the coupling c_{1ZZ}, which measures the strength of the standard HZZ coupling, can be obtained after combining experiments at different energies as discussed in Ref. [13].

The covariance matrices are expressed in terms of the eigenvectors and the errors. With unpolarized electron beam $|P| = 0$, we find for $\sqrt{s} = 250$ GeV and $L = 100$ fb^{-1},

$$.88c'_{2ZZ} + .41c'_{3ZZ} + .097c_{2Z\gamma} + .15c_{3Z\gamma} = \pm.00\,048, \tag{104a}$$
$$.45c'_{2ZZ} - .86c'_{3ZZ} - .026c_{2Z\gamma} - .24c_{3Z\gamma} = \pm.0042, \tag{104b}$$
$$.068c'_{2ZZ} + .28c'_{3ZZ} - .54c_{2Z\gamma} - .79c_{3Z\gamma} = \pm.0054, \tag{104c}$$
$$.046c'_{2ZZ} + .10c'_{3ZZ} + .83c_{2Z\gamma} - .54c_{3Z\gamma} = \pm.072. \tag{104d}$$

The smallness of the magnitudes of the coefficients of the $HZ\gamma$ couplings in the first two eigenvectors and that of the coefficients of the HZZ couplings in the latter eigenvectors reveals that the HZZ couplings and $HZ\gamma$ couplings are measured rather independently. Inspection of the first two eigenvectors in Eq. (104), which are most tightly constrained, tells that the couplings c'_{2ZZ} and c'_{3ZZ} can be measured much more accurately than the other two couplings $c_{2Z\gamma}$ and $c_{3Z\gamma}$, and also their sum in Eq. (104a) can be measured almost 1 order of magnitude better than their difference in Eq. (104b). The errors of the $HZ\gamma$ couplings, $c_{2Z\gamma}$ and $c_{3Z\gamma}$, which can be deciphered from the third and the fourth eigenvectors, are significantly larger; those of their sum in Eq. (104c) and their difference in Eq. (104d) are, respectively, more than 1 and 2 orders of magnitude larger than the smallest error in Eq. (104a). This can be attributed to the cancellation of the contributions from the $HZ\gamma$ couplings between the left-handed and right-handed electron contributions, where the interference term between the γ and Z exchange amplitudes change sign,

$$g_L^{\gamma ee} g_L^{Zee} + g_R^{\gamma ee} g_R^{Zee} = -e(g_L^{Zee} + g_R^{Zee}) = e g_Z (1/2 - 2\sin^2\theta_W) \ll e g_Z. \tag{105}$$

Expressing Eq. (104) in terms of the covariance matrix, we reproduce identical results given in Eq. (5.4) of Ref. [13], even though we do not take into account τ polarization and partial identification of both b and $\bar{b}$ jets. Small improvements of the covariance matrix due to these additional measurements can be hidden in the numerical uncertainty of the correlation matrix elements in the standard expression in terms of the errors and their correlations.

The constraint on the couplings become significantly stronger when we introduce the e^- beam polarization.

With $|P| = 80\%$, $L_{(P=0.8)} = L_{(P=-0.8)} = 50$ fb^{-1} at $\sqrt{s} = 250$ GeV, we find

$$.056c'_{2ZZ} + .027c'_{3ZZ} + .53c_{2Z\gamma} + .85c_{3Z\gamma} = \pm.00\,024, \tag{106a}$$

$$.90c'_{2ZZ} + .43c'_{3ZZ} - .032c_{2Z\gamma} - .053c_{3Z\gamma} = \pm.00\,049, \tag{106b}$$

$$-.094c'_{2ZZ} + .20c'_{3ZZ} - .83c_{2Z\gamma} + .51c_{3Z\gamma} = \pm.0034, \tag{106c}$$

$$.42c'_{2ZZ} - .88c'_{3ZZ} - .19c_{2Z\gamma} + .12c_{3Z\gamma} = \pm.0043. \tag{106d}$$

It is salient that the errors of the couplings c'_{2ZZ} and c'_{3ZZ}, that of their sum in Eq. (106b) and that of their difference (106d), do not improve at all by introducing the beam polarization, from the corresponding ones in Eqs. (104a) and (104b). On the other hand, the errors of the two eigenvectors with dominant $c_{2Z\gamma}$ and $c_{3Z\gamma}$ components are reduced by a factor of 20. This observation can be explained as follows:

(1) The c_{2ZZ} and c_{3ZZ} coupling contribution depends on the beam polarization exactly the same way as the SM. In particular, the weight functions for c_{2ZZ} and c_{3ZZ} in Eq. (97b) have the same polarization dependence as the SM contribution in Eq. (97a), essentially because $R_Z^\alpha = 1$ in Eq. (97b).

(2) When a photon propagates in the s channel, the $c_{2Z\gamma}$ and $c_{3Z\gamma}$ contributions to the amplitude do not change by the beam polarization, since the electromagnetic interactions are chirality blind. But the interference of the γ exchange and the SM Z boson exchange amplitude changes sign; see Eq. (105).

We present our results for $\sqrt{s} = 350$ GeV for $L = 100$ fb^{-1} and $|P| = 80\%$: [1]

$$.029c'_{2ZZ} + .030c'_{3ZZ} + .34c_{2Z\gamma} + .94c_{3Z\gamma} = \pm.00\,015, \tag{107a}$$

$$.71c'_{2ZZ} + .70c'_{3ZZ} - .013c_{2Z\gamma} - .040c_{3Z\gamma} = \pm.00\,040, \tag{107b}$$

$$.67c'_{2ZZ} - .68c'_{3ZZ} - .28c_{2Z\gamma} + .100c_{3Z\gamma} = \pm.0014, \tag{107c}$$

$$-.21c'_{2ZZ} + .21c'_{3ZZ} - .90c_{2Z\gamma} + .32c_{3Z\gamma} = \pm.0012. \tag{107d}$$

We first note that the eigenvectors and their ordering remain similar to those at $\sqrt{s} = 250$ GeV. We observe that c'_{3ZZ} is more accurately measured at high energies where the amplitude for the longitudinal Z boson ($\lambda = 0$) grows, mainly because of the $\gamma_0 = E_Z/m_Z$ factor in Eq. (95b). The weight functions for the couplings c'_{3ZZ} and $c_{3Z\gamma}$ grow as γ_0^2 from the dominant $\lambda = 0$ amplitudes; see Eq. (96d). In contrast, the weight functions for c'_{2ZZ} and $c_{2Z\gamma}$ do not increase at high energies, since the $\lambda = 0$ amplitude tends to be canceled by the $\lambda = \pm$ (transverse) modes; see Eq. (96c). This growth of the weight functions at high energies explains the general decrease of all the errors at $\sqrt{s} = 350$ GeV in Eq. (107) as compared with those at $\sqrt{s} = 250$ GeV in Eq. (106), despite the decrease of the total cross section from 260 fb to 130 fb.

At $\sqrt{s} = 500$ GeV for $L_0 = 100$ fb^{-1} with $P = \pm 0.8$, we find

$$.015c'_{2ZZ} + .035c'_{3ZZ} + .18c_{2Z\gamma} + .98c_{3Z\gamma} = \pm.000\,099, \tag{108a}$$

$$.38c'_{2ZZ} + .92c'_{3ZZ} - .0085c_{2Z\gamma} - .037c_{3Z\gamma} = \pm.00\,028, \tag{108b}$$

$$.24c'_{2ZZ} - .097c'_{3ZZ} + .95c_{2Z\gamma} - .17c_{3Z\gamma} = \pm.00\,086, \tag{108c}$$

$$.89c'_{2ZZ} - .37c'_{3ZZ} - .25c_{2Z\gamma} + .046c_{3Z\gamma} = \pm.0010. \tag{108d}$$

Despite smaller cross section at $\sqrt{s} = 500$ GeV, all the errors in Eq. (108) are smaller than those in Eq. (107) for $\sqrt{s} = 350$ GeV.

The energy dependence of the measurement at higher energies ($\sqrt{s} \gg m_Z$) can be read from Table I, where we show the high-energy limit of the matrix elements $(\hat{M}_{c_i})^\lambda_\alpha$ of Eq. (95). Since the weight functions are the interference between the SM amplitudes and the c_i amplitudes, we immediately find that c_{3ZZ} and $c_{3Z\gamma}$ are measured most accurately at high energies from the Z_L contribution, because their weight functions grow linearly with $\gamma_0 = E_Z/m_Z$. The couplings c_{2ZZ} and $c_{2Z\gamma}$ are best measured from the Z_T contribution, whose weight functions do not vanish at high energies.

Finally, we present the results for $\sqrt{s} = 1$ TeV for $L_0 = 100$ fb^{-1} with $P = \pm 0.8$;

TABLE I. The high energy limit of the matrix elements $(\hat{M}_{c_i})^\lambda_\alpha$ in Eq. (95). Here, $\gamma_0 = E_Z/m_Z$.

c_i	$Z_T(\lambda = \pm)$		$Z_L(\lambda = 0)$	
	Energy Dependence	Coefficient	Energy Dependence	Coefficient
SM	$1/\gamma_0$	$g_Z g_\alpha^{Zee}$	1	$g_Z g_\alpha^{Zee}$
c_{2ZZ}	γ_0	$4g_Z g_\alpha^{Zee}$	$1/\gamma_0$	$g_Z g_\alpha^{Zee}(5 - m_H^2/m_Z^2)$
c_{3ZZ}	$1/\gamma_0$	$g_Z g_\alpha^{Zee} m_H^2/m_Z^2$	γ_0	$4g_Z g_\alpha^{Zee}$
$c_{2Z\gamma}$	γ_0	$4e$	$1/\gamma_0$	$e(5 - m_H^2/m_Z^2)$
$c_{3Z\gamma}$	γ_0	$4e$	γ_0	$8e$

[1] From now on, we do not report our results for $|P| = 0$ in order to save space. Individual results with $|P| = 0$ will be available on request from the authors.

$$.004c'_{2ZZ} + .039c'_{3ZZ} + .047c_{2Z\gamma} + .998c_{3Z\gamma} = \pm.000046, \tag{109a}$$

$$.092c'_{2ZZ} + .995c'_{3ZZ} - .003c_{2Z\gamma} - .039c_{3Z\gamma} = \pm.00013, \tag{109b}$$

$$-.16c'_{2ZZ} + .014c'_{3ZZ} - .986c_{2Z\gamma} + .047c_{3Z\gamma} = \pm.00086, \tag{109c}$$

$$.98c'_{2ZZ} - .092c'_{3ZZ} - .16c_{2Z\gamma} + .007c_{3Z\gamma} = \pm.0012. \tag{109d}$$

All the four couplings are now measured rather independently, as we can observe from the single coupling dominance in all the four eigenvectors. The error of $c_{3Z\gamma}$ and c'_{3ZZ} becomes half of those at 500 GeV in Eq. (108), because their weight functions are proportional to γ_0. On the other hand, the errors of c'_{2ZZ} and $c_{2Z\gamma}$ do not improve because the weight functions remain constant at high energies.

VI. $e^+e^- \to e^+e^-H$ DOUBLE-TAG ZZ-FUSION PROCESSES

In this section, we study the HZZ, $HZ\gamma$ and $H\gamma\gamma$ couplings via the t-channel vector-boson fusion (VBF) process $e^+e^- \to e^+e^-H$; see Fig. 2(b). The merit of the t-channel VBF processes is that the cross section grows with $\sqrt{s}$, and also, we expect sensitivity to the coupling c_{1ZZ}, which cannot be measured independently from the other couplings in the s-channel process $e^+e^- \to ZH$.

A. Helicity amplitudes and background

The momentum and helicity assignments are the same as those in Eq. (45) for the W-boson fusion process

$$e^-\left(k_1, \frac{\sigma_1}{2}\right) + e^+\left(k_2, \frac{\sigma_2}{2}\right) \to e^-\left(p_1, \frac{\lambda_1}{2}\right) + e^+\left(p_2, \frac{\lambda_2}{2}\right) + H(p_H). \tag{110}$$

Here again we neglect the mass of $e^\pm$, and only two diagrams of Fig. 2(a) (ZH production) and Fig. 2(b) (VBF) contribute. The electron chirality conservation tells $\sigma_i = \lambda_i$ for the VBF amplitudes, and $\sigma_1 = -\sigma_2$ and $\lambda_1 = -\lambda_2$ for ZH production amplitudes. When $\sigma_1 = \lambda_1 = -\sigma_2 = -\lambda_2$, the two amplitudes interfere. The ZH production contribution is suppressed by requiring the invariant mass of the e^+e^- pair to be away from m_Z, Eq. (42).

The helicity amplitudes for the VBF process are given as

$$\begin{aligned} M^{\lambda_1\lambda_2}_{\sigma_1\sigma_2}(e^+e^- \to e^-e^+H) &= j^\mu_{e^-(\sigma_1,\lambda_1)}[g^{Zee}_{\sigma_1} D_Z(t_1)\Gamma^{ZZH}_{\mu\nu} D_Z(t_2) g^{Zee}_{-\sigma_2} \\ &+ g^{Zee}_{\sigma_1} D_Z(t_1)\Gamma^{Z\gamma H}_{\mu\nu} D_\gamma(t_2) g^{\gamma ee}_{-\sigma_2} \\ &+ g^{\gamma ee}_{\sigma_1} D_\gamma(t_1)\Gamma^{\gamma ZH}_{\mu\nu} D_Z(t_2) g^{Zee}_{-\sigma_2} \\ &+ g^{\gamma ee}_{\sigma_1} D_\gamma(t_1)\Gamma^{\gamma\gamma H}_{\mu\nu} D_\gamma(t_2) g^{\gamma ee}_{-\sigma_2}] j^\nu_{e^+(\sigma_2,\lambda_2)} \end{aligned} \tag{111}$$

for $\lambda_1 = \sigma_1$, and $\lambda_2 = \sigma_2$. The propagator factors $D_V(t_i)$ and the Vee couplings g^{Vee}_α are given in Eq. (76). The t-channel currents

$$j^\mu_{e^-(\alpha\alpha)} = \bar{u}(p_1, \alpha/2)\gamma^\mu P_\alpha u(k_1, \alpha/2), \tag{112a}$$

$$j^\nu_{e^+(\beta\beta)} = \bar{v}(k_2, \beta/2)\gamma^\nu P_{-\beta} v(p_2, \beta/2) \tag{112b}$$

are evaluated in the laboratory frame

$$j^\mu_{e^-(\alpha\alpha)} = \sqrt{sx_1}\left(\cos\frac{\theta_1}{2}, \sin\frac{\theta_1}{2} e^{i\alpha\phi_1}, -i\alpha \sin\frac{\theta_1}{2} e^{i\alpha\phi_1}, \cos\frac{\theta_1}{2}\right), \tag{113a}$$

$$j^\nu_{e^+(\beta\beta)} = \sqrt{sx_2}\left(\sin\frac{\theta_2}{2}, \cos\frac{\theta_2}{2} e^{-\beta i\phi_2}, i\beta\cos\frac{\theta_2}{2} e^{-i\beta\phi_2}, -\sin\frac{\theta_2}{2}\right) \tag{113b}$$

in the $m_e = 0$ limit, where the four momenta of the final electron and positron are parametrized as in Eq. (A1). The helicity amplitudes are then expressed as

$$\begin{aligned} M^{\alpha\beta}_{\alpha\beta} = g_Z m_Z \sum_{V_1=Z,\gamma} \sum_{V_2=Z,\gamma} g^{V_1ee}_\alpha D_{V_1}(t_1) D_{V_2}(t_2) g^{V_2ee}_{-\beta} \mathcal{F}(\theta_1, \theta_2) \\ \otimes \left[\delta_{\alpha\beta}\left(h^{V_1V_2}_1 \mathcal{H} + \frac{h^{V_1V_2}_2}{m_Z^2}\frac{s}{8}\mathcal{G}'\right) + \delta_{\alpha,-\beta}\left(h^{V_1V_2}_1 + \frac{h^{V_1V_2}_2}{m_Z^2}\frac{s}{8}\mathcal{G}\right)\right], \end{aligned} \tag{114}$$

where the functions $\mathcal{F}$, $\mathcal{H}$, $\mathcal{G}$, and $\mathcal{G}'$ are given in Eq. (B2) and (B3) of Appendix B. The above helicity amplitudes can be expressed as

$$M^{\alpha\beta}_{\alpha\beta} = (M_{\rm SM})^{\alpha\beta}_{\alpha\beta} + \sum_i c_i (M_{c_i})^{\alpha\beta}_{\alpha\beta}, \tag{115}$$

where

$$(M_{c_{1ZZ}})^{\alpha\beta}_{\alpha\beta} = (M_{\rm SM})^{\alpha\beta}_{\alpha\beta} = g_Z m_Z g^{Zee}_{\alpha} g^{Zee}_{-\beta} D_Z(t_1) D_Z(t_2) \mathcal{F}(\theta_1, \theta_2)(\delta_{\alpha\beta}\mathcal{H}(\theta_1, \theta_2, \phi) + \delta_{\alpha,-\beta}), \tag{116a}$$

$$(M_{c_{2V_1V_2}})^{\alpha\beta}_{\alpha\beta} = (M_{\rm SM})^{\alpha\beta}_{\alpha\beta} \frac{D_{V_1}(t_1)}{D_Z(t_1)} \frac{D_{V_2}(t_2)}{D_Z(t_2)} \left[f_{2V_1V_2} + \frac{s}{4m_Z^2} \frac{\delta_{\alpha\beta}\mathcal{G}' + \delta_{\alpha,-\beta}\mathcal{G}}{\delta_{\alpha\beta}\mathcal{H}(\theta_1, \theta_2, \phi) + \delta_{\alpha,-\beta}} \right], \tag{116b}$$

$$(M_{c_{3V_1V_2}})^{\alpha\beta}_{\alpha\beta} = (M_{\rm SM})^{\alpha\beta}_{\alpha\beta} \frac{D_{V_1}(t_1)}{D_Z(t_1)} \frac{D_{V_2}(t_2)}{D_Z(t_2)} \left[f_{3V_1V_2} - \frac{s}{4m_Z^2} \frac{\delta_{\alpha\beta}\mathcal{G}' + \delta_{\alpha,-\beta}\mathcal{G}}{\delta_{\alpha\beta}\mathcal{H}(\theta_1, \theta_2, \phi) + \delta_{\alpha,-\beta}} \right], \tag{116c}$$

with

$$f_{1ZZ} = 1, \qquad f_{2ZZ} = f_{2Z\gamma} = f_{2\gamma Z} = f_{2\gamma\gamma} = -\frac{m_H^2 - t_1 - t_2}{m_Z^2}, \tag{117a}$$

$$f_{3ZZ} = \frac{m_H^2}{m_Z^2}, \qquad f_{3Z\gamma} = \frac{m_H^2 - t_1 + t_2}{m_Z^2}, \qquad f_{3\gamma Z} = \frac{m_H^2 + t_1 - t_2}{m_Z^2}. \tag{117b}$$

It should be noted that in the notation of Eq. (115), the coefficients of the $HZ\gamma$ couplings should be interpreted as

$$c_{kZ\gamma}(M_{c_{kZ\gamma}})^{\alpha\beta}_{\alpha\beta} + c_{k\gamma Z}(M_{c_{k\gamma Z}})^{\alpha\beta}_{\alpha\beta} = c_{kZ\gamma}[(M_{c_{kZ\gamma}})^{\alpha\beta}_{\alpha\beta} + (M_{c_{k\gamma Z}})^{\alpha\beta}_{\alpha\beta}] \tag{118}$$

for $k = 2, 3$, by using the expressions in Eq. (116b) and (116c).

The SM distribution $\Sigma_{\rm SM}$ and the weight functions Σ_{c_i} depend on the 3-body phase space in the laboratory frame, which is parametrized as in Eq. (A8e),

$$d\Phi_3 = \frac{s}{1024\pi^4} \times \frac{x_1(1 - x_1 - m_H^2/s)}{[1 - x_1(1 - \cos\theta_{12})/2]^2} dx_1 d\cos\theta_1 d\cos\theta_2 d\phi, \tag{119}$$

where $\phi = \phi_2 - \phi_1$. The differential cross section with e^- and e^+ beam polarizations, P and $\bar{P}$, respectively, is expressed as in Eq. (20), where the weight functions are

$$\Sigma_{\rm SM}(P, \bar{P}; \Phi_3) = \frac{1}{2s} \sum_{\alpha,\beta} \left(\frac{1 + \alpha P}{2}\right)\left(\frac{1 + \beta\bar{P}}{2}\right) |(M_{\rm SM})^{\alpha\beta}_{\alpha\beta}|^2,$$

$$\Sigma_{c_i}(P, \bar{P}; \Phi_3) = \frac{1}{2s} \sum_{\alpha\beta} \left(\frac{1 + \alpha P}{2}\right)\left(\frac{1 + \beta\bar{P}}{2}\right) \times 2\,{\rm Re}[(M_{c_i})^{\alpha\beta}_{\alpha,\beta}(M^*_{\rm SM})^{\alpha\beta}_{\alpha\beta}]. \tag{120a}$$

The six nonstandard couplings, $c_i \equiv c_{1ZZ}, c_{2ZZ}, c_{3ZZ}, c_{2Z\gamma}, c_{3Z\gamma}$, and $c_{2\gamma\gamma}$, contribute to the t-channel Z and γ exchange processes, and the inverse of the covariant matrix is then evaluated as in Eq. (26b). As shown in Fig. 3 and noted in Sec. III C, the interference contribution from the s-channel ZH production amplitudes is not negligible at $\sqrt{s} = 250$ GeV and at 350 GeV. We therefore replace the SM amplitude in Eq. (120) by the sum of the t-channel and s-channel amplitudes at these energies. That is, we neglect contributions from the anomalies in the suppressed ZH production amplitudes.

B. Constraint on the HZZ, $HZ\gamma$, and $H\gamma\gamma$ couplings

1. Sensitivity at $\sqrt{s} = 250$ GeV and 350 GeV with the integration approximation

We first present the "theoretical" result for the contribution from the t-channel vector-boson fusion, using the standard integration procedure for $\sqrt{s} = 250$ and 350 GeV. Later on we take into consideration the interference effects from s-channel ZH production and adopt a more realistic approach to evaluate the inverse of the respective covariance matrices.

Our results for the purely t-channel process at $\sqrt{s} = 250$ GeV for $L_0 = 100$ fb^{-1} with $|P| = 80\%$ are

$$.001c_{1ZZ} - .000c_{2ZZ} - .001c_{3ZZ} - .001c_{2Z\gamma} + .99\,997c_{3Z\gamma} - .008c_{2\gamma\gamma} = \pm.0014, \tag{121a}$$

$$.028c_{1ZZ} - .067c_{2ZZ} + .005c_{3ZZ} - .065c_{2Z\gamma} - .008c_{3Z\gamma} - .995c_{2\gamma\gamma} = \pm.0040, \tag{121b}$$

$$.009c_{1ZZ} - .097c_{2ZZ} + .010c_{3ZZ} + .993c_{2Z\gamma} + .000c_{3Z\gamma} - .058c_{2\gamma\gamma} = \pm.0099, \tag{121c}$$

$$.28c_{1ZZ} + .54c_{2ZZ} - .79c_{3ZZ} + .056c_{2Z\gamma} - .002c_{3Z\gamma} - .036c_{2\gamma\gamma} = \pm.047, \tag{121d}$$

$$.73c_{1ZZ} - .65c_{2ZZ} - .19c_{3ZZ} - .064c_{2Z\gamma} - .000c_{3Z\gamma} + .068c_{2\gamma\gamma} = \pm.067, \tag{121e}$$

$$.62c_{1ZZ} + .52c_{2ZZ} + .58c_{3ZZ} + .039c_{2Z\gamma} + .000c_{3Z\gamma} - .017c_{2\gamma\gamma} = \pm.17. \tag{121f}$$

The cross section for the t-channel double-tag eeH process is only 0.83 fb as can be seen from the solid thin curve in Fig. 3. Imposing the exclusion cut $|m_{e^+e^-} - m_Z| > 5\Gamma_Z$, it reduces to 0.55 fb, or 55 events for 100 fb^{-1}. Nevertheless, we present

the above results in the integral approximation (the small bin size limit) over the 3-body phase space, as a reference to study the energy dependence. Binning effects for small statistics is reported in the next subsubsection.

It is remarkable that the two $HZ\gamma$ couplings and the $H\gamma\gamma$ coupling are rather uniquely constrained in the first three eigenvectors of Eq. (121) with small errors. This is a consequence of the combined effect of the strong e^- beam polarization dependence of the $Z-\gamma$ interference term (even though it is effective only for the γ-exchange between e^- and H) and also from the kinematic difference between the γ and Z propagator factors when $|t_1|$ or $|t_2|$ or both are significantly smaller than m_Z^2. In fact, we confirm the latter effects from the unpolarized beam ($P=0$) case, where the three couplings are still measured rather uniquely [24]; $c_{2\gamma\gamma}$ is now constrained most accurately with the error $\pm.0041$, $c_{3Z\gamma}$ has an error of $\pm.011$, while $c_{2Z\gamma}$ is poorly constrained. The three HZZ couplings are constrained rather weakly in the last three lines of Eq. (121).

Similarly, at $\sqrt{s}=350$ GeV for $L=100$ fb^{-1} with $|P|=80\%$, we find

$$.002c_{1ZZ}-.000c_{2ZZ}-.003c_{3ZZ}+.001c_{2Z\gamma}+.99\,998c_{3Z\gamma}-.006c_{2\gamma\gamma}=\pm.00\,085, \tag{122a}$$
$$.046c_{1ZZ}-.17c_{2ZZ}-.021c_{3ZZ}-.21c_{2Z\gamma}-.006c_{3Z\gamma}-.96c_{2\gamma\gamma}=\pm.0035, \tag{122b}$$
$$.025c_{1ZZ}-.099c_{2ZZ}+.006c_{3ZZ}+.98c_{2Z\gamma}-.003c_{3Z\gamma}-.19c_{2\gamma\gamma}=\pm.0053, \tag{122c}$$
$$.29c_{1ZZ}+.41c_{2ZZ}-.86c_{3ZZ}+.030c_{2Z\gamma}-.004c_{3Z\gamma}-.047c_{2\gamma\gamma}=\pm.016, \tag{122d}$$
$$.47c_{1ZZ}-.82c_{2ZZ}-.24c_{3ZZ}-.057c_{2Z\gamma}-.000c_{3Z\gamma}+.19c_{2\gamma\gamma}=\pm.025, \tag{122e}$$
$$.83c_{1ZZ}+.34c_{2ZZ}+.44c_{3ZZ}+.004c_{2Z\gamma}-.000c_{3Z\gamma}-.032c_{2\gamma\gamma}=\pm.054. \tag{122f}$$

Here, the cross section is 2.9 fb which is almost a factor 3.5 times larger than those at 250 GeV; see Fig. 3. The effect of the exclusion cut is negligible and the cross section is reduced to 2.8 fb, which would mean 280 events with 100 fb^{-1}. Therefore, we naively expect a factor of 2 improvements in the statistical error when compared with the results in Eq. (121). The results in Eq. (122) show that the error of the HZZ couplings decreases to about $1/3$, those of the $HZ\gamma$ couplings to $\sim 1/2$, while the $H\gamma\gamma$ coupling does not show a significant improvement. The $H\gamma\gamma$ coupling measurement does not improve because the amplitudes with $|t_i| < m_Z^2$ do not increase much with $\sqrt{s}$. We notice that the two couplings $c_{2\gamma\gamma}$ and $c_{2Z\gamma}$ now have some correlation, as can be seen from the combinations $(0.21c_{2Z\gamma}+0.96c_{2\gamma\gamma})$ in Eq. (122b) and $(0.98c_{2Z\gamma}-0.19c_{2\gamma\gamma})$ in Eq. (122c). It is because of their similar behavior when both $|t_1|$ and $|t_2|$ are larger than m_Z. Such a region of the phase space is tiny at $\sqrt{s}=250$ GeV, but starts appearing at 350 GeV, and will be dominating at higher energies.

2. *Sensitivity at $\sqrt{s}=250$ GeV and 350 GeV with the table method including s-channel contributions*

As the t-channel cross sections are very small at $\sqrt{s}=250$ GeV and 350 GeV, the interference effects due to the contribution from ZH amplitudes along with the exclusion $|m_{e^+e^-}-m_Z|>5\Gamma_Z$ can be significant as can be seen from the thick dashed line, in Fig. 3. To simulate the realistic experimental situation we adopt the table method to calculate V^{-1}, which is more realistic when the expected number of events is not large. Here, we examine the two-dimensional weight functions in terms of the momentum transfers $|t_1|$ and $|t_2|$.

At $\sqrt{s}=250$ GeV with $L_0=100$ fb^{-1} and $|P|=80\%$, the cross section of the double-tag e^+e^-H process becomes 0.93 fb, after including the contribution from the s-channel amplitudes; see Fig. 3. Because of the smallness of the signal events (93 events for 100 fb^{-1} with 100% efficiency), we integrate the weight functions over the azimuthal angle and $m_{e^+e^-}$, and divide $|t_i|$'s into 3 regions, each as follows: $|t_i|<(45\ \text{GeV})^2$, $(45\ \text{GeV})^2<|t_i|<(90\ \text{GeV})^2$, and $|t_i|>(90\ \text{GeV})^2$. With this binning, all the 18 bins (9 bins each for $P=0.8$ and $P=-0.8$) have approximately 5 events. We obtain the V^{-1} matrix by summing over the contributions from 18 bins, and find

$$.006c_{1ZZ}-.0c_{2ZZ}-.010c_{3ZZ}+.31c_{2Z\gamma}+.95c_{3Z\gamma}+.051c_{2\gamma\gamma}=\pm.0043, \tag{123a}$$
$$.050c_{1ZZ}+.13c_{2ZZ}+.10c_{3ZZ}+.93c_{2Z\gamma}-.31c_{3Z\gamma}+.065c_{2\gamma\gamma}=\pm.013, \tag{123b}$$
$$.24c_{1ZZ}+.63c_{2ZZ}+.60c_{3ZZ}-.11c_{2Z\gamma}+.064c_{3Z\gamma}-.41c_{2\gamma\gamma}=\pm.016, \tag{123c}$$
$$.26c_{1ZZ}+.29c_{2ZZ}+.18c_{3ZZ}-.14c_{2Z\gamma}-.004c_{3Z\gamma}+.89c_{2\gamma\gamma}=\pm.043, \tag{123d}$$
$$.80c_{1ZZ}+.13c_{2ZZ}-.56c_{3ZZ}+.010c_{2Z\gamma}-.005c_{3Z\gamma}-.16c_{2\gamma\gamma}=\pm.088, \tag{123e}$$
$$.48c_{1ZZ}-.70c_{2ZZ}+.53c_{3ZZ}+.012c_{2Z\gamma}-.001c_{3Z\gamma}-.015c_{2\gamma\gamma}=\pm.37. \tag{123f}$$

In spite of the increase of the cross section, from 0.55 fb to 0.93 fb, we observe that the errors of all the eigenvectors in Eq. (123) are larger than those in Eq. (121), which are obtained by using the integral approximation. Especially, the error of the eigenvector with dominant $c_{2\gamma\gamma}$ component in Eq. (123d) becomes an order of magnitude larger than the corresponding one in Eq. (121b). The main reason for the enhancement of the errors is the loss of information due to the large bin size. For instance, the error of $c_{2\gamma\gamma}$ is reduced significantly if we divide the $|t_i| < (45\ \mathrm{GeV})^2$ bin into 2 bins, while that of $c_{3Z\gamma}$ is reduced if we divide the $|t_i| > (90\ \mathrm{GeV})^2$ bin into 2 bins. In the very high luminosity limit, we can decrease the bin size, and the integral limit of Eq. (121), corrected for the interference effects, is obtained. In the following analysis, however, we will use the result of Eq. (123) as the contribution from the double-tag eeH events at $\sqrt{s} = 250$ GeV for 100 fb^{-1} with $|P| = 0.8$.

We repeat the same exercise at $\sqrt{s} = 350$ GeV for $L_0 = 100$ fb^{-1} with $|P| = 0.8$. As can be seen from Fig. 3, the cross section increases to 3.3 fb from 2.9 fb due to constructive interference. Here, we considered 6 bins each for $|t_1|$ and $|t_2|$, to make the number of event almost the same in all the 72 bins. We find that

$$.004c_{1ZZ} + .005c_{2ZZ} - .002c_{3ZZ} + .11c_{2Z\gamma} + .99c_{3Z\gamma} + .014c_{2\gamma\gamma} = \pm.0012, \quad (124a)$$
$$.007c_{1ZZ} + .006c_{2ZZ} - .072c_{3ZZ} + .97c_{2Z\gamma} - .11c_{3Z\gamma} + .22c_{2\gamma\gamma} = \pm.0074, \quad (124b)$$
$$.21c_{1ZZ} + .31c_{2ZZ} + .44c_{3ZZ} + .21c_{2Z\gamma} - .013c_{3Z\gamma} - .79c_{2\gamma\gamma} = \pm.011, \quad (124c)$$
$$.67c_{1ZZ} + .20c_{2ZZ} - .70c_{3ZZ} - .026c_{2Z\gamma} - .000c_{3Z\gamma} - .14c_{2\gamma\gamma} = \pm.023, \quad (124d)$$
$$.71c_{1ZZ} - .31c_{2ZZ} + .52c_{3ZZ} - .046c_{2Z\gamma} - .000c_{3Z\gamma} + .35c_{2\gamma\gamma} = \pm.079, \quad (124e)$$
$$.023c_{1ZZ} + .88c_{2ZZ} + .19c_{3ZZ} - .092c_{2Z\gamma} - .000c_{3Z\gamma} + .43c_{2\gamma\gamma} = \pm.095. \quad (124f)$$

All the errors in Eq. (124) are approximately a factor of 2 larger than the corresponding ones in Eq. (122), mainly because of the loss of information due to the binning and also to the reduction of the dimensionality of the weight functions from 4 (x_i, $\cos\theta_1$, $\cos\theta_2$, ϕ) to 2 ($|t_1|$, $|t_2|$).

3. Sensitivity at $\sqrt{s} = 500$ GeV and 1 TeV

At $\sqrt{s} = 500$ GeV with $L = 100$ fb^{-1} with $|P| = 80\%$, we find

$$.002c_{1ZZ} + .000c_{2ZZ} - .007c_{3ZZ} - .004c_{2Z\gamma} + .99\,995c_{3Z\gamma} - .005c_{2\gamma\gamma} = \pm.00\,057, \quad (125a)$$
$$.034c_{1ZZ} - .20c_{2ZZ} - .064c_{3ZZ} - .61c_{2Z\gamma} - .007c_{3Z\gamma} - .76c_{2\gamma\gamma} = \pm.0029, \quad (125b)$$
$$.044c_{1ZZ} - .28c_{2ZZ} - .030c_{3ZZ} + .78c_{2Z\gamma} + .000c_{3Z\gamma} - .55c_{2\gamma\gamma} = \pm.0035, \quad (125c)$$
$$.19c_{1ZZ} + .31c_{2ZZ} - .93c_{3ZZ} + .045c_{2Z\gamma} - .007c_{3Z\gamma} - .029c_{2\gamma\gamma} = \pm.0067, \quad (125d)$$
$$.34c_{1ZZ} - .84c_{2ZZ} - .23c_{3ZZ} - .098c_{2Z\gamma} - .000c_{3Z\gamma} + .33c_{2\gamma\gamma} = \pm.013, \quad (125e)$$
$$.92c_{1ZZ} + .27c_{2ZZ} + .28c_{3ZZ} + .012c_{2Z\gamma} - .000c_{3Z\gamma} - .063c_{2\gamma\gamma} = \pm.031. \quad (125f)$$

The cross section now is 6.6 fb, or 660 events with 100 fb^{-1}; see Fig. 3. We therefore expect that the statistical errors should be about 2/3 of those at $\sqrt{s} = 350$ GeV. In fact, all the errors of Eq. (125) are smaller than the corresponding errors in Eq. (122) by a factor of 1.2 to 2.4. At this energy, as mentioned above, kinematic difference in the Z and γ propagators diminishes, and the $H\gamma\gamma$ coupling $c_{2\gamma\gamma}$ tends to mix with $c_{2Z\gamma}$ and the HZZ couplings.

And at $\sqrt{s} = 1$ TeV for $L = 100$ fb^{-1} with $|P| = 80\%$, we find that

$$.002c_{1ZZ} + .002c_{2ZZ} - .020c_{3ZZ} - .019c_{2Z\gamma} + .9996c_{3Z\gamma} - .006c_{2\gamma\gamma} = \pm.0004, \quad (126a)$$
$$.008c_{1ZZ} + .033c_{2ZZ} - .15c_{3ZZ} - .95c_{2Z\gamma} - .022c_{3Z\gamma} - .26c_{2\gamma\gamma} = \pm.0018, \quad (126b)$$
$$.089c_{1ZZ} + .12c_{2ZZ} - .97c_{3ZZ} + .19c_{2Z\gamma} - .017c_{3Z\gamma} - .091c_{2\gamma\gamma} = \pm.0022, \quad (126c)$$
$$.035c_{1ZZ} - .67c_{2ZZ} + .018c_{3ZZ} + .17c_{2Z\gamma} + .000c_{3Z\gamma} - .72c_{2\gamma\gamma} = \pm.0025, \quad (126d)$$
$$.15c_{1ZZ} - .72c_{2ZZ} - .17c_{3ZZ} - .17c_{2Z\gamma} - .002c_{3Z\gamma} + .64c_{2\gamma\gamma} = \pm.0058, \quad (126e)$$
$$.98c_{1ZZ} + .12c_{2ZZ} + .11c_{3ZZ} + .011c_{2Z\gamma} + .000c_{3Z\gamma} - .063c_{2\gamma\gamma} = \pm.019. \quad (126f)$$

The cross section is around 13 fb, or 1300 events with 100 fb^{-1}. The error of $c_{3Z\gamma}$ in Eq. (126a) decreases by a factor 1.4 from the corresponding one in Eq. (125a) for 500 GeV. The other errors are reduced more significantly. At high energies, the distinction among the weight functions becomes clear and $c_{3Z\gamma}$, $c_{2Z\gamma}$, c_{3ZZ} and c_{1ZZ} are measured rather independently, while only c_{2ZZ} and $c_{2\gamma\gamma}$ are correlated. Since the γ and Z propagator factors are similar at high energies, the distinction come from the extra (t_1, t_2) dependence in Eq. (117) and from the azimuthal angle dependence in the factor $\mathcal{G}$ and $\mathcal{G}'$; see Eq. (B3) in Appendix B. The most significant improvement is found for the error of the eigenvector with dominant c_{3ZZ} component, which decreases by a factor of 3 from 0.0067 at $\sqrt{s} = 500$ GeV in Eq. (125d) to 0.0022 at $\sqrt{s} = 1$ TeV in Eq. (126c).

Overall, we find that the $HZ\gamma$ couplings are most accurately measured at high energies in the double-tag eeH process. However, the accuracies of the $c_{2Z\gamma}$ and $c_{3Z\gamma}$ measurements cannot compete with those from the ZH process, as can be seen, e.g., by comparing Eqs. (126a) and (126b) with Eqs. (109a) and (109c), respectively, at $\sqrt{s} = 1$ TeV. The double-tag events are found to be most important in distinguishing c_{1ZZ}, the SM-like HZZ coupling, from c_{2ZZ} and c_{3ZZ}.

VII. NO-TAG $ee \to (ee)H$ PROCESS

Although the double-tag t-channel eeH process shows certain sensitivity to the $H\gamma\gamma$ coupling $c_{2\gamma\gamma}$, the sensitivity at $\sqrt{s} = 500$ GeV and 1 TeV with $L_0 = 100$ fb^{-1} is not sufficient for resolving the $H\gamma\gamma$ coupling of the SM from the W-boson and top-quark loops. We can expect better sensitivity to the $H\gamma\gamma$ coupling when the $e^\pm$ are not tagged, because of the fusion of almost real photons. The produced Higgs-boson has little p_T, and can be distinguished from the $\nu_e\bar{\nu}_e H$ events.

A. Cross section

The momentum and helicity assignment for the initial and final particles in no-tag $(ee)H$ process is the same as the double-tag eeH process, Eq. (110). The momentum and helicity of the intermediate almost real photon is assigned as

$$e^-\left(k_1, \frac{\sigma_1}{2}\right) \to e^-\left(p_1, \frac{\lambda_1}{2}\right) + \gamma(k_1', \lambda_1'), \tag{127a}$$

$$e^+\left(k_2, \frac{\sigma_2}{2}\right) \to e^+\left(p_2, \frac{\lambda_2}{2}\right) + \gamma(k_2', \lambda_2'), \tag{127b}$$

where λ_1' and λ_2' is the helicity of the equivalent real photon emitted from e^- and e^+, respectively. The final electron and positron escape detection by going into the beam pipe, and an almost real photon of the virtuality $|q^2| \ll m_H^2$ is emitted in the same direction; see e.g. Ref. [25] for a review. The Z boson contribution is suppressed by a small factor of $|q^2|/m_Z^2 \ll 1$. The minimum and maximum magnitude of the square of the electron or positron momentum transfer is calculated as

$$q^2_{\min} = \frac{m_e^2 z^2}{1-z}, \qquad q^2_{\max} = (1-z)\frac{s}{2}(1-\cos\theta_{\min}), \tag{128}$$

where $z = 2E_\gamma/\sqrt{s}$ is the energy fraction of the photon, and $\theta_{\min}$ is the polar angle below which the final $e^\pm$ escapes detection into the beam pipe. In our analysis, we set $\cos\theta_{\min} = 0.995$; see Eq. (33). The equivalent real photon distribution can be split into two parts,

$$D_{\gamma/e^\pm}(z, Q^2) = D^{\sigma_i\lambda_j'=+}_{\gamma/e^\pm}(z, Q^2) + D^{\sigma_i\lambda_j'=-}_{\gamma/e^\pm}(z, Q^2), \tag{129}$$

where the helicity preserving component ($\sigma\lambda' = +$) and the helicity flip component ($\sigma\lambda' = -$) are [26]

$$D^+_{\gamma/e^\pm}(z, Q^2) = \frac{\alpha}{2\pi}\left[\frac{1}{z}\left(\ln\frac{Q^2}{q^2_{\min}} - 1\right) + z\right], \tag{130a}$$

$$D^-_{\gamma/e^\pm}(z, Q^2) = \frac{\alpha}{2\pi}\left[\frac{(1-z)^2}{z}\left(\ln\frac{Q^2}{q^2_{\min}} - 1\right)\right], \tag{130b}$$

respectively, with

$$Q^2 = \min\{m_H^2, q^2_{\max}\}. \tag{131}$$

It is worth noting that the last term z in the parenthesis of the helicity preserving ($\sigma\lambda' = +$) distribution (130a) comes from the helicity flip ($\sigma\lambda = -$) amplitude where the final $e^\pm$ helicity is opposite from the initial one. Since contribution from the momentum transfer much smaller than 1 GeV^2 dominates the photon distribution, we use $\alpha = 1/137$ in Eq. (130). The real photon approximation for the matrix elements cease to be valid when $Q^2 = |t_i|$ becomes $\mathcal{O}(m_H^2)$. In our study, the maximum momentum transfer $q^2_{\max}$ stays below $\sim 0.25 m_H^2$ even at $\sqrt{s} = 1$ TeV, and hence our predictions do not change significantly when we replace the scale from m_H^2 by $0.1 m_H^2$, in Eq. (131).

The cross section for the no-tag $(ee)H$ events is now expressed as

$$\sigma^{(ee)H} = \sum_{\alpha,\beta}\left(\frac{1+\alpha P}{2}\right)\left(\frac{1+\beta\bar{P}}{2}\right)\sum_{\lambda_1',\lambda_2'}\int_0^1 dx_1 \int_0^1 dx_2 \times D^{\alpha\lambda_1'}_{\gamma/e^-}(x_1, Q^2) D^{\beta\lambda_2'}_{\gamma/e^+}(x_2, Q^2)\hat{\sigma}^{\gamma\gamma\to H}_{\lambda_1'\lambda_2'}, \tag{132}$$

where

$$\hat{\sigma}^{\gamma\gamma\to H}_{\lambda_1'\lambda_2'}(\hat{s}) = \delta_{\lambda_1'\lambda_2'}(16\pi^2)\frac{\Gamma_{\gamma\gamma}}{m_H}\delta(\hat{s} - m_H^2). \tag{133}$$

Here, x_i and λ_i' are the energy fractions and the helicities of the equivalent real photon in $e^-(i=1)$ and $e^+(i=2)$, respectively, $\alpha/2$ and $\beta/2$ are the e^- and e^+ helicities, and $\hat{s} = x_1 x_2 s$ is the square of the $\gamma\gamma$ collision energy. Higgs boson is produced only when $\lambda_1' = \lambda_2'$. Therefore,

the total cross section and the rapidity $y_H = 1/2 \log(x_1/x_2)$ distribution of the Higgs boson, which has strong dependence on the helicity profile of the equivalent real photon distribution, depends on the $e^{\pm}$ beam polarizations P and $\bar{P}$. We find, however, that the polarization effects survive only when both e^- and e^+ have nonzero polarization.

The unpolarized cross section of the no-tag $(ee)H$ events in Fig. 3 for $m_H = 120$ GeV and those of Fig. 4 for $m_H = 100$ GeV to 200 GeV are calculated by using the above formula with

$$\Gamma_{\gamma\gamma} = \frac{\alpha^2 m_H^3}{256\pi^3 v^2}|I|^2, \tag{134}$$

where the loop function I sums over the contributions from the W boson and the top quark [27]. The enhancement due to the W-boson pair production threshold can be observed in Fig. 4. For $m_H = 120$ GeV, the decay width of Eq. (134) gives $\Gamma_{\gamma\gamma}^{\rm SM} = 0.0073$ MeV, and the cross section is 0.15 fb, 0.32 fb, 0.56 fb, and 1.3 fb at $\sqrt{s} = 250$, 350, 500, and 1000 GeV, respectively, as shown in Fig. 3. When the integrated luminosity is 100 fb^{-1}, the expected number of events are 15, 32, 56, and 128, respectively. Therefore, in this study, we consider the no-tag events only at $\sqrt{s} = 500$ GeV and 1 TeV.

B. Error estimation for $c_{2\gamma\gamma}$

The interaction Lagrangian for the effective $H\gamma\gamma$ vertex

$$L_{\rm int}^{H\gamma\gamma} = \frac{1}{v} c_{2\gamma\gamma} H A_{\mu\nu} A^{\mu\nu} \tag{135}$$

contains both the SM loop contribution and new physics effects. We parametrize them as

$$c_{2\gamma\gamma} = c_{2\gamma\gamma}^{\rm SM} + \Delta c_{2\gamma\gamma}. \tag{136}$$

The SM contribution is approximated by the loop function I, and its numerical value for $m_H = 120$ GeV is

$$c_{2\gamma\gamma}^{\rm SM} = \frac{\alpha}{8\pi} I = -0.00\,187, \tag{137}$$

with a negligibly small imaginary part from the b and τ contributions. Our approximation of the pointlike coupling in the effective Lagrangian Eq. (135) is valid as long as $|q^2| \ll m_W^2,\ m_t^2$. The cross section of the no-tag $(ee)H$ process for $m_H = 120$ GeV is expressed in terms of the generalized $H\gamma\gamma$ coupling given in Eqs. (135) and (136) as

$$\sigma^{ee\to(ee)H}(\sqrt{s} = 500\ \text{GeV}) = 1.61 \times 10^5 (c_{2\gamma\gamma}^{\rm SM} + \Delta c_{2\gamma\gamma})^2\ \text{fb}, \tag{138a}$$

$$\sigma^{ee\to(ee)H}(\sqrt{s} = 1\ \text{TeV}) = 3.70 \times 10^5 (c_{2\gamma\gamma}^{\rm SM} + \Delta c_{2\gamma\gamma})^2\ \text{fb}. \tag{138b}$$

As mentioned earlier, this cross section does not depend on the e^- polarization P, as long as the e^+ polarization is zero, $\bar{P} = 0$.

While evaluating the error of the cross section, we take into account of the contribution from WW-fusion $\nu_e\bar{\nu}_e H$ events, which cannot be distinguished from the no-tag $(ee)H$ events when the Higgs boson has small transverse momentum. In the following analysis, we make a very naive estimate for the background and the errors by assuming that the Higgs-boson $p_{\rm T}$ can be resolved at 3 GeV accuracy and that the SM background contribution can be estimated from the high $p_{\rm T}$ distribution. In Fig. 8, we show the expected $p_{\rm T}$ distribution of the Higgs boson from the no-tag $(ee)H$ process as the red-solid rectangle, which is overlaid above the WW-fusion contribution shown by the gray-shaded histograms; Fig. 8(a) is for $\sqrt{s} = 500$ GeV and Fig. 8(b) is for $\sqrt{s} = 1$ TeV. Also shown in the figures are the statistical errors corresponding to the background WW-fusion events, and that of the sum of the no-tag $(ee)H$ and WW-fusion events for the lowest $p_{\rm T}$ ($p_{\rm T} < 3$ GeV) bin with $L_0 = 500$ fb^{-1}. We can then estimate the error of the signal $(ee)H$ cross section as follows:

$$\sigma_{\rm sig} = \sigma_{\rm tot} - \sigma_{\rm BG} = \bar{\sigma}_{\rm tot} - \bar{\sigma}_{\rm BG} \pm \sqrt{\frac{\bar{\sigma}_{\rm tot}^2}{N_{\rm tot}} + \frac{\bar{\sigma}_{\rm BG}^2}{N_{\rm BG}}}$$

$$= \bar{\sigma}_{\rm sig} \pm \sqrt{\frac{\bar{\sigma}_{\rm tot} + \bar{\sigma}_{\rm BG}}{L}}, \tag{139}$$

where $\bar{\sigma}$ represents the mean value and L is the integrated luminosity. The errors of the total and the background cross sections in the lowest $p_{\rm T}$ bin are estimated to be 0.023 fb and 0.012 fb, respectively, at $\sqrt{s} = 500$ GeV, and 0.033 fb and 0.016 fb, respectively, at $\sqrt{s} = 1$ TeV. By taking the squared sum of the errors, we obtain the following estimates:

$$\sigma_{\rm sig} = 0.56 \pm 0.045\ \text{fb} \quad \text{at } \sqrt{s} = 500\ \text{GeV}; L = 500\ \text{fb}^{-1}, \tag{140a}$$

$$\sigma_{\rm sig} = 1.29 \pm 0.064\ \text{fb} \quad \text{at } \sqrt{s} = 1\ \text{TeV}; L = 500\ \text{fb}^{-1}. \tag{140b}$$

We then find from Eq. (138)

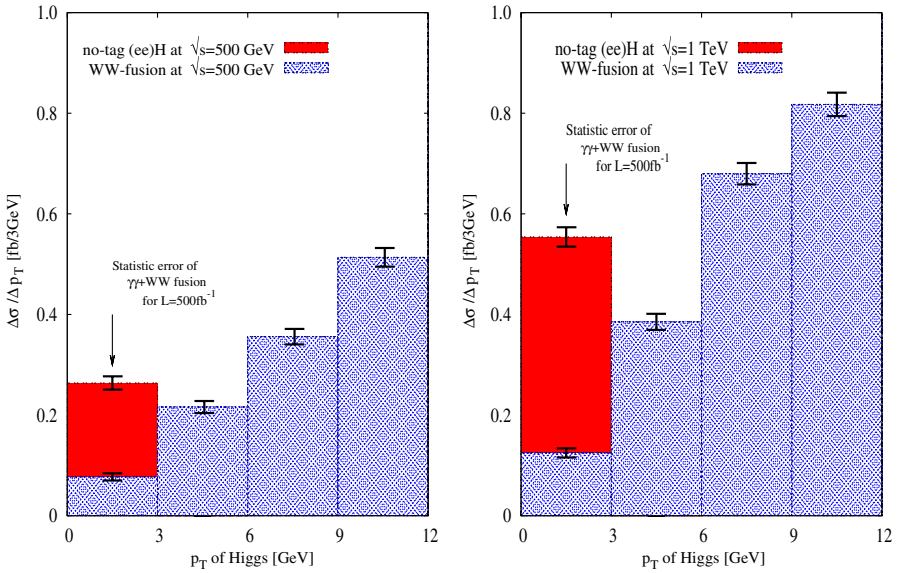

FIG. 8 (color online). The histograms for the number of events at low Higgs p_T.

$$c_{2\gamma\gamma}^{\mathrm{SM}} + \Delta c_{2\gamma\gamma} = -0.00187 \begin{cases} +0.000\,074 \\ -0.000\,077 \end{cases} \quad \text{at } \sqrt{s} = 500 \text{ GeV}; L = 500 \text{ fb}^{-1}, \tag{141a}$$

$$c_{2\gamma\gamma}^{\mathrm{SM}} + \Delta c_{2\gamma\gamma} = -0.00187 \begin{cases} +0.000\,046 \\ -0.000\,047 \end{cases} \quad \text{at } \sqrt{s} = 1 \text{ TeV}; L = 500 \text{ fb}^{-1}. \tag{141b}$$

The above results show that the no-tag $(ee)H$ process at e^+e^- collider can measure the $H\gamma\gamma$ coupling with the 4% and 2% accuracy with the integrated luminosity of 500 fb^{-1} at $\sqrt{s} = 500$ GeV and 1 TeV, respectively. In contrast, the sensitivity of the double-tag eeH events on the $c_{2\gamma\gamma}$ coupling in Eqs. (125) and (126), gives the error of 0.0016 and 0.0014 at $\sqrt{s} = 500$ GeV and 1 TeV, respectively, with 500 fb^{-1}, which is barely enough to resolve the SM coupling at 1σ level. From this exercise, we can conclude that the no-tag $(ee)H$ process is about 20 to 30 times more sensitive to the $H\gamma\gamma$ coupling than double-tag eeH process, at $\sqrt{s} = 500$ GeV and 1 TeV, if our naive estimation of the background is valid.

This naive estimation of the errors is based on the assumption that the background contribution from the WW-fusion process can be estimated from the high p_T distribution. This assumption can be tested experimentally by using the different polarization dependence of the signal and the background. The background WW-fusion process scales as $1 - P$, i.e., it increases for $P < 0$ and decreases for $P > 0$, while the signal remains independent on P as long as positron is unpolarized. Once the positron polarization is available, both the total cross section and the rapidity distribution of the no-tag $(ee)H$ events depend on the sign of the product $P \cdot \bar{P}$, which should be a distinctive signature of the $\gamma\gamma$ fusion.

Although the sensitivity to the $H\gamma\gamma$ coupling is expected to be measured far more accurately with the photon-linear collider [28,29], our results show the sensitivity limit when it is not realized.

VIII. SINGLE-TAG $e^+e^- \to (e^\pm)e^\mp H$ PROCESS

This process essentially measures $e^\pm\gamma \to e^\pm H$, where the initial photon comes from the other $e^\mp$ beam as an equivalent real photon. Since we have studied both double-tag eeH and no-tag $(ee)H$ events, it is worthwhile to examine the single-tag $(e)eH$ process for completeness.

A. Cross section

The momentum and the helicity assignments of the single-tag $(e)eH$ process are also the same as those in the double-tag eeH process in Eq. (110). We use the equivalent real photon approximation for the current from the untagged $e^\pm$. Since the helicity of the equivalent real photon depends on the parent $e^\pm$ helicity, and also the electroweak interactions of the tagged $e^\pm$ current are sensitive to their polarization, we give the general expression of the cross section with both e^- and e^+ beam polarizations, P and $\bar{P}$, respectively;

$$\begin{aligned} \sigma^{(e)eH} = & \sum_{\alpha,\beta} \left(\frac{1+\alpha P}{2}\right)\left(\frac{1+\beta\bar{P}}{2}\right) \\ & \times \left[\sum_{\lambda_2'} \hat{\sigma}^{e^-\gamma\to e^-H}_{\alpha\lambda_2'} D^{\beta\lambda_2'}_{\gamma/e}(z, Q^2) \right. \\ & \left. + \sum_{\lambda_1'} \hat{\sigma}^{e^+\gamma\to e^+H}_{\beta\lambda_1'} D^{\alpha\lambda_1'}_{\gamma/e}(z, Q^2) \right]. \end{aligned} \tag{142}$$

Here, the polarization-dependent real photon distributions

are as defined in Eq. (130), and the $e^{\pm}\gamma \to e^{\mp}H$ cross sections are

$$\hat{\sigma}^{e^{\pm}\gamma\to e^{\mp}H}_{\alpha\lambda_i'} = \frac{1}{2\hat{s}}\int |M^{e^{\pm}\gamma}_{\alpha\lambda_i'}|^2 d\Phi_2 = \frac{1}{32\pi\hat{s}}\left(1-\frac{m_H^2}{\hat{s}}\right)\int d\cos\theta^*_{e^{\pm}} |M^{e^{\pm}\gamma}_{\alpha\lambda_i'}|^2, \tag{143}$$

where $\hat{s} = sz$, $\alpha/2$ is the $e^{\pm}$ helicity, λ_i' is the photon helicity, and $\theta^*_{e^{\pm}}$ is the polar angle of the final tagged $e^{\pm}$ in the colliding $e^{\pm}\gamma$ c.m. frame, measured from the incoming $e^{\pm}$ momentum direction. The integration region of $\cos\theta^*_{e^{\pm}}$ is constrained by the tagging criteria of Eq. (32)

$$|\cos\theta_{e^{\pm}}| < 0.995 \equiv \cos\theta_{\min} \tag{144}$$

in the e^+e^- collision c.m. frame. We find

$$-1 + \frac{z(1-\cos\theta_{\min})}{[z+(1-z)(1+\cos\theta_{\min})/2]} < \cos\theta^*_{e^{\pm}} < 1 - \frac{1-\cos\theta_{\min}}{[z+(1-z)(1-\cos\theta_{\min})/2]}. \tag{145}$$

The interaction Lagrangian relevant for the $e^{\pm}\gamma \to e^{\pm}H$ process is

$$L_{\text{eff}} = \frac{1}{v}c_{2\gamma\gamma}A_{\mu\nu}A^{\mu\nu} + \frac{2}{v}(c_{2Z\gamma} - c_{3Z\gamma})HZ_{\mu\nu}A^{\mu\nu}. \tag{146}$$

The coupling $c_{2\gamma\gamma}$ dictates the γ-exchange amplitude, and the combination $c_{2Z\gamma} - c_{3Z\gamma}$ dictates the Z-exchange amplitude in Fig. 9. The helicity amplitudes for the $e^-\gamma \to e^-H$ process are expressed as

$$\begin{aligned} M^{e^-\gamma}_{\alpha\lambda_2'} &= j^{\mu}_{e^-(\alpha\alpha)}\left[\frac{-e}{t_1}\Gamma^{H\gamma\gamma}_{\mu\nu} + \frac{g^{Zee}_{\alpha}}{t_1-m_Z^2}\Gamma^{HZ\gamma}_{\mu\nu}\right]\epsilon^{\nu}(k_2', \lambda_2'), \\ &= -g_Z\sqrt{\hat{s}x_1}\frac{t_1-m_H^2}{m_Z}\left[\frac{-e}{t_1}c_{2\gamma\gamma} + \frac{g^{Zee}_{\alpha}}{t_1-m_Z^2}\right. \\ &\quad \left.\times(c_{2Z\gamma}-c_{3Z\gamma})\right]\sqrt{2}\sin\frac{\theta^*}{2} \\ &\quad \times\left[\delta_{\alpha\lambda_2'} - \frac{\hat{s}-m_H^2}{t_1-m_H^2}\frac{1+\cos\theta^*}{2}\right], \end{aligned} \tag{147}$$

where the $\Gamma^{HVV}_{\mu\nu}$ form factors are as in Eq. (13), $j^{\mu}_{e^-(\alpha\alpha)}$ is the massless t-channel current of Eq. (113a), $t_1 = (k_1 - p_1)^2 = -sx_1(1-\cos\theta^*)/2$, x_1 is the energy fraction of the tagged e^-, θ^* is the scattering angle in the $e^-\gamma$ rest frame, k_2' is the four momentum of the equivalent real photon emitted from e^+. The amplitudes for $e^+\gamma \to e^+H$ are obtained from Eq. (147) simply by replacing α, g^{Zee}_{α}, $t_1 = (k_1-p_1)^2$, and λ_2' by β, $g^{Zee}_{-\beta}$, $t_2 = (k_2-p_2)^2$, and λ_1', respectively, where θ^* is now the scattering angle between the initial and final e^+ in the $e^+\gamma$ rest frame.

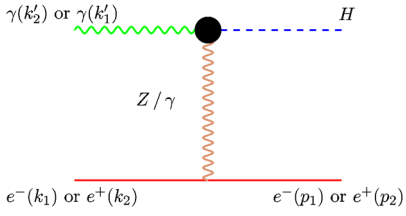

FIG. 9 (color online). Feynman diagram of $e^{\pm}\gamma \to e^{\pm}H$.

It is instructive to show that the single-tag $(e)eH$ cross section of Eq. (142) reduces to the no-tag $(ee)H$ cross section of Eq. (132) in the limit of $|t_1| \ll m_Z^2$. In this limit, the γ-exchange contribution dominates the amplitude, and by noting $\cos\theta^* \sim 1$ and $x_1 = 1 - m_H^2/\hat{s}$, Eq. (143) becomes

$$\begin{aligned} \hat{\sigma}^{e^-\gamma\to e^-H}_{\sigma\lambda} &\simeq \frac{g_Z^2e^2c_{2\gamma\gamma}^2m_H^2}{8\pi\hat{s}m_Z^2}\int\frac{d\cos\theta^*}{1-\cos\theta^*}(1-x_1) \\ &\quad\times\left[\delta_{\sigma\lambda} + \frac{x_1}{1-x_1}\right]^2, \\ &= \frac{1}{\hat{s}}\frac{16\pi^2}{m_H}\Gamma_{\gamma\gamma}\int\frac{dt}{t}\frac{\alpha}{2\pi}\left[\frac{\delta_{\sigma,\lambda}+\delta_{\sigma,-\lambda}x_1^2}{1-x_1}\right], \\ &= \frac{1}{\hat{s}}\frac{16\pi^2}{m_H}\Gamma_{\gamma\gamma}D^{\sigma\lambda}_{\gamma/e}(1-x_1, Q^2). \end{aligned} \tag{148}$$

Comparing the final expression of Eq. (148) with Eq. (130a), we find that the term proportional to z, in the $\sigma\lambda = +$distribution from the electron helicity flip amplitudes, is not reproduced, since we have neglected the electron mass of the tagged e^-. Inserting Eq. (148) in Eq. (143), we reproduce the cross section (132) for the no-tag $(ee)H$ events.

B. Error estimation for $c_{2\gamma\gamma}$ and $c_{2Z\gamma} - c_{3Z\gamma}$

To calculate the SM 1-loop contribution, we again adopt the approximation of replacing the 1-loop vertices by localized effective couplings

$$c_{2\gamma\gamma} = c^{\text{SM}}_{2\gamma\gamma} + \Delta c_{2\gamma\gamma}, \qquad c_{2Z\gamma} = c^{\text{SM}}_{2Z\gamma} + \Delta c_{2Z\gamma}. \tag{149}$$

It is important to note that since the virtuality of the tagged $e^{\pm}$ currents (t) can be larger than the weak-boson mass scale that dictates the spatial extension of the vertex, the approximation of Eq. (149) is not as excellent as that in Eq. (136) for the no-tag $(ee)H$ events. In evaluating the SM contribution, we therefore retain the t dependence of the loop function [30]

$$c^{\text{SM}}_{2\gamma\gamma} = c^{\text{SM}}_{2\gamma\gamma}(t), \qquad c^{\text{SM}}_{2Z\gamma} = c^{\text{SM}}_{2Z\gamma}(t), \tag{150}$$

and use the t-dependent "couplings" in the evaluation of the $e\gamma \to eH$ matrix elements. In other words, only the new physics contributions via $\Delta c_{2\gamma\gamma}$ and $\Delta c_{2Z\gamma}$ are assumed to be local in Eq. (149). With regard to the $H\gamma\gamma$ couplings, $c^{\text{SM}}_{2\gamma\gamma}(0) = -0.00\,187$ in Eq. (138) determines the $H \to \gamma\gamma$ width, while it reduces to

$c^{\rm SM}_{2\gamma\gamma}(-m_Z^2) = -0.00\,160$. Similarly, for the $HZ\gamma$ coupling, $c^{\rm SM}_{2Z\gamma}(m_Z^2) = -0.00\,322$ determines the $H \to Z\gamma$ width, while it reduces to $c^{\rm SM}_{2Z\gamma}(0) = -0.00\,276$ and $c^{\rm SM}_{2Z\gamma}(-m_Z^2) = -0.00\,243$, all for $m_H = 120$ GeV. As a consequence of the W boson dominance in the loop, we find that the ratio $c^{\rm SM}_{2Z\gamma}(m_Z^2)/c^{\rm SM}_{2\gamma\gamma}(0) \simeq 1.7$, is essentially the ratio of the W boson gauge couplings $g_{ZWW}/g_{\gamma WW} \simeq 1.8$. Since the effective couplings are gauge dependent when they are away from their on-shell limit, $t = 0$ for $c^{\rm SM}_{2\gamma\gamma}$ and $t = m_Z^2$ for $c^{\rm SM}_{2Z\gamma}$, respectively, the SM cross section based on the t-dependent effective couplings should be regarded only as an order of magnitude estimate. However, the box diagram contribution to the $e\gamma \to eH$ process, which is necessary to recover the gauge invariance, is found to be negligibly small numerically [30].

Because the single-tag $(e)eH$ process has small cross sections as shown in Fig. 3 and 4, we use only the total cross section to constrain the $H\gamma\gamma$ and $HZ\gamma$ couplings. In order to quantify the effects of the e^- beam polarization, we obtain the following parametrization for the single-tag e^- events for the e^- helicity α and unpolarized e^+[2].

$$\begin{aligned}\sigma_\alpha &= \frac{1}{2}\int dz \sum_{\lambda_1'} \sigma^{e^-\gamma\to e^- H}_{\alpha\lambda_1'} D_{\gamma/e^+}(z, Q^2) \\ &= A_\alpha (c_{2\gamma\gamma})^2 + B_\alpha (c_{2Z\gamma} - c_{3Z\gamma})^2 \\ &\quad + C_\alpha c_{2\gamma\gamma}(c_{2Z\gamma} - c_{3Z\gamma}). \end{aligned} \tag{151}$$

Here, the average over e^+ helicities is replaced by the sum over the photon helicity λ_1'. We find for $\sqrt{s} = 500$ GeV,

$$\begin{aligned}\sigma_R &= 15\,000(c_{2\gamma\gamma})^2 + 0890(c_{2Z\gamma} - c_{3Z\gamma})^2 \\ &\quad - 5500 c_{2\gamma\gamma}(c_{2Z\gamma} - c_{3Z\gamma}) = 0.025 \text{ fb}, \end{aligned} \tag{152a}$$

$$\begin{aligned}\sigma_L &= 15\,000(c_{2\gamma\gamma})^2 + 1200(c_{2Z\gamma} - c_{3Z\gamma})^2 \\ &\quad + 6400 c_{2\gamma\gamma}(c_{2Z\gamma} - c_{3Z\gamma}) = 0.066 \text{ fb}, \end{aligned} \tag{152b}$$

and for $\sqrt{s} = 1$ TeV,

$$\begin{aligned}\sigma_R &= 24\,000(c_{2\gamma\gamma})^2 + 2900(c_{2Z\gamma} - c_{3Z\gamma})^2 \\ &\quad - 15\,000 c_{2\gamma\gamma}(c_{2Z\gamma} - c_{3Z\gamma}) = 0.022 \text{ fb}, \end{aligned} \tag{153a}$$

$$\begin{aligned}\sigma_L &= 24\,000(c_{2\gamma\gamma})^2 + 3900(c_{2Z\gamma} - c_{3Z\gamma})^2 \\ &\quad + 17\,000 c_{2\gamma\gamma}(c_{2Z\gamma} - c_{3Z\gamma}) = 0.107 \text{ fb}. \end{aligned} \tag{153b}$$

The large coefficients of $(c_{2\gamma\gamma})^2$ indicate that the γ-exchange amplitude dominates the cross section even for the tagged events. The effects of the $HZ\gamma$ couplings can be measured from the interference between the γ-exchange and the Z-exchange amplitudes, which is destructive for e_R and constructive for e_L, reflecting the relative sign of their couplings, $g_L^{\gamma ee} = g_R^{\gamma ee} = -e$ and $g_L^{Zee} = g_Z(-1/2 + \sin^2\theta_{\rm W})$, $g_R^{Zee} = g_Z \sin^2\theta_{\rm W}$. Therefore, we expect that the beam polarization can be a powerful tool to distinguish the $HZ\gamma$ coupling from the $H\gamma\gamma$ coupling.

It is also worth noting that the cross section after the e tagging condition of Eq. (145) can become smaller at high energies, as we find for σ_R in Eqs. (152a) and (153a). In Fig. 10, we show the rapidity distribution of tagged e^- in the laboratory frame. Although the total cross section increases monotonically with $\sqrt{s}$, the distribution shifts to large η as $\sqrt{s}$ grows. It implies that more and more fraction of events escape detection ($\cos\theta_e > 0.995$ or $\eta_e > 2.99$) at high energies. The suppression of the cross section σ_R for ($\eta_e < 2.99$) as shown in Fig. 10, can be attributed to the cancellation between the γ and Z amplitudes for the tagged e_R, with large scattering angle in the $e^-\gamma$ rest frame.

In terms of the above parameterizations Eqs. (152) and (153), we can determine the total cross section for polarized e^- beam and unpolarized e^+ beam as follows:

$$\sigma^{e^- H}(P, \bar{P} = 0) = \left(\frac{1+P}{2}\right)\sigma_R + \left(\frac{1-P}{2}\right)\sigma_L, \tag{154a}$$

$$\sigma^{e^+ H}(P, \bar{P} = 0) = \frac{1}{2}(\sigma_R + \sigma_L). \tag{154b}$$

At $\sqrt{s} = 500$ GeV with $L = 500$ fb^{-1}, we find

$$\sigma^{e^- H}(P = +0.8, \bar{P} = 0) = 0.030(\pm 0.011) \text{ fb}, \tag{155a}$$

$$\sigma^{e^- H}(P = -0.8, \bar{P} = 0) = 0.062(\pm 0.016) \text{ fb}, \tag{155b}$$

$$\sigma^{e^+ H}(P = \pm 0.8, \bar{P} = 0) = 0.046(\pm 0.0096) \text{ fb}, \tag{155c}$$

and at $\sqrt{s} = 1$ TeV with $L = 500$ fb^{-1}, we find

$$\sigma^{e^- H}(P = +0.8, \bar{P} = 0) = 0.030(\pm 0.011) \text{ fb}, \tag{156a}$$

$$\sigma^{e^- H}(P = -0.8, \bar{P} = 0) = 0.098(\pm 0.020) \text{ fb}, \tag{156b}$$

$$\sigma^{e^+ H}(P = \pm 0.8, \bar{P} = 0) = 0.064(\pm 0.011) \text{ fb}. \tag{156c}$$

The errors in the parentheses are for $L = 250$ fb^{-1} each for $P = 0.8$ and $P = -0.8$.

From Eqs. (152) and (155), we find

$$\begin{matrix} c_{2Z\gamma} - c_{3Z\gamma} = -0.00\,201 \pm 0.0012 \\ c_{2\gamma\gamma} = -0.00\,166 \pm 0.00\,016 \end{matrix} \quad \begin{pmatrix} 1. & \\ -.71 & 1. \end{pmatrix} \tag{157}$$

at $\sqrt{s} = 500$ GeV. The mean values may be interpreted as the average of the t-dependent SM couplings in the tagged events, which turn out to be approximately $c^{\rm SM}_{2Z\gamma}(-m_Z^2)$ and $c^{\rm SM}_{2\gamma\gamma}(-m_Z^2)$, but with slightly smaller magnitudes. The smallness of the magnitude of $\langle c^{\rm SM}_{2Z\gamma}(t)\rangle$ reflects the larger mean value of the momentum transfer $\langle |t| \rangle$ in the γ-Z interference than in the purely γ-exchange contribution.

[2]The coefficient A_α is determined by evaluating the γ-exchange contribution only, such that the SM cross section is reproduced with a constant $c_{2\gamma\gamma}$, which may be interpreted as the average of $(c_{2\gamma\gamma})^2 = \langle c^{\rm SM}_{2\gamma\gamma}(t)^2\rangle_{\gamma\gamma}$. Likewise, the coefficient C_α is determined by requiring that the SM contribution to the γ-Z exchange interference is reproduced for a constant value of $c_{2\gamma\gamma}(c_{2Z\gamma} - c_{3Z\gamma}) = \langle c^{\rm SM}_{2\gamma\gamma}(t)\rangle_{\gamma\gamma}\langle c^{\rm SM}_{2Z\gamma}(t)\rangle_{Z\gamma}$. Finally, the coefficient B_α is fixed by demanding that the total SM cross section is reproduced for the above average values.

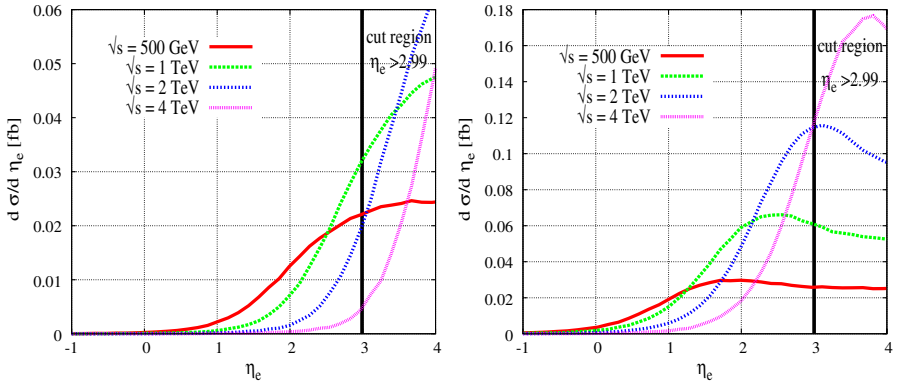

(a) Rapidity distributions for σ_R (b) Rapidity distributions for σ_L

FIG. 10 (color online). The rapidity distributions of tagged e^- in the lab. Frame for each initial helicity state and at each collision energy. The thick solid line shows the detection limit, above which e^- escape detection.

When we compare the result Eq. (157) with that of the no-tag $(ee)H$ events in Eq. (141a), we find that the no-tag events are about a factor 2 more sensitive to the $H\gamma\gamma$ coupling. On the other hand, the sensitivity to the $HZ\gamma$ coupling, ± 0.0012, is 1 order of magnitude worse than that of the ZH process in Eq. (108) rescaled for $L = 500$ fb^{-1}. Hence, the measurements of the single-tag $(e)eH$ events do not improve the constraint on the $HZ\gamma$ coupling significantly.

For $\sqrt{s} = 1$ TeV, we find

$$\begin{matrix} c_{2Z\gamma} - c_{3Z\gamma} = -0.00\,180 \pm 0.00\,063 \\ c_{2\gamma\gamma} = -0.00\,145 \pm 0.00\,014 \end{matrix} \quad \begin{pmatrix} 1. & \\ -.77 & 1. \end{pmatrix} \tag{158}$$

from Eqs. (153) and (156). The magnitudes of the mean values decrease slightly from those of Eq. (157) at $\sqrt{s} = 500$ GeV, because of the higher value of the typical momentum transfer $|t|$ at $\sqrt{s} = 1$ TeV. The error of $c_{2\gamma\gamma}$ is almost a factor of 3 larger than that of the no-tag $(ee)H$ events, Eq. (141b), while that of $c_{3Z\gamma}$ is more than 1 order of magnitude larger than that from ZH events in Eq. (109), rescaled for $L = 500$ fb^{-1}.

Although the process $e\gamma \to eH$ gives us clean measurements of the $HZ\gamma$ couplings with e^- beam polarization, the sensitivity is rather low in e^+e^- collisions because of the small and soft photon flux from the bremsstrahlung. This process will become more important once the photon-linear collider option is realized [30].

IX. LUMINOSITY UNCERTAINTY

So far, the errors and their correlations based on the optimal observables method for Higgs-gauge-boson effective couplings are computed by assuming the true luminosity L. However, the error in the measurement of the L can affect the measurements of some effective couplings. We attempt here to study the impact of the luminosity uncertainty on the precision measurements of the HVV couplings.

In the presence of the luminosity uncertainty, the true luminosity L can be estimated as

$$L = f\bar{L}, \qquad f = 1 \pm \Delta f, \tag{159}$$

where $\bar{L}$ is the measured mean value, and Δf is its 1-σ uncertainty. The χ^2 function given in Eq. (23) of Sec. III should then be redefined as follows:

$$\chi^2(c_i) \to \chi^2(c_i; f) = \sum_{k=1}^{N} \left(\frac{N^k_{\rm exp} - N^k_{\rm th}(c_i)}{\sqrt{N^k_{\rm exp}}} \right)^2 + \left(\frac{f-1}{\Delta f} \right)^2, \tag{160a}$$

$$= \sum_{k=1}^{N} \left(\frac{L\Sigma_{\rm SM}(\Phi_k)\Delta - \bar{L}[\Sigma_{\rm SM}(\Phi_k) + \sum_{i=1}^{n} c_i \Sigma_i(\Phi_k)]\Delta}{\sqrt{L\Sigma_{\rm SM}(\Phi_k)\Delta}} \right)^2 + \left(\frac{f-1}{\Delta f} \right)^2, \tag{160b}$$

$$= \bar{L} \sum_{k=1}^{N} \frac{[(f-1)\Sigma_{\rm SM}(\Phi_k) + \sum_{i=1}^{n} c_i \Sigma_i(\Phi_k)]^2}{\Sigma_{\rm SM}(\Phi_k)} \Delta + \left(\frac{f-1}{\Delta f} \right)^2, \tag{160c}$$

$$\overset{N\to\infty}{\to} \sum_{i=0}^{n} \sum_{j=0}^{n} c_i (V_f^{-1})_{ij} c_j + \left(\frac{f-1}{\Delta f} \right)^2, \tag{160d}$$

where

$$(V_f^{-1})_{ij} = \bar{L}\int \frac{\Sigma_i(\Phi)\Sigma_j(\Phi)}{\Sigma_{\rm SM}(\Phi)}d\Phi \tag{161}$$

is now $(n+1)\times(n+1)$ matrix with

$$c_0 = f-1, \qquad \Sigma_0(\Phi) = \Sigma_{\rm SM}(\Phi). \tag{162}$$

It is straightforward to integrate out the $c_0 = f-1$ dependence and obtain the probability distribution of the parameters c_1 to c_n in the presence of the luminosity uncertainty. In our study, we note that the two couplings, c_{1WW} and c_{1ZZ} have the weight functions that are identical to the SM distribution.[3] Because of this, we can study the impacts of the luminosity uncertainty algebraically by using the χ^2 functions written in terms of c_{1WW} and c_{1ZZ}. We use

$$\Sigma_{c_{1WW}}(\Phi) = 2\Sigma_{\rm SM}(\Phi) \tag{163}$$

for the WW-fusion process given in Eq. (45), and

$$\Sigma_{c_{1ZZ}}(\Phi) = 2\Sigma_{\rm SM}(\Phi), \tag{164}$$

for the ZH production and double-tag eeH processes given in Eqs. (73) and (110), respectively. We can express the total χ^2 function with the luminosity uncertainty given in Eq. (161) for a particular c.m. energy, $\sqrt{s}$ as

$$\chi^2(c_i;f)_{\sqrt{s}} = \chi^2\Big(c_{1WW}\to c'_{1WW} = c_{1WW} + \frac{f-1}{2}\Big)^{HWW}_{\sqrt{s}} + \chi^2\Big(c_{1ZZ}\to c'_{1ZZ} = c_{1ZZ} + \frac{f-1}{2}\Big)^{HZZ}_{\sqrt{s}} + \Big[\frac{f-1}{(\Delta f)_{\sqrt{s}}}\Big]^2. \tag{165}$$

In the following analysis, we assume that the luminosity uncertainty is common to all the processes at each collision energy $\sqrt{s}$.

Let us examine the effects at $\sqrt{s} = 500$ GeV in some detail. The χ^2 function for the HWW process in Eq. (62) can be expressed in the form

$$\chi^2(c_{1WW}\to c'_{1WW})^{HWW}_{500} = \sum_{i,j} c'_{iWW}[(V^{HWW}_{500})^{-1}]_{ij}c'_{jWW}, \tag{166}$$

where $c'_{1WW} = c_{1WW} + (f-1)/2$, $c'_{iWW} \equiv c_{iWW}$ $(i\neq 1)$. Likewise, the χ^2 function from the ZH and the double-tag eeH processes in Secs. V and VI can be expressed as

$$\chi^2(c_{1ZZ}\to c'_{1ZZ})^{HZZ}_{500} = \sum_{k,l} c'_k[(V^{HZZ}_{500})^{-1}]_{kl}c'_l, \tag{167}$$

where $c'_{1ZZ} = c_{1ZZ} + (f-1)/2$ and c'_2, c'_3, c'_4, c'_5, $c'_6 \equiv c_{2ZZ}$, c_{3ZZ}, $c_{2Z\gamma}$, $c_{3Z\gamma}$, $c_{2\gamma\gamma}$. Now, the luminosity uncertainty in the χ^2 function of Eq. (165) at $\sqrt{s} = 500$ GeV can easily be factored out as

$$\chi^2(c_i;f)_{500} = \Big[\frac{f-1}{(\Delta f)^{\rm eff}_{500}} + (\Delta f)^{\rm eff}_{500}R\Big]^2 + \tilde{\chi}^2(c_i)_{500}, \tag{168}$$

where

$$\frac{1}{[(\Delta f)^{\rm eff}_{500}]^2} = \frac{1}{[(\Delta f)_{500}]^2} + \frac{1}{4}[(V^{HWW}_{500})^{-1}]_{11} + \frac{1}{4}[(V^{HZZ}_{500})^{-1}]_{11}, \tag{169a}$$

$$R = \frac{1}{2}\Big(\sum_{k=1}^{3} c_{kWW}[(V^{HWW}_{500})^{-1}]_{1k} + \sum_{k=1}^{6} c_k[(V^{HZZ}_{500})^{-1}]_{1k}\Big), \tag{169b}$$

and the reduced χ^2 function is

$$\tilde{\chi}^2(c_i)_{500} = \chi^2(c_i)_{500} - [(\Delta f)^{\rm eff}_{500}]^2R^2. \tag{170}$$

We can use the reduced χ^2 function to study the constraints on the nonstandard couplings in the presence of the luminosity uncertainty. It should be noted that because of the last term of Eq. (170) there appear correlations between the HWW couplings and the $HZZ/HZ\gamma/H\gamma\gamma$ coupling measurements. Therefore, the effects of the luminosity uncertainty is important when we study the constraints on the coefficients of the dimension-six operators, Eq. (12), since some of them contribute to both couplings.

The reduced χ^2 function of Eq. (170) gives a 9×9 covariance matrix. The results for $\sqrt{s} = 500$ GeV, $L = 500$ fb^{-1}, and $\Delta f = 0.01$ can be expressed as,

[3]For no-tag $(ee)H$ and single-tag $(e)eH$ processes, the $H\gamma\gamma$ and $HZ\gamma$ couplings of the SM at one-loop order are used to calculate the SM cross sections. There, however, the statistical error is dominated, and the errors due to the luminosity uncertainty can be safely neglected.

$$\begin{array}{l} c_{1WW} = \pm.045 \\ c_{2WW} = \pm.046 \\ c_{3WW} = \pm.013 \\ c_{1ZZ} = \pm.013 \\ c_{2ZZ} = \pm.00\,059 \\ c_{3ZZ} = \pm.00\,044 \\ c_{2Z\gamma} = \pm.00\,037 \\ c_{3Z\gamma} = \pm.000\,080 \\ c_{2\gamma\gamma} = \pm.0022 \end{array} \begin{pmatrix} 1 & & & & & & & & \\ .990 & 1 & & & & & & & \\ .991 & .995 & 1 & & & & & & \\ .043 & 0. & 0. & 1 & & & & & \\ .0 & 0. & 0. & -.63 & 1 & & & & \\ .0 & 0. & 0. & -.81 & .033 & 1 & & & \\ .0 & 0. & 0. & -.006 & -.063 & .043 & 1 & & \\ .0 & 0. & 0. & .0 & .050 & -.046 & -.83 & 1 & \\ .0 & 0. & 0. & .22 & -.27 & -.28 & -.040 & .034 & 1 \end{pmatrix}. \tag{171}$$

When the above results are compared with those without the luminosity uncertainty in Eq. (63) for the HWW couplings and the corresponding expression for the $HZZ/HZ\gamma/H\gamma\gamma$ couplings, after rescaling of the errors by $1/\sqrt{5} \simeq 0.447$, we find the following: The errors of c_{1WW} and c_{1ZZ} are slightly larger than $1/\sqrt{5}$ of the corresponding statistical errors, while all the other errors are not affected much. The correlations between c_{1WW} and c_{2WW} or c_{3WW} are reduced slightly in magnitude from Eq. (63), and those correlations between c_{1ZZ} and the other HZZ, $HZ\gamma$, $H\gamma\gamma$ couplings are also reduced slightly in magnitude. Finally, the off-diagonal subcorrelation matrix in Eq. (171) is almost vacant except for the (c_{1WW}, c_{1ZZ}) component, which shows positive correlation because the luminosity uncertainty affects both c_{1WW} and c_{1ZZ} couplings in the same way. All the effects of the luminosity uncertainty are rather small because the statistical errors of c_{1WW} and c_{1ZZ} are ± 0.045 and ± 0.013, respectively, which are significantly larger than the error from the postulated luminosity uncertainty $\Delta f/2 = 0.005$. When the errors due to the luminosity uncertainty become dominant, the errors of c_{1WW} and c_{1ZZ} will stop decreasing with the luminosity, and the correlation between c_{1WW} and c_{1ZZ} will grow.

It is instructive to study the impact of the luminosity uncertainty analytically in a very simplified example where only the two couplings, c_{1WW} and c_{1ZZ}, are retained in the amplitudes at $\sqrt{s} = 500$ GeV. In this limit, the reduced χ^2 function of Eq. (170) is simply

$$\begin{aligned} \tilde{\chi}^2(c_i)_{500} &= c_{1WW}^2[(V_{500}^{HWW})^{-1}]_{11} + c_{1ZZ}^2[(V_{500}^{HZZ})^{-1}]_{11} \\ &\quad - \frac{1}{4}[(\Delta f)_{500}^{\rm eff}]^2(c_{1WW}[(V_{500}^{HWW})^{-1}]_{11} \\ &\quad + c_{1ZZ}[(V_{500}^{HZZ})^{-1}]_{11})^2, \\ &= \left(\frac{c_{1WW}}{\Delta c_{1WW}}\right)^2 + \left(\frac{c_{1ZZ}}{\Delta c_{1ZZ}}\right)^2 \\ &\quad - \frac{1}{4}[(\Delta f)_{500}^{\rm eff}]^2\left[\frac{c_{1WW}}{(\Delta c_{1WW})^2} + \frac{c_{1ZZ}}{(\Delta c_{1ZZ})^2}\right]^2, \end{aligned} \tag{172}$$

where the combined error of $(\Delta f)_{500}^{\rm eff}$ is

$$[(\Delta f)_{500}^{\rm eff}]^{-2} = [(\Delta f)_{500}]^{-2} + \frac{1}{4}(\Delta c_{1WW})^{-2} + \frac{1}{4}(\Delta c_{1ZZ})^{-2}. \tag{173}$$

As noted above, the second term in Eq. (172) generates the correlation between the errors of c_{1WW} and c_{1ZZ}. For example, if we take the limit where the statistical errors are much smaller than the luminosity uncertainty, $(\Delta c_{1WW})^2, (\Delta c_{1ZZ})^2 \ll (\Delta f)^2$, the above reduced χ^2 function can be expressed as

$$\begin{aligned} \tilde{\chi}^2(c_i)_{500} &\overset{(\Delta c_{1VV})^2 \ll \Delta f^2}{\longrightarrow} \frac{(c_{1WW} - c_{1ZZ})^2}{(\Delta c_{1WW})^2 + (\Delta c_{1ZZ})^2} \\ &\quad + \frac{4}{(\Delta f)^2}\frac{[(\Delta c_{1ZZ})^2 c_{1WW} + (\Delta c_{1WW})^2 c_{1ZZ}]^2}{[(\Delta c_{1WW})^2 + (\Delta c_{1ZZ})^2]^2} \\ &\quad + \mathcal{O}\left(\frac{1}{(\Delta f)^4}\right). \end{aligned} \tag{174}$$

In the leading term, only the combination $(c_{1WW} - c_{1ZZ})$ is constrained, and the next-to-leading term proportional to $1/(\Delta f)^2$ constrain the combination $(\Delta c_{1ZZ})^2 c_{1WW} + (\Delta c_{1WW})^2 c_{1ZZ}$. In the limit of large statistics, the first term dominates the χ^2 function and the correlation approaches the unity.

In Fig. 11, we show the errors of c_{1WW} and c_{1ZZ} couplings as a function of the integrated luminosity L for the luminosity uncertainty $\Delta f = 0.01$ at $\sqrt{s} = 500$ GeV. The solid line shows the error of the combination $c_{1WW} - c_{1ZZ}$, which decreases as $1/\sqrt{L}$ asymptotically, since the luminosity uncertainty is canceled out by taking the difference. On the other hand, the dashed line for c_{1WW}, and the dashed-dotted line for c_{1ZZ}, approaches the same value $(\Delta f)/2$, showing that the individual errors will be dominated by the luminosity uncertainty. More explicitly, the errors of the couplings, c_{1WW} and c_{1ZZ}, can be expressed as

$$\begin{aligned} c_{1WW} &= \pm\sqrt{\left(\frac{\Delta f}{2}\right)^2 + (\Delta c_{1WW})^2}, \\ c_{1ZZ} &= \pm\sqrt{\left(\frac{\Delta f}{2}\right)^2 + (\Delta c_{1ZZ})^2}, \end{aligned} \tag{175a}$$

with the correlation

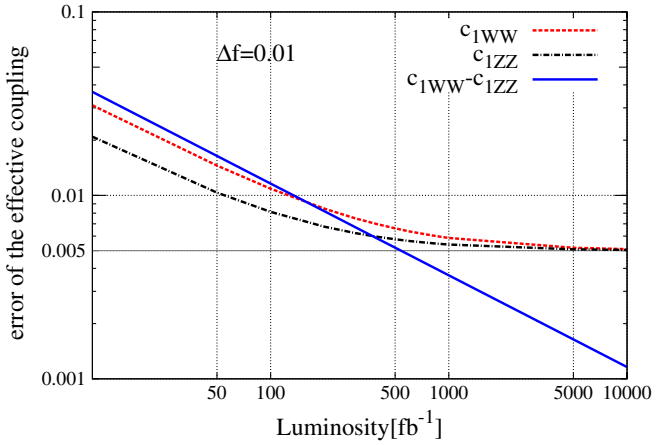

FIG. 11 (color online). Error of c_{1WW} and c_{1ZZ} vs integrated Luminosity at $\sqrt{s} = 500$ GeV when the luminosity uncertainty is $\Delta f = 0.01$.

$$\rho = \left[\left(1 + 4\frac{(\Delta c_{1WW})^2}{(\Delta f)^2}\right)\left(1 + 4\frac{(\Delta c_{1ZZ})^2}{(\Delta f)^2}\right)\right]^{-(1/2)}. \tag{175b}$$

X. CONCLUSION AND DISCUSSION

The imprint of the dynamics of the symmetry breaking physics is inherent in the interactions of the Higgs boson and the gauge bosons. In this article, we attempt to evaluate the potential of the future linear e^+e^- colliders, such as the ILC, in probing the dynamics of all the CP-even and gauge-invariant dimension-six operators of the SM fields that affect the Higgs-gauge-boson couplings when there is one SM-like light Higgs boson. For this purpose, we study all the processes that are sensitive to the HVV couplings: the $\nu_e\bar{\nu}_e H$ production via WW fusion is sensitive to HWW couplings, the ZH production process is sensitive to HZZ and $HZ\gamma$ couplings, the double-tag eeH production process via t-channel Z and γ exchange is also sensitive to HZZ, $HZ\gamma$, and $H\gamma\gamma$ coupling, the no-tag $(ee)H$ process measures the $H\gamma\gamma$ coupling, and the single-tag $(e)eH$ process measures $HZ\gamma$ and $H\gamma\gamma$ couplings. In order to quantify the resolving power of each process, we allow all the effective HVV couplings to vary freely in the fit and adopt the optimal observables method to constrain them in each process, at a few selected collision energies ($\sqrt{s} =$ 250, 350, 500, 1000 GeV), and with or without e^- beam polarization.

A. Summary of the constraints on the HVV couplings

Here, we summarize our results for the effective HVV couplings at the ILC.

(i) All our results have been presented for nominal integrated luminosity of $L_0 = 100$ fb^{-1}, except for the no-tag $(ee)H$ and single-tag $(e)eH$ events, where we give our error estimates for $L = 500$ fb^{-1} at $\sqrt{s} = 500$ GeV and 1 TeV only.

(ii) Most of our results have been given for e^- beam polarization of $|P| = 80\%$ with no e^+ beam polarization $|\bar{P}|$=0, where exactly half of the total integrated luminosity L is delivered with $P = |P|$ and $P = -|P|$.

(iii) Results for $|P| = |\bar{P}| = 0$ have also been calculated for all the cases [24], but presented only for the ZH production process at $\sqrt{s} = 250$ GeV; see Eq. (104).

(iv) Our results for the HWW effective couplings are shown in Eq. (66) for $\sqrt{s} = 250$ GeV, Eq. (67) for $\sqrt{s} = 350$ GeV, Eq. (62) for $\sqrt{s} = 500$ GeV, and Eq. (68) for $\sqrt{s} = 1$ TeV.

(v) The results for the HZZ and $HZ\gamma$ couplings in ZH production process with $|P| = 80\%$ are shown in Eq. (106) for $\sqrt{s} = 250$ GeV, Eq. (107) for $\sqrt{s} =$ 350 GeV, Eq. (108) for $\sqrt{s} = 500$ GeV, and Eq. (109) for $\sqrt{s} = 1$ TeV.

(vi) The results for the HZZ, $HZ\gamma$ and $H\gamma\gamma$ couplings in double-tag eeH process from t-channel vector-boson fusion with $|P| = 80\%$ are shown in Eq. (123) for $\sqrt{s} = 250$ GeV, Eq. (124) for $\sqrt{s} =$ 350 GeV, Eq. (125) for $\sqrt{s} = 500$ GeV, and Eq. (126) for $\sqrt{s} = 1$ TeV.

(vii) The $H\gamma\gamma$ coupling results from the no-tag $(ee)H$ process are given for $L = 500$ fb^{-1} in Eq. (141a) at $\sqrt{s} = 500$ GeV, and in Eq. (141b) at $\sqrt{s} =$ 1 TeV.

(viii) The $HZ\gamma$ and $H\gamma\gamma$ coupling results from the single-tag $(e)eH$ process for $L = 500$ fb^{-1} with $|P| = 80\%$ are given in Eq. (157) at $\sqrt{s} =$ 500 GeV, and in Eq. (158) at $\sqrt{s} = 1$ TeV.

(ix) The impact of the luminosity uncertainty, $L = f\bar{L}$ with $f = 1 \pm \Delta f$, should be taken into account according to Eq. (165), where the coefficients c_{1WW} and c_{1ZZ} in the χ^2 function at each energy is replaced by $c'_{1VV} = c_{1VV} + (f-1)/\Delta f$ and by adding the term $(f-1)^2/(\Delta f)^2$ at each energy. After squaring out the $(f-1)$ dependence, we obtain the reduced χ^2 function $\tilde{\chi}^2(c_i)$ at each energy.

The combined analyses in this section are performed by gathering all the above results, by adding all the χ^2 functions with appropriate weights.

In particular, we report the following two cases:

$$\chi^2(c_i)_{\rm I} = \frac{L_{250}}{L_0}\tilde{\chi}^2(c_i)_{250} + \frac{L_{350}}{L_0}\tilde{\chi}^2(c_i)_{350} + \frac{L_{500}}{L_0}\tilde{\chi}^2(c_i)_{500}, \tag{176a}$$

$$\chi^2(c_i)_{\rm I+II} = \chi^2(c_i)_{\rm I} + \frac{L_{1000}}{L_0}\tilde{\chi}^2(c_i)_{1000}, \tag{176b}$$

where $\chi^2(c_i)_{\rm I}$ gives the combined results of the ILC phase I with the maximum energy of $\sqrt{s} = 500$ GeV and $\chi^2(c_i)_{\rm I+II}$ gives that of combining the results from ILC-I and ILC-II at $\sqrt{s} = 1$ TeV. The reduced χ^2 function at each energy, $\tilde{\chi}^2(c_i)_{\sqrt{s}}$, are obtained for the luminosity uncertainty of $(\Delta f)_{\sqrt{s}}$ at each energy.

Since we present the individual covariance matrix separately in each process at $\sqrt{s} = 250$ GeV, 350 GeV, 500 GeV, and 1 TeV, in terms of its eigenvectors and square root of eigenvalues, we can estimate the constraints for an arbitrary integrated luminosity with an arbitrary luminosity uncertainty Δf at each energy. As an example, we show the results for

$$L_{250} = L_{350} = 100\ \text{fb}^{-1}, \qquad L_{500} = L_{1000} = 500\ \text{fb}^{-1}, \tag{177}$$

when the luminosity uncertainty is $\Delta f = 1\%$ at all energies.

Using the χ^2 function defined in Eq. (176a), we evaluate the errors and correlations of the effective couplings for ILC-I, with the integrated luminosities given in Eq. (177) and obtain

$$\begin{array}{l}
c_{1WW} = \pm.022 \\
c_{2WW} = \pm.023 \\
c_{3WW} = \pm.0065 \\
c_{1ZZ} = \pm.0067 \\
c_{2ZZ} = \pm.00\,048 \\
c_{3ZZ} = \pm.00\,021 \\
\Delta c_{2Z\gamma} = \pm.00\,030 \\
c_{3Z\gamma} = \pm.000\,073 \\
\Delta c_{2\gamma\gamma} = \pm.000\,075
\end{array}
\begin{pmatrix}
1 & & & & & & & & \\
.96 & 1 & & & & & & & \\
.96 & .98 & 1 & & & & & & \\
.17 & .0 & .0 & 1 & & & & & \\
-.0 & .0 & .0 & -.49 & 1 & & & & \\
.0 & .0 & .0 & -.26 & -.16 & 1 & & & \\
-.0 & .0 & .0 & .0 & -.067 & .072 & 1 & & \\
.0 & .0 & .0 & -.001 & .049 & -.090 & -.81 & 1 & \\
.0 & .0 & .0 & .004 & -.006 & -.002 & -.001 & .001 & 1
\end{pmatrix}. \tag{178}$$

When we compare the above combined results from the three ILC-I energies with those of Eq. (171) at $\sqrt{s} = 500$ GeV, we observe the following: As for the HWW couplings, we observe reduction of the errors of all the 3 couplings and that of correlations. This is essentially because contributions have different dependence on $\sqrt{s}$. As for the $HZZ/HZ\gamma/H\gamma\gamma$ couplings, the errors of c_{2ZZ}, c_{3ZZ}, $c_{2Z\gamma}$ and $c_{3Z\gamma}$ are essentially determined by the $\sqrt{s} = 500$ GeV experiment, while that of c_{1ZZ} is reduced significantly by including the lower energy data, because the ZH production cross section is larger at lower energies, see Fig. 3. The error of $c_{2\gamma\gamma}$ is essentially determined by the no-tag $(ee)H$ events. We find that the single-tag $(e)eH$ events, Eq. (157), do contribute significantly to improve the $HZ\gamma$ couplings measurement.

Only the errors of c_{1WW} and c_{1ZZ} and the corresponding rows of the correlation matrix are affected by the luminosity uncertainty $\Delta f = 0.01$ at each energy, assumed in the fit. By combining the results of Eqs. (62), (64), and (65) we obtain the combined error of c_{1WW} without the luminosity uncertainty to be 0.025, which is still 5 times larger than the error due to the luminosity uncertainty, $\Delta f/2 = 0.005$ at each energy. Therefore, the error of c_{1WW} does not increase significantly with the inclusion of the luminosity error. On the other hand, by combining the results at $\sqrt{s} = 250$, 350, and 500 GeV, we find that the combined error of c_{1ZZ} without the luminosity uncertainty is 0.0045, which is comparable to the error due to the luminosity uncertainty. We therefore find almost a 30% larger error for c_{1ZZ} in Eq. (178). The correlation between c_{1WW} and c_{1ZZ} is now 0.17, which is still small because the statistical error of c_{1WW} is much larger than the error due to the luminosity uncertainty.

After combining the ILC-I and ILC-II results with the integrated luminosities of Eq. (177), we find

$$\begin{array}{l}
c_{1WW} = \pm.0089 \\
c_{2WW} = \pm.0077 \\
c_{3WW} = \pm.0015 \\
c_{1ZZ} = \pm.0058 \\
c_{2ZZ} = \pm.00\,032 \\
c_{3ZZ} = \pm.000\,063 \\
\Delta c_{2Z\gamma} = \pm.00\,018 \\
c_{3Z\gamma} = \pm.000\,023 \\
\Delta c_{2\gamma\gamma} = \pm.000\,039
\end{array}
\begin{pmatrix}
1 & & & & & & & & \\
.80 & 1 & & & & & & & \\
.80 & .96 & 1 & & & & & & \\
.49 & .0 & .0 & 1 & & & & & \\
-.0 & .0 & .0 & -.36 & 1 & & & & \\
-.0 & .0 & .0 & -.10 & -.23 & 1 & & & \\
-.0 & .0 & .0 & -.003 & -.061 & .055 & 1 & & \\
.0 & .0 & .0 & .0 & .034 & -.096 & -.60 & 1 & \\
.0 & .0 & .0 & .003 & -.007 & -.0 & -.002 & .001 & 1
\end{pmatrix}. \tag{179}$$

The HWW couplings are measured much more accurately than the ILC-I alone case, mainly because of the large WW-fusion cross section at $\sqrt{s} = 1$ TeV; see Fig. 3. The correlations between the error of c_{1WW} and those of c_{2WW} and c_{3WW} are reduced because of the strong energy dependence of the contributions from the higher-dimensional operators, as discussed in Sec. IV. In contrast, the reduction of the error of c_{1ZZ} is marginal and the correlation between c_{1WW} and c_{1ZZ} grows to 0.49, reflecting the dominance of the luminosity uncertainty $\Delta f/2 = 0.005$. The errors of c_{3ZZ} and $c_{3Z\gamma}$ are a factor of 3 smaller than the ILC-I results in Eq. (178), mainly because of the strong energy dependence of their contributions; as discussed in Sec. VI. The error of $c_{2\gamma\gamma}$ is roughly half of the ILC-I result in Eq. (178), partly because of the 2.3 times larger cross section of the no-tag $(ee)H$ events, see Fig. 3 and Eqs. (140) and (141), and partly because of the contributions from the double-tag eeH events.

B. Comparison with other papers

First, we would like to compare our results with those of Ref. [13], as the present work is envisaged as an extension of this piece of work. The authors of Ref. [13] analyzed the ZH production process for $m_H = 120$ GeV both with unpolarized and 90% polarized e^- beam in e^+e^- collisions, using all the Z-boson decay modes. The study was based on the optimal observables method by allowing all the couplings to vary simultaneously. Although the formalism presented in Sec. V of this report is significantly more compact than that of Ref. [13], we reproduce all the errors and their correlations for both unpolarized and 90% polarized e^- beams at $\sqrt{s} = 250$ GeV as given in Eqs. (5.4) and (5.9), respectively, as well as Eq. (5.13) of Ref. [13], for $\sqrt{s} = 500$ GeV with 90% polarized e^- beam. Note that the authors in Ref. [13] considered the integrated luminosity 10 fb^{-1}, and therefore the errors in Eqs. (5.4), (5.9), and (5.13) should be multiplied by $1/\sqrt{10}$ for comparison with our results. It is worth noting here that the τ lepton polarization and the b jet charge identification with the efficiency 40% and 20%, respectively, considered in Ref. [13] have little impact on the final results once the e^- beam polarization is available. The reduction of the beam polarization from 90% considered in Ref. [13] to 80% in this report does lead to a slight increase in the error of the $HZ\gamma$ couplings by about 13%.

Next, we compare our results with Tables II and III of Ref. [15], where the authors estimated the 3σ bounds on c_{1ZZ}, c_{2ZZ}, c_{1WW} and c_{2WW} (Δa_Z, $\Delta b_Z/2$, Δa_W and $\Delta b_W/2$, respectively, in their notation). This analysis was performed for unpolarized e^+e^- collisions at $\sqrt{s} = 500$ GeV, with $L = 500$ fb^{-1} and $m_H = 120$ GeV. It is worth noting that to derive these bounds they vary one coupling at a time and hence the inclusion of the 1% systematic error (accruing from luminosity uncertainty, etc.) dominates their fluctuation estimation for all the observed cross sections. Their results can be easily reproduced from ours simply by setting all the couplings to zero except for the one whose error is estimated, in the respective χ^2 function for the specified process with an appropriate integrated luminosity, which should be corrected for the Higgs-boson decay branching fraction. The systematic error of 1% is then added to the statistical error in quadrature. For instance, the 3σ limit $|c_{1ZZ}| \leq 0.034$ [15] is found from the double-tag eeH process excluding the $Z \to e^+e^-$ events. To compare, we set all the other couplings to zero in the χ^2 function and find $c_{1ZZ} = \pm 0.0092$ for $L = 500$ fb^{-1} with $B(H \to b\bar{b}) = 0.9$. Now, adding the systematic error of 1% in quadrature we find $c_{1ZZ} = \pm 0.0105$ and the 3σ limit is $|c_{1ZZ}| \leq 0.032$. The limit $|c_{2ZZ}| \leq 0.0022$ [15] is obtained from the observed ZH production cross section, where Z decays to muon pair and light quarks (excluding b quark) pair have been considered. Under similar conditions we find the statistical error of $c_{2ZZ} = \pm .00\,059$. Since the luminosity error does not affect the measurement of c_{2ZZ}, this gives the 3σ limit of $|c_{2ZZ}| < 0.0018$, which shows an improvement by a factor of 1.3. We find that this difference is due to the use of the optimal observable, i.e., the differential distribution which is linear in c_{2ZZ}; the quoted limit in [15] is reproduced if we use only the c_{2ZZ} effects on the total cross section. Likewise, we reproduce the bound $|c_{1WW}|$, while we find a factor of 2 better bound on $|c_{2WW}|$, which can be attributed to our use of optimal weight function.

We also compare our results on c_{1ZZ} and c_{1WW} couplings with those of Ref. [17]. Since they studied possible constraint on the operator $\mathcal{O}_{\phi 2}$ ($\mathcal{O}_1$ in their notation), we present our comparison result in the next subsection; see the second footnote.

C. Constraints on the dimension-six operators

The constraints on the effective HVV couplings given in Eqs. (178) and (179) should be expressed as those of the 8 dimension-six operators of Eq. (2) in order to compare the power of ILC precision measurements with that of the other experiments. All the effective HVV couplings are linear combinations of the coefficients f_i/Λ^2's of these operators, as given in Eq. (12). It is clear from Eq. (12) that the coefficients $f_{\phi 1}$, $f_{\phi 2}$, $f_{\phi 4}$ cannot be determined uniquely from the HVV coupling measurements alone.[4] We therefore present constraints on two combinations of the three coefficients, $f_{\phi 1}$ and $3f_{\phi 4} - 2f_{\phi 2}$. Our results are hence for the 7 coefficients $f_{\phi 1}$, f_{BW}, f_W, f_B, f_{WW}, f_{BB}, and $3f_{\phi 4} - 2f_{\phi 2}$.

The combined ILC-I results of Eq. (178) lead to the following constraints on the dimension-six operators,

[4]For instance, the measurement of the triple Higgs-boson coupling is necessary to constrain all the three operators.

$$\begin{array}{l}
(\frac{1\ \mathrm{TeV}}{\Lambda})^2 f_{\phi 1} = \pm.091 \\
(\frac{1\ \mathrm{TeV}}{\Lambda})^2 f_{BW} = \pm.35 \\
(\frac{1\ \mathrm{TeV}}{\Lambda})^2 f_{W} = \pm.051 \\
(\frac{1\ \mathrm{TeV}}{\Lambda})^2 f_{B} = \pm.084 \\
(\frac{1\ \mathrm{TeV}}{\Lambda})^2 f_{WW} = \pm.22 \\
(\frac{1\ \mathrm{TeV}}{\Lambda})^2 f_{BB} = \pm.56 \\
(\frac{1\ \mathrm{TeV}}{\Lambda})^2 (3f_{\phi 4} - 2f_{\phi 2}) = \pm.36
\end{array}
\begin{pmatrix}
1 & & & & & & \\
-.40 & 1 & & & & & \\
.37 & .23 & 1 & & & & \\
.23 & -.49 & .35 & 1 & & & \\
.59 & -.91 & -.20 & .26 & 1 & & \\
-.49 & .98 & .22 & -.41 & -.96 & 1 & \\
-.052 & -.017 & .060 & .010 & .053 & -.032 & 1
\end{pmatrix}. \tag{180}$$

We find that the three coefficients, $f_{\phi 1}$, f_W, and f_B can be constrained rather accurately, with around 5% accuracy for $\Lambda = 1$ TeV, and rather independently of the other operators. The coefficient $f_{\phi 1}$ is measured accurately, because it contributes with the opposite sign to c_{1WW} and c_{1ZZ}; see Eqs. (12a) and (12b). In other words, $f_{\phi 1}$ is a measure of the difference between the HZZ and the HWW coupling strengths. On the other hand, the error of the $3f_{\phi 2} - 2f_{\phi 4}$ is rather large, since it measures the overall strengths of the HVV couplings. In fact, we find that it is only the error of $3f_{\phi 2} - 2f_{\phi 4}$, which is affected significantly by the luminosity uncertainty of $\Delta f = 0.01$. When we set $\Delta f = 0$, its error is reduced to 0.14,[5] but none of the errors of the other operators and their correlations are affected significantly. In addition, the three coefficients f_{BW}, f_{WW}, and f_{BB} are poorly constrained, while their errors are strongly correlated, with the correlation matrix elements of -0.91, 0.98, -0.96, suggesting the presence of their linear combination, which can be measured accurately. We therefore present constraints on the 6 operators, after integrating out the contributions from $3f_{\phi 2} - 2f_{\phi 4}$ Eq. (180), in terms of the eigenvectors and their errors

$$-.096f_{\phi 1} - .29f_{BW} - .26f_W + .31f_B + .73f_{WW} + .47f_{BB} = \pm.026, \tag{181a}$$
$$-.35f_{\phi 1} - .18f_{BW} + .84f_W - .28f_B + .21f_{WW} + .13f_{BB} = \pm.029, \tag{181b}$$
$$-.49f_{\phi 1} + .63f_{BW} + .077f_W + .47f_B + .22f_{WW} - .32f_{BB} = \pm.039, \tag{181c}$$
$$.59f_{\phi 1} + .020f_{BW} + .47f_W + .65f_B - .078f_{WW} + .062f_{BB} = \pm.088, \tag{181d}$$
$$.59f_{\phi 1} + .49f_{BW} + .057f_W - .43f_B + .53f_{WW} - .093f_{BB} = \pm.11, \tag{181e}$$
$$-.064f_{\phi 1} + .50f_{BW} + .016f_W - .052f_B - .31f_{WW} + .81f_{BB} = \pm.69. \tag{181f}$$

As anticipated, we find 3 combinations of the 6 coefficients, whose errors are smaller than 5% for $\Lambda = 1$ TeV. The worst constrained combination of Eq. (181f) has a much larger error of 68%, showing the poorly constrained combination of the three coefficients f_{BW}, f_{WW}, and f_{BB}, which leads to their large errors and the strong correlations among themselves in Eq. (180). It is worth noting here that the eigenvector of the most accurately measured combination in Eq. (181a) has a significant contribution from the constraint on $c_{2\gamma\gamma}$, which is proportional to $f_{BW} - f_{WW} - f_{BB}$ in Eq. (12e). In fact, if we drop the no-tag $(ee)H$ events from the analysis, the eigenvector with smallest error becomes essentially that of Eq. (181b) with a dominant f_W term, which contribute to the c_{3ZZ}, $c_{3Z\gamma}$ and c_{3WW} couplings in Eqs. (12g)–(12i). Also as expected, none of the results of Eq. (181), neither the eigenvectors nor errors, are affected significantly by the luminosity uncertainty of $\Delta f = 0.01$.

It is worth reporting here the importance of the e^- beam polarization to obtain the previous results. By setting $|P| = 0$, we find for the same ILC-I integrated luminosities and their errors of $\Delta f = 0.01$,

$$\begin{array}{l}
(\frac{1\ \mathrm{TeV}}{\Lambda})^2 f_{\phi 1} = \pm 0.17 \\
(\frac{1\ \mathrm{TeV}}{\Lambda})^2 f_{BW} = \pm 1.6 \\
(\frac{1\ \mathrm{TeV}}{\Lambda})^2 f_{W} = \pm 0.22 \\
(\frac{1\ \mathrm{TeV}}{\Lambda})^2 f_{B} = \pm 1.2 \\
(\frac{1\ \mathrm{TeV}}{\Lambda})^2 f_{WW} = \pm 0.61 \\
(\frac{1\ \mathrm{TeV}}{\Lambda})^2 f_{BB} = \pm 2.1 \\
(\frac{1\ \mathrm{TeV}}{\Lambda})^2 (3f_{\phi 4} - 2f_{\phi 2}) = \pm 0.38
\end{array}
\begin{pmatrix}
1 & & & & & & \\
.12 & 1 & & & & & \\
.45 & -.051 & 1 & & & & \\
-.62 & -.089 & -.91 & 1 & & & \\
.41 & -.83 & .21 & -.24 & 1 & & \\
-.031 & .986 & -.099 & .005 & -.91 & 1 & \\
.13 & .30 & -.078 & -.009 & -.14 & .26 & 1
\end{pmatrix}. \tag{182}$$

[5]The authors of Ref. [17] studied possible constraints on the dimension-six operator $\mathcal{O}_{\phi 2}$ ($\mathcal{O}_1$ in their notation), which affects the HZZ and HWW couplings by considering ZH production, WW-fusion and double-tag eeH processes. They found the uncertainty of 0.005 for the coupling $2c_{1ZZ} = 2c_{1WW}$ (a_1 in their notation) at $\sqrt{s} = 500$ GeV for $L = 1$ ab^{-1} with $B(H \to b\bar{b}) = 0.9$ and 80% b-tagging efficiency. Our result of $3f_{\phi 4} - 2f_{\phi 2} = \pm.14$ corresponds to $2c_{1ZZ} = 2c_{1WW} \approx \pm.0042$, even though the total integrated luminosity of our analysis is 700 fb^{-1}. This improvement is mainly due to the optimal observable method, but the luminosity uncertainty will limit our measurement.

It is striking to find that all the errors except that of $3f_{\phi 2} - 2f_{\phi 4}$ are larger by more than a factor of 3 to 9 for the same luminosity. This is essentially because of the incapability to resolve the nonstandard HZZ and $HZ\gamma$ couplings in the absence of beam polarization. On the other hand, we notice extremely strong correlations among the errors of f_{BW}, f_{WW}, and f_{BB}, and moderately strong correlation of -0.91 between the errors of f_W and f_B. We therefore give the eigenvectors and their errors for the three most accurately measured combinations after $3f_{\phi 4} - 2f_{\phi 2}$ is integrated out;

$$-.24f_{\phi 1} - .43f_{BW} + .27f_W + .052f_B + .66f_{WW} + .50f_{BB} = \pm.028, \tag{183a}$$

$$-.53f_{\phi 1} + .44f_{BW} + .64f_W + .12f_B + .052f_{WW} - .30f_{BB} = \pm.035, \tag{183b}$$

$$.72f_{\phi 1} - .092f_{BW} + .66f_W + .15f_B - .12f_{WW} + .045f_{BB} = \pm.083. \tag{183c}$$

It is remarkable that the error of the most accurately measured combination in Eq. (183a) is not much different from that of Eq. (181a). The reason is partly because both of them receive dominant contribution from the no-tag $(ee)H$ events that measure the $H\gamma\gamma$ coupling, which does not depend on the beam polarization. The second and the third combination of Eqs. (183b) and (183c) have dominant contributions from the f_W and $f_{\phi 1}$. Except for the these three combinations, all the other eigenvectors have errors larger than 0.1 for $\Lambda = 1$ TeV.

Finally, our results for the combined ILC-I and ILC-II analysis, Eq. (179) gives

$$\begin{array}{c} (\frac{1\ \mathrm{TeV}}{\Lambda})^2 f_{\phi 1} = \pm 0.56 \\ (\frac{1\ \mathrm{TeV}}{\Lambda})^2 f_{BW} = \pm .22 \\ (\frac{1\ \mathrm{TeV}}{\Lambda})^2 f_W = \pm .015 \\ (\frac{1\ \mathrm{TeV}}{\Lambda})^2 f_B = \pm .026 \\ (\frac{1\ \mathrm{TeV}}{\Lambda})^2 f_{WW} = \pm .14 \\ (\frac{1\ \mathrm{TeV}}{\Lambda})^2 f_{BB} = \pm .34 \\ (\frac{1\ \mathrm{TeV}}{\Lambda})^2 (3f_{\phi 4} - 2f_{\phi 2}) = \pm .34 \end{array} \quad \begin{pmatrix} 1 & & & & & & \\ -.42 & 1 & & & & & \\ .22 & .21 & 1 & & & & \\ .12 & -.32 & .32 & 1 & & & \\ .61 & -.91 & -.21 & .13 & 1 & & \\ -.51 & .98 & .21 & -.25 & -.96 & 1 & \\ .005 & -.005 & .029 & .002 & .028 & -.014 & 1 \end{pmatrix}. \tag{184}$$

When compared with the ILC-I only results of Eq. (180), we find that the errors of f_W and f_B are reduced to 1/3, those of $f_{\phi 1}$, f_{BW}, f_{WW} and f_{BB} are reduced to 2/3, while that of $3f_{\phi 2} - 2f_{\phi 4}$ remains the same. The reduction of the errors in f_B and f_W is a result of the strong constraints on the c_{3WW}, c_{3ZZ} and $c_{3Z\gamma}$ couplings at high energies. The strong correlations among the errors of f_{BW}, f_{WW}, and f_{BB} remain unchanged, suggesting the persistent importance of the $H\gamma\gamma$ measurement via no-tag $(ee)H$ events. The error of the combination $3f_{\phi 2} - 2f_{\phi 4}$ does not change, because it is dominated by the luminosity uncertainty. If we set $\Delta f = 0$, it reduces to ± 0.070.

As in the ILC-I only case, we obtain the eigenvectors and their errors after integrating out the uncertainty in $3f_{\phi 2} - 2f_{\phi 4}$, and hence also over the luminosity error. We find,

$$-.24f_{\phi 1} + .001f_{BW} + .95f_W - .29f_B - .005f_{WW} - .028f_{BB} = \pm.012, \tag{185a}$$

$$-.085f_{\phi 1} - .48f_{BW} + .057f_W + .16f_B + .66f_{WW} + .54f_{BB} = \pm.015, \tag{185b}$$

$$-.27f_{\phi 1} + .36f_{BW} + .21f_W + .84f_B + .15f_{WW} - .17f_{BB} = \pm.021, \tag{185c}$$

$$.70f_{\phi 1} - .35f_{BW} + .22f_W + .42f_B - .39f_{WW} + .13f_{BB} = \pm.038, \tag{185d}$$

$$.64f_{\phi 1} + .53f_{BW} + .043f_W - .14f_B + .54f_{WW} - .068f_{BB} = \pm.062, \tag{185e}$$

$$-.066f_{\phi 1} + .50f_{BW} + .008f_W - .016f_B - .31f_{WW} + .81f_{BB} = \pm.43. \tag{185f}$$

We now find that 5 combinations out of 6 coefficients are constrained better than 5% for $\Lambda = 1$ TeV. We noticed that the most accurately measured combination in Eq. (185a) is now dominated by f_W, reflecting the strong $\sqrt{s}$ dependence of the c_{3WW}, c_{3ZZ} and $c_{3Z\gamma}$ couplings; see Eq. (12g) to Eq. (12i). The reduction of the error from that of the corresponding combination in Eq. (181b) is 60%. The second best constrained combination, Eq. (185b), can be identified as the $c_{2\gamma\gamma}$ combination, whose error is reduced by 40% from the ILC-I result of Eq. (181a). The coefficient of f_B dominates the third accurately measured combination, Eq. (185c). The worst measured combination in Eq. (185f) is exactly the same as that of ILC-I only result in Eq. (181f), while its error is reduced to about 2/3, reflecting a factor of 3 larger cross sections of the dominant WW- and ZZ-fusion processes at $\sqrt{s} = 1$ TeV as compared with those at $\sqrt{s} = 500$ GeV; see Fig. 3.

D. Comparison with the precision electroweak measurements

A clear advantage of using the higher-dimensional operators to parametrize possible new physics contribution is that we can compare the sensitivity and complementarity

of any experiments, whether at high energies or low energies, in a model-independent manner.

Although the HVV couplings can also be measured at the LHC in the Higgs-strahlung processes (WH and ZH production) and in the weak-boson fusion processes, the expected sensitivity to the higher-dimensional operators [31,32] is not competitive with that expected at the ILC. On the other hand, the sensitivity of the precision measurements of the Z-boson and the W-boson properties on the higher-dimensional operators will remain competitive even in the ILC era. In this last subsection, we therefore compare our results with those of the present and future precision electroweak measurements. Although the results from LEP and SLC experiments have been finalized [33], both the mean values and the errors of the coefficients of the two operators, $\mathcal{O}_{\phi 1}$ and $\mathcal{O}_{BW}$ in Eq. (2), will depend not only on m_H but also strongly on the continuously improving measurements of m_t and m_W, and to a lesser extent on $\alpha_s(m_Z)_{\overline{\rm MS}}$ and $\alpha(m_Z^2)$. We therefore present details of the dependences of the precision observables on these parameters.

It is well known that the two operators $\mathcal{O}_{\phi 1}$ and $\mathcal{O}_{BW}$ in Eq. (2) contribute to the Z- and W-boson properties [10,34] via the oblique parameters S and T [21,35,36]

$$(\Delta S)_{\rm NP} = -4\pi \frac{v^2}{\Lambda^2} f_{BW}, \tag{186a}$$

$$(\Delta T)_{\rm NP} = -\frac{1}{2\alpha}\frac{v^2}{\Lambda^2} f_{\phi 1}. \tag{186b}$$

Here, $(\Delta S)_{\rm NP}$ and $(\Delta T)_{\rm NP}$ are the new physics contributions to the S and T parameters, respectively. All the Z-boson parameters are parametrized in terms of the two parameters ΔS_Z and ΔT_Z [37], which are related to the S and T parameters as

$$\Delta S_Z = \Delta S + \Delta R_Z, \tag{187a}$$

$$\Delta T_Z = \Delta T + 1.49\Delta R_Z, \tag{187b}$$

where ΔR_Z denotes the difference in the effective Z-boson coupling, $\bar{g}_Z^2(q^2)$ [23], between $q^2 = 0$ (where S and T parameters are defined) and $q^2 = m_Z^2$ (where the coupling is measured precisely at LEP and SLC). By using the 13 data set of Z-pole parameters [33], we obtain the following fit in terms of 4 parameters ΔS_Z, ΔT_Z, m_t, and $\alpha_s(m_Z)_{\overline{\rm MS}}$;

$$\begin{aligned} \Delta S_Z &= 0.037 + 0.0045x_t - 0.037x_s \pm 0.105 \quad \begin{pmatrix} 1. & \\ 0.90 & 1. \end{pmatrix}, \\ \Delta T_Z &= 0.043 + 0.0084x_t - 0.065x_s \pm 0.136 \end{aligned} \tag{188a}$$

$$\chi^2_{\rm min} = 15.5 + \left(\frac{x_t + x_s + 2.8}{4.3}\right)^2 + \left(\frac{x_s + 0.17}{0.79}\right)^2. \tag{188b}$$

Here, $x_t = (m_t - 172\ {\rm GeV})/3\ {\rm GeV}$ and $x_s = (\alpha_s - 0.118)/0.003$. The direct m_t dependence of the fit comes from the $Zb\bar{b}$ vertex correction, and the α_s dependence comes from $\Gamma(Z \to {\rm hadrons})$.

In the above fit, ΔS, ΔT, and ΔR_Z are measured from their reference values in the SM at $m_H = 100$ GeV, $m_t = 172$ GeV, $\alpha_s(m_Z)_{\overline{\rm MS}} = 0.118$, and $\Delta\alpha^5_{\rm had} = 0.0277$. Because the values of m_H, m_t, α_s, and $\Delta\alpha^5_{\rm had}$ will be measured precisely in the future, we parametrized their dependence as [37,38]

$$(\Delta S)_{\rm SM} = 0.0963x_h - 0.0224x_h^2 + 0.0026x_h^3 - 0.0014x_t - 0.033x_a, \tag{189a}$$

$$(\Delta T)_{\rm SM} = -0.0432x_h - 0.0539x_h^2 + 0.0096x_h^3 + 0.0367x_t - 0.0007x_h x_t - 0.0033x_s \tag{189b}$$

$$(\Delta R_Z)_{\rm SM} = 0.00\,838(1 - e^{-2x_h}), \tag{189c}$$

where $x_h = \ln(m_H/100\ {\rm GeV})$ and $x_a = (\Delta\alpha^5_{\rm had} - 0.0277)/0.0003$.

In addition to the Z-boson parameters, the W-boson mass is also sensitive to the operators $f_{\phi 1}$ and f_{BW}. Their dependences can be parametrized as

$$m_W[{\rm GeV}] = 80.318 - 0.288(\Delta S) + 0.418(\Delta T) + 0.337(\Delta U) - 0.0055x_a, \tag{190}$$

where the SM contribution to the U parameter is

$$(\Delta U)_{\rm SM} = -0.2974x_h - 0.0260x_h^2 + 0.0772x_t + 0.0004x_t^2, \tag{191}$$

We note that none of the dimension-six operators in Eq. (2) contribute to ΔU and ΔR_Z;

$$(\Delta U)_{\rm NP} = (\Delta R_Z)_{\rm NP} = 0. \tag{192}$$

By using the fit Eq. (188) of the LEP and SLC results [33] on the Z parameters, and the latest estimates of m_W, m_t, α_s [2] and $\Delta\alpha^5_{\rm had}$ [39]

$$m_W[{\rm GeV}] = 80.403 \pm 0.029, \tag{193a}$$

$$m_t[{\rm GeV}] = 172.5 \pm 2.3, \tag{193b}$$

$$\alpha_s(m_Z)_{\overline{\rm MS}} = 0.118 \pm 0.002, \tag{193c}$$

$$\Delta\alpha^5_{\rm had} = 0.02\,768 \pm 0.00\,022, \tag{193d}$$

we find the constraints

$$\begin{matrix}(\frac{1\ \mathrm{TeV}}{\Lambda})^2 f_{\phi 1} = -0.048 \pm 0.028 \\ (\frac{1\ \mathrm{TeV}}{\Lambda})^2 f_{BW} = -0.093 \pm 0.14 \end{matrix} \quad \begin{pmatrix} 1. & \\ 0.83 & 1. \end{pmatrix}, \tag{194}$$

with $\chi^2_{\mathrm{min}}/\mathrm{d.o.f.} = 20.5/12$, for $m_H = 120$ GeV ($x_h = 0.1823$). By comparing Eq. (194) with Eq. (180) for ILC-I and Eq. (184) for the combined ILC-I and ILC-II analysis, we find that the low-energy data constrain $f_{\phi 1}$ and f_{BW} better than the ILC. On the other hand, the two combination of the operators that are constrained by the low-energy data

$$.987 f_{\phi 1} - .16 f_{BW} = -0.032 \pm 0.015, \tag{195a}$$

$$.16 f_{\phi 1} + .987 f_{BW} = -0.10 \pm 0.14 \tag{195b}$$

are quite orthogonal to the most precisely measured combinations at ILC-I, Eq. (180), and those in the combined ILC-I and ILC-II analysis, Eq. (184). For instance, if we combine Eqs. (184) and (194), we find

$$\begin{matrix}(\frac{1\ \mathrm{TeV}}{\Lambda})^2 f_{\phi 1} = -0.048 \pm .020 \\ (\frac{1\ \mathrm{TeV}}{\Lambda})^2 f_{BW} = -0.093 \pm .10 \\ (\frac{1\ \mathrm{TeV}}{\Lambda})^2 f_{W} = \pm .015 \\ (\frac{1\ \mathrm{TeV}}{\Lambda})^2 f_{B} = \pm .025 \\ (\frac{1\ \mathrm{TeV}}{\Lambda})^2 f_{WW} = \pm .065 \\ (\frac{1\ \mathrm{TeV}}{\Lambda})^2 f_{BB} = \pm .15 \end{matrix} \quad \begin{pmatrix} 1 & & & & & \\ .68 & 1 & & & & \\ .27 & .28 & 1 & & & \\ -.12 & -.17 & .38 & 1 & & \\ -.34 & -.65 & -.40 & -.25 & 1 & \\ .59 & .93 & .36 & -.009 & -.86 & 1 \end{pmatrix}, \tag{196}$$

and now all the 6 operator coefficients are constrained rather independently, except for f_{BB}, which is still correlated with f_{BW} and f_{WW}. It is remarkable that even the errors of $f_{\phi 1}$ and f_{BW} are reduced significantly ($\sim 30\%$) by the ILC data. Because of the strong correlation among the errors of f_{BW}, f_{WW} and f_{BB} in Eq. (184), the addition of the low-energy data (194) leads to reduction of f_{WW} and f_{BB} errors.

We note here that the result given in Eq. (196) does not take into account improvements in the measurements of m_W and m_t, which should certainly take place at the ILC-I, and also possible improvements in the measurements of $\alpha_s(m_Z)_{\overline{\mathrm{MS}}}$ and $\Delta\alpha^5_{\mathrm{had}}$ are expected. If we replace the present constraints of Eq. (193) by

$$m_W[\mathrm{GeV}] = 80.403 \pm 0.010, \tag{197a}$$

$$m_t[\mathrm{GeV}] = 172.50 \pm 0.10, \tag{197b}$$

$$\alpha_s(m_Z)_{\overline{\mathrm{MS}}} = 0.1180 \pm 0.0010, \tag{197c}$$

$$\Delta\alpha^5_{\mathrm{had}} = 0.02768 \pm 0.00\,010, \tag{197d}$$

without changing their mean values, the low-energy constraints will become

$$\begin{matrix}(\frac{1\ \mathrm{TeV}}{\Lambda})^2 \Delta f_{\phi 1} = -0.082 \pm 0.018 \\ (\frac{1\ \mathrm{TeV}}{\Lambda})^2 \Delta f_{BW} = -0.21 \pm 0.12 \end{matrix} \quad \begin{pmatrix} 1. & \\ 0.95 & 1. \end{pmatrix}. \tag{198}$$

Most importantly, the error of $f_{\phi 1}$ is reduced to about a half, because $f_{\phi 1}$ has rather strong dependence on m_t.

In addition, if there are new measurements at GigaZ, we can measure the effective weak-mixing angle much more accurately. For instance, an estimate in Ref. [40] gives

$$\sin^2\theta^{\mathrm{eff}}_W = 0.23153 \pm 0.000\,013. \tag{199}$$

The effective mixing angle can also be parametrized as [37,38]

$$\sin^2\theta^{\mathrm{eff}}_W = 0.23\,148 + 0.00\,359(\Delta S_Z) - 0.00\,241(\Delta T_Z) + 0.00\,011 x_\alpha, \tag{200}$$

and the constraints on $f_{\phi 1}$ and f_{BW} will become

$$\begin{matrix}(\frac{1\ \mathrm{TeV}}{\Lambda})^2 \Delta f_{\phi 1} = -0.097 \pm 0.011 \\ (\frac{1\ \mathrm{TeV}}{\Lambda})^2 \Delta f_{BW} = -0.32 \pm 0.062 \end{matrix} \quad \begin{pmatrix} 1. & \\ 0.95 & 1. \end{pmatrix}, \tag{201}$$

with $\chi^2/\mathrm{d.o.f} = 30.9/13$.[6] Both errors of $f_{\phi 1}$ and f_{BW} are reduce by a factor 2.5 and 2.3, respectively, from Eq. (194). The eigenvectors and its errors are

$$.98 f_{\phi 1} - .17 f_{BW} = -0.041 \pm 0.0034, \tag{202a}$$

$$.17 f_{\phi 1} + .98 f_{BW} = -0.33 \pm 0.062. \tag{202b}$$

Although the most accurately measured combination of the dimension-six operator does not change from Eq. (195), the error is reduced by a factor of 4.4. We note, however, that the reduction of the errors are limited by the error of $\Delta\alpha^5_{\mathrm{had}}$ assumed in Eq. (197d), whose contribution to the uncertainty of the x_α term in Eq. (200) is 3 times larger than the error in Eq. (199).

If we combine Eq. (201) with ILC-I + ILC-II result of Eq. (196), we find

[6]Neither the low probability of the fit nor the 13σ evidence for $(\Delta f_{\phi 1}, \Delta f_{BW})$ in Eq. (201) is our concern, since they are artifacts of our keeping the present mean values Eq. (197) and (199) when reducing their errors.

$$\begin{array}{l}(\frac{1\ \mathrm{TeV}}{\Lambda})^2 f_{\phi 1} = -0.097 \pm 0.010 \\ (\frac{1\ \mathrm{TeV}}{\Lambda})^2 f_{BW} = -0.32 \pm 0.056 \\ (\frac{1\ \mathrm{TeV}}{\Lambda})^2 f_{W} = \pm 0.014 \\ (\frac{1\ \mathrm{TeV}}{\Lambda})^2 f_{B} = \pm 0.025 \\ (\frac{1\ \mathrm{TeV}}{\Lambda})^2 f_{WW} = \pm 0.053 \\ (\frac{1\ \mathrm{TeV}}{\Lambda})^2 f_{BB} = \pm 0.096 \end{array} \quad \begin{pmatrix} 1 & & & & & \\ .94 & 1 & & & & \\ .17 & .18 & 1 & & & \\ -.088 & -.093 & .43 & 1 & & \\ -.38 & -.42 & -.36 & -.40 & 1 & \\ .75 & .80 & .31 & .16 & -.81 & 1 \end{pmatrix}. \tag{203}$$

Thanks to the precise measurements of $f_{\phi 1}$ and f_{BW}, the errors of f_{BB} and f_{WW} are reduced. The error of f_W and f_B are not affected much by the improved measurements of the weak-boson parameters, and the constraints of the type (185a) ~ (185c) will still give additional information on new physics from the HVV coupling measurements.

We hope that our report will be useful in studying the physics potential of the ILC project.

ACKNOWLEDGMENTS

We thank S. Ishihara, J. Kamoshita, and Y. Uehara for participating in stimulating discussions in the early stage of this study. This work is supported in part by the JSPS Core University Program, and the Grant-in-Aid for Scientific Research (#17540281 and #18340060) from MEXT, Japan. S. D. would like to thank the Science and Engineering Research Council, Department of Science and Technology, the Government of India for partial financial support (SR/S2/HEP-12/2006).

APPENDIX A: THE 3-BODY PHASE SPACE

We parametrize the four momentum of the $e^+e^- \to f\bar{f}H$ process; see Eq. (18), in the laboratory frame as follows:

$$k_1^\mu = \frac{\sqrt{s}}{2}(1, 0, 0, 1), \tag{A1a}$$

$$k_2^\mu = \frac{\sqrt{s}}{2}(1, 0, 0, -1), \tag{A1b}$$

$$p_1^\mu = \frac{\sqrt{s}}{2}x_1(1, \sin\theta_1\cos\phi_1, \sin\theta_1\sin\phi_1, \cos\theta_1), \tag{A1c}$$

$$p_2^\mu = \frac{\sqrt{s}}{2}x_2(1, \sin\theta_2\cos\phi_2, \sin\theta_2\sin\phi_2, \cos\theta_2), \tag{A1d}$$

$$p_{\mathrm{H}}^\mu = k_1^\mu + k_2^\mu - p_1^\mu - p_2^\mu, \tag{A1e}$$

$$= x_H\frac{\sqrt{s}}{2}(1, \beta_H\sin\theta_H, 0, \beta_H\cos\theta_H), \tag{A1f}$$

where we ignore the masses of $e^\pm$, f, and $\bar{f}$, and the Higgs boson is produced in the xz-plane

$$x_1\sin\theta_1\sin\phi_1 + x_2\cos\theta_2\cos\phi_2 = 0. \tag{A2}$$

The Higgs-boson energy fraction and its velocity are

$$x_H = \frac{2E_H}{\sqrt{s}} = 2 - x_1 - x_2, \qquad \beta_H = \sqrt{1 - 4m_H^2/sx_H^2}. \tag{A3}$$

We parametrize the f and $\bar{f}$ four momenta also in the rest frame of the $f\bar{f}$ system,

$$p_1^{*\mu} = \frac{m_{f\bar{f}}}{2}(1, \sin\theta^*\cos\phi^*, \sin\theta^*\sin\phi^*, \cos\theta^*),$$
$$p_2^{*\mu} = \frac{m_{f\bar{f}}}{2}(1, -\sin\theta^*\cos\phi^*, -\sin\theta^*\sin\phi^*, -\cos\theta^*), \tag{A4}$$

where $m_{f\bar{f}}^2 = (p_1 + p_2)^2$, θ^* and ϕ^* are the polar and azimuthal angle, respectively, with respect to the momentum direction of the $f\bar{f}$ system in the laboratory frame. After making an appropriate boost to the laboratory frame with

$$\beta = \frac{x_H\beta_H}{2 - x_H}, \qquad \gamma = \frac{1}{\sqrt{1-\beta^2}}, \tag{A5}$$

and an appropriate rotation about the y-axis by θ_H, we find p_1^μ and p_2^μ in the laboratory frame

$$\begin{aligned} p_1^\mu = \frac{m_{f\bar{f}}}{2}&(\gamma(1 + \beta c_{\theta^*}), c_{\theta_H}s_{\theta^*}c_{\phi^*} \\ &+ s_{\theta_H}\gamma(\beta + c_{\theta^*}), s_{\theta^*}s_{\phi^*}, c_{\theta_H}\gamma(\beta + c_{\theta^*}) \\ &- s_{\theta_H}s_{\theta^*}c_{\phi^*}), \\ p_2^\mu = \frac{m_{f\bar{f}}}{2}&(\gamma(1 - \beta c_{\theta^*}), -c_{\theta_H}s_{\theta^*}c_{\phi^*} \\ &+ s_{\theta_H}\gamma(\beta - c_{\theta^*}), -s_{\theta^*}s_{\phi^*}, c_{\theta_H}\gamma(\beta - c_{\theta^*}) \\ &+ s_{\theta_H}s_{\theta^*}c_{\phi^*}). \end{aligned} \tag{A6}$$

Here, we introduce a shorthand $s_\theta \equiv \sin\theta$ and $c_\theta \equiv \cos\theta$. Comparing Eq. (A1) with Eq. (A6), we find

$$x_1 = \frac{m_{f\bar{f}}}{\sqrt{s}}\gamma(1 + \beta c_{\theta^\star}),$$
$$x_2 = \frac{m_{f\bar{f}}}{\sqrt{s}}\gamma(1 - \beta c_{\theta^\star}), \tag{A7a}$$

$$\cos\theta_1 = \frac{c_{\theta_H}\gamma(\beta + c_{\theta^*}) - s_{\theta_H}s_{\theta^*}c_{\phi^*}}{\gamma(1 + \beta c_{\theta^*})},$$
$$\cos\theta_2 = \frac{c_{\theta_H}\gamma(\beta - c_{\theta^*}) + s_{\theta_H}s_{\theta^*}c_{\phi^*}}{\gamma(1 - \beta c_{\theta^*})}, \tag{A7b}$$

$$\sin\theta_1\sin\phi_1 = \frac{s_{\theta^*}s_{\phi^*}}{\gamma(1 + \beta c_{\theta^*})},$$
$$\sin\theta_2\sin\phi_2 = -\frac{s_{\theta^*}s_{\phi^*}}{\gamma(1 - \beta c_{\theta^*})}, \tag{A7c}$$

which satisfy Eq. (A2). We can now parametrize the 3-body phase space as

$$d\Phi_3 \equiv (2\pi)^4\delta^4(k_1+k_2-p_1-p_2-p_H) \times\left[\prod_{i=1}^{2}\frac{d^3p_i}{(2\pi)^3 2E_i}\right]\frac{d^3p_H}{(2\pi)^3 2E_H}, \tag{A8a}$$

$$= \frac{1}{(8\pi)^2}\bar{\beta}\left(\frac{m_{f\bar{f}}^2}{s},\frac{m_H^2}{s}\right)\frac{d\cos\theta_H}{2}\frac{dm_{f\bar{f}}^2}{2\pi}\frac{d\cos\theta^* d\phi^*}{4\pi}, \tag{A8b}$$

$$= \frac{\sqrt{s}}{128\pi^3}\bar{\beta}\left(\frac{m_{f\bar{f}}^2}{s},\frac{m_H^2}{s}\right)dE_H d\cos\theta_H\frac{d\cos\theta^* d\phi^*}{4\pi}, \tag{A8c}$$

$$= \frac{\sqrt{s}}{128\pi^3}\bar{\beta}\left(\frac{m_{f\bar{f}}^2}{s},\frac{m_H^2}{s}\right)dp_{TH}dy_H\frac{d\cos\theta^* d\phi^*}{4\pi}, \tag{A8d}$$

$$= \frac{s}{128\pi^3}\frac{x_1(1-x_1-m_H^2/s)}{[1-x_1(1-\cos\theta_{12})/2]^2}dx_1 \times\frac{d\cos\theta_1 d\phi_1}{4\pi}\frac{d\cos\theta_2 d\phi_2}{4\pi}, \tag{A8e}$$

where

$$\bar{\beta}(a,b) = \sqrt{1-2(a+b)+(a-b)^2}, \tag{A9a}$$

$$\cos\theta_{12} = \cos\theta_1\cos\theta_2+\sin\theta_1\sin\theta_2\cos(\phi_2-\phi_1). \tag{A9b}$$

We use the phase-space parametrization (A8b) in the analysis of the ZH production process, (A8c) or (A8d) in the analysis of the $\nu_e\bar{\nu}_e H$ process where the undetectable ν_e and $\bar{\nu}_e$ angles ($\cos\theta^*$,ϕ^*) are integrated out, and (A8e) in the analysis of the double-tag (eeH) events, following the prescription given in the Appendix A of Ref. [26]. In the analysis of single-tag (e)eH events and no-tag (ee)H events, the electron mass should be kept in the integration of the forward scattering angles [26].

APPENDIX B: MASSLESS FERMION CURRENTS

In this appendix, we show the explicit form of the massless fermion currents, which appear in the t-channel and s-channel gauge-boson exchange processes. The t-channel currents of Eqs. (47) and (113) for $\sigma_1=\lambda_1=\sigma$ and $\sigma_2=\lambda_2=\bar{\sigma}$ are

$$j^\mu_{e^-(\sigma,\sigma)} = \sqrt{sx_1}\left(\cos\frac{\theta_1}{2},\sin\frac{\theta_1}{2}e^{i\sigma\phi_1},-i\sigma\sin\frac{\theta_1}{2}e^{i\sigma\phi_1},\cos\frac{\theta_1}{2}\right), \tag{B1a}$$

$$j^\mu_{e^+(\bar{\sigma},\bar{\sigma})} = \sqrt{sx_2}\left(\sin\frac{\theta_2}{2},\cos\frac{\theta_2}{2}e^{-i\bar{\sigma}\phi_2},i\bar{\sigma}\cos\frac{\theta_2}{2}e^{-i\bar{\sigma}\phi_2},-\sin\frac{\theta_2}{2}\right), \tag{B1b}$$

where $\sigma/2$ denotes the e^- helicities in Eq. (B1a), and $\bar{\sigma}/2$ denotes the e^+ helicities in Eq. (B1b). In the t-channel W-exchange process, $e^+e^-\to\nu_e\bar{\nu}_e H$, only the $\sigma=-\bar{\sigma}=-$combination contributes, while in $e^+e^-\to e^+e^-H$ via t-channel Z and γ exchange processes, both helicities contribute. The following 8 combinations of the contractions appear in the cross section with higherdimensional operators:

$$j^\mu_{e^-(-,-)}g_{\mu\nu}j^\nu_{e^+(+,+)} = [j^\mu_{e^-(+,+)}g_{\mu\nu}j^\nu_{e^+(-,-)}]^* \equiv \mathcal{F}(\theta_1,\theta_2), \tag{B2a}$$

$$j^\mu_{e^-(-,-)}g_{\mu\nu}j^\nu_{e^+(-,-)} = [j^\mu_{e^-(+,+)}g_{\mu\nu}j^\nu_{e^+(+,+)}]^* \equiv \mathcal{F}(\theta_1,\theta_2)\mathcal{H}(\theta_1,\theta_2,\phi), \tag{B2b}$$

$$j^\mu_{e^-(-,-)}q_{1\nu}q_{2\mu}j^\nu_{e^+(+,+)} = [j^\mu_{e^-(+,+)}q_{1\nu}q_{2\mu}j^\nu_{e^+(-,-)}]^* \equiv \frac{s}{8}\mathcal{F}(\theta_1,\theta_2)\mathcal{G}(\theta_1,\theta_2,\phi), \tag{B2c}$$

$$j^\mu_{e^-(-,-)}q_{1\nu}q_{2\mu}j^\nu_{e^+(-,-)} = [j^\mu_{e^-(+,+)}q_{1\nu}q_{2\mu}j^\nu_{e^+(+,+)}]^* \equiv \frac{s}{8}\mathcal{F}(\theta_1,\theta_2)\mathcal{G}'(\theta_1,\theta_2,\phi). \tag{B2d}$$

Here, $q_1=k_1-p_1$ and $q_2=k_2-p_2$ are the transfer momenta in the t channel, and $\phi=\phi_1-\phi_2$. The functions $\mathcal{F}(\theta_1,\theta_2)$, $\mathcal{H}(\theta_1,\theta_2,\phi)$, $\mathcal{G}(\theta_1,\theta_2,\phi)$, and $\mathcal{G}'(\theta_1,\theta_2,\phi)$ are

$$\mathcal{F}(\theta_1,\theta_2) = 2s\sqrt{x_1x_2}\cos\frac{\theta_1}{2}\sin\frac{\theta_2}{2}, \tag{B3a}$$

$$\mathcal{H}(\theta_1,\theta_2,\phi) = 1-\tan\frac{\theta_1}{2}\cot\frac{\theta_2}{2}e^{i\phi}, \tag{B3b}$$

$$\mathcal{G}(\theta_1,\theta_2,\phi) = \left[2-x_1(1+\cos\theta_1)+x_1\sin\theta_1\cot\frac{\theta_2}{2}e^{-i\phi}\right]\left[2-x_2(1-\cos\theta_2)+x_2\sin\theta_2\tan\frac{\theta_1}{2}e^{i\phi}\right], \tag{B3c}$$

$$\mathcal{G}'(\theta_1,\theta_2,\phi) = \left[2-x_1(1+\cos\theta_1)+x_1\sin\theta_1\cot\frac{\theta_2}{2}e^{i\phi}\right]\left[2-x_2(1-\cos\theta_2)+x_2\sin\theta_2\tan\frac{\theta_1}{2}e^{i\phi}\right]. \tag{B3d}$$

The currents that appear in the s-channel ZH production process are rather simple. The initial e^+e^- annihilate currents are

$$j^{\mu}_{1\sigma} = \bar{v}\left(k_2, -\frac{\sigma}{2}\right)\gamma^{\mu}P_{\sigma}u\left(k_1, \frac{\sigma}{2}\right) = \sqrt{s}(0, -\sigma, -i, 0), \tag{B4}$$

where the e^- helicity is $\sigma/2$. The final $Z \to f\bar{f}$ decay currents are

$$\begin{aligned} j^{\mu}_{2\sigma'} &= \bar{u}\left(p_1, \frac{\sigma'}{2}\right)\gamma^{\mu}P_{\sigma'}v\left(p_2, -\frac{\sigma'}{2}\right) \\ &= \sqrt{s}(0, -\sigma'\cos\theta^*\cos\phi^* \\ &\quad - i\sin\phi^*, -\sigma'\cos\theta^*\sin\phi^* + i\cos\phi^*, \sigma'\sin\theta^*) \end{aligned} \tag{B5a}$$

in the $f\bar{f}$ rest frame of Eq. (A6), where the f helicity is $\sigma'/2$. When contracted with the decaying Z-boson polarization vector

$$\epsilon^{\mu}(\lambda = \pm) = \frac{1}{\sqrt{2}}(0, \mp 1, -i, 0), \tag{B6a}$$

$$\epsilon^{\mu}(\lambda = 0) = (0, 0, 0, 1), \tag{B6b}$$

we find

$$\epsilon(\pm)\cdot j_{2\sigma'} = -\sqrt{\frac{s}{2}}(1 \pm \sigma' c_{\theta^*})e^{\pm i\phi^*}, \tag{B7a}$$

$$\epsilon(0)\cdot j_{2\sigma'} = -\sqrt{s}\sigma' s_{\theta^*}. \tag{B7b}$$

The decay density matrix elements of Eq. (90) are obtained from these equations.

[1] P. Teixeira-Dias, J. Phys. Conf. Ser. **110**, 042030 (2008), and references therein.
[2] W. M. Yao *et al.* (Particle Data Group), J. Phys. G**33**, 1 (2006) and 2007 partial update for 2008 edition. http://pdglive.lbl.gov/listings.
[3] A. Duperrin, arXiv:0805.3624; U. Aglietti *et al.*, arXiv:hep-ph/0612172.
[4] D. Zeppenfeld, R. Kinnunen, A. Nikitenko, and E. Richter-Was, Phys. Rev. D **62**, 013009 (2000).
[5] D. Atwood and A. Soni, Phys. Rev. D **45**, 2405 (1992).
[6] M. Davier, L. Duflot, F. Le Diberder, and A. Rougé, Phys. Lett. B **306**, 411 (1993).
[7] M. Diehl and O. Nachtmann, Z. Phys. C **62**, 397 (1994).
[8] J. F. Gunion, B. Grzadkowski, and X. G. He, Phys. Rev. Lett. **77**, 5172 (1996).
[9] C. J. C. Burges and H. J. Schnitzer, Nucl. Phys. **B228**, 464 (1983); W. Buchmüller and D. Wyler, Nucl. Phys. **B268**, 621 (1986); C. N. Leung, S. T. Love, and S. Rao, Z. Phys. **C31**, 433 (1986); A. De Rújula, M. B. Gavela, P. Hernández, and E. Massó, Nucl. Phys. **B384**, 3 (1992).
[10] B. Grinstein and M. B. Wise, Phys. Lett. B **265**, 326 (1991).
[11] K. Hagiwara, T. Hatsukano, S. Ishihara, and R. Szalapski, Nucl. Phys. **B496**, 66 (1997).
[12] J. P. Ma and B. H. McKellar, Phys. Rev. D **52**, 22 (1995).
[13] K. Hagiwara, S. Ishihara, J. Kamoshita, and B. A. Kniehl, Eur. Phys. J. C **14**, 457 (2000).
[14] M. L. Stong and K. Hagiwara, Waikoloa Linear Collid. 0631 (1993).
[15] S. S. Biswal, D. Choudhury, R. M. Godbole, and R. K. Singh, Phys. Rev. D **73**, 035001 (2006); **74**, 039904(E) (2006).
[16] D. Choudhury and Mamta, Phys. Rev. D**74**, 115019 (2006); I. Sahin, Phys. Rev. D **77**, 115010 (2008).
[17] V. Barger, T. Han, P. Langacker, B. McElrath, and P. Zerwas, Phys. Rev. D **67**, 115001 (2003).
[18] F. de Campos, M. C. Gonzalez-Garcia, and S. F. Novaes, Phys. Rev. Lett. **79**, 5210 (1997).
[19] M. C. Gonzalez-Garcia, S. M. Lietti, and S. F. Novaes, Phys. Rev. D **57**, 7045 (1998).
[20] K. Hagiwara, S. Ishihara, R. Szalapski, and D. Zeppenfeld, Phys. Rev. D **48**, 2182 (1993).
[21] M. E. Peskin and T. Takeuchi, Phys. Rev. D **46**, 381 (1992); Phys. Rev. Lett. **65**, 964 (1990).
[22] M. B. Einhorn, D. R. T. Jones, and M. J. G. Veltman, Nucl. Phys. **B191**, 146 (1981).
[23] K. Hagiwara, Annu. Rev. Nucl. Part. Sci.**48**, 463 (1998); K. Hagiwara, S. Matsumoto, D. Haidt, and C. S. Kim, Z. Phys. C **64**, 559 (1994); **68**, 352(E) (1995).
[24] Yu Matsumoto, Ph.D. thesis (unpublished) Graduate University for Advanced Studies (Soken-dai).
[25] V. M. Budnev, I. F. Ginzburg, G. V. Meledin, and V. G. Serbo, Phys. Rep. **15**, 181 (1975).
[26] K. Hagiwara, H. Iwasaki, A. Miyamoto, H. Murayama, and D. Zeppenfeld, Nucl. Phys. **B365**, 544 (1991).
[27] J. F. Gunion, H. E. Haber, G. Kane, and S. Dawson, *Higgs Hunter's Guide* (Addison-Wesley, Redwood City, California, 2000).
[28] B. Badelek *et al.* (ECFA/DESY Photon Collider Working Group), Int. J. Mod. Phys. A **19**, 5097 (2004).
[29] T. Han, Yu-Ping Kuang, and Bin Zhang, Phys. Rev. D **73**, 055010 (2006).
[30] A. T. Banin, I. F. Ginzburg, and I. P. Ivanov, Phys. Rev. D **59**, 115001 (1999).
[31] Oscar J. P. Eboli, M. C. Gonzalez-Garcia, S. M. Lietti, and S. F. Novae, Phys. Lett. B **478**, 199 (2000).
[32] B. Zhang, Yu-Ping Kuang, Hong-Jian He, and C. P. Yuan, Phys. Rev. D **67**, 114024 (2003).
[33] ALEPH Collaboration, DELPHI Collaboration, L3 Collaboration, OPAL Collaboration, SLD Collaboration, LEP Electroweak Working Group, SLD Electroweak Group, and SLD Heavy Flavour Group, Phys. Rep. **427**, 257 (2006).
[34] B. Holdom and J. Terning, Phys. Lett. B **247**, 88 (1990).
[35] D. C. Kennedy and P. Langacker, Phys. Rev. Lett. **65**, 2967 (1990); **66**, 395(E) (1991).

[36] G. Altarelli, R. Barbieri, and S. Jadach, Nucl. Phys. **B369**, 3 (1992); **B376**, 444(E) (1992); G. Altarelli, R. Barbieri, and F. Caravaglios, Nucl. Phys. **B405** 3 (1993).
[37] G. C. Cho and K. Hagiwara, Nucl. Phys. **B574**, 623 (2000).
[38] G. C. Cho, K. Hagiwara, D. Nomura, and Y. Matsumoto (unpublished).
[39] K. Hagiwara, A. D. Martin, D. Nomura, and T. Teubner, Phys. Lett. B **649**, 173 (2007).
[40] S. Heinemeyer, W. Hollik, A. M. Weber, and G. Weiglein, Report No. IPPP-07-78, Report No. DCPT-07-156, Report No. LCWS-2007-TEV03, 2007.